Hidden-driver inference reveals synergistic brain-penetrant therapies for medulloblastoma

Running Title: Target cancer hidden drivers to accelerate drug combination discovery

Authors: Jingjing Liu[1,10], Xu Yang[1,10], Mingrui Zhu[1,10], Xinran Dong[2], Honglei Zhou[1], Brandon Bianski[3], Barbara M. Jonchere[4], Wenwei Lin[5], Xiang Fu[6], Lei Yang[6], Burgess B. Freeman III[7], Abigail S. Wang[1], Ruilin Jiang[1], Taosheng Chen[5], Giles W. Robinson[8], Martine F. Roussel[4], Thomas E. Merchant[3], Amar Gajjar[8,9], Jiyang Yu[1,*]

[1]Department of Computational Biology, St. Jude Children's Research Hospital, Memphis, TN 38105, USA

[2]Center for Molecular Medicine, Children's Hospital of Fudan University, Shanghai 201102, P.R. China

[3]Department of Radiation Oncology, St Jude Children's Research Hospital, Memphis, TN 38105, USA

[4]Department of Tumor Cell Biology, St Jude Children's Research Hospital, Memphis, TN 38105, USA

[5]Department of Chemical Biology and Therapeutics, St Jude Children's Research Hospital, Memphis, TN 38105, USA

[6]Analytical Technologies Center, Department of Chemical Biology and Therapeutics, St Jude Children's Research Hospital, Memphis, TN 38105, USA

[7]Preclinical Pharmacokinetics Shared Resource, St Jude Children's Research Hospital, Memphis, TN 38105, USA

[8]Department of Oncology, St. Jude Children's Research Hospital, Memphis, TN, 38105, USA

[9]Department of Pediatric Medicine, Department of Oncology, St Jude Children's Research Hospital, Memphis, TN 38105, USA

[10]: These authors contributed equally

[*]Correspondence: jiyang.yu@stjude.org

ABSTRACT

Effective therapies for high-risk medulloblastoma (MB), particularly MYC-driven Group 3 (G3) MB, remain elusive due to limited druggable mutations, poor blood–brain barrier (BBB) penetration, and rapid resistance. We developed **SINBA (Synergy Inference by Data-driven Network-Based Bayesian Analysis)**, a systems biology framework that predicts synergistic, BBB-permeable drug combinations by identifying *hidden drivers* that sustain oncogenic programs without detectable genetic or transcriptional alterations. Integrating MB-specific gene networks, transcriptomic data, and drug–gene interactions, SINBA prioritized 32 candidate combinations, of which 19 were experimentally validated as synergistic. The **MEK inhibitor mirdametinib** and **p38 inhibitor regorafenib** emerged as the top brain-penetrant pair, suppressing G3 MB progression and extending survival in human xenograft and immunocompetent mouse models, with efficacy enhanced by low-dose radiation. Single-cell analysis revealed selective targeting of the **developmental origins of G3 MB**, accompanied by immune microenvironment reprogramming. These findings establish *hidden-driver inference* as a generalizable framework for rational drug combination discovery.

SIGNIFICANCE

The SINBA platform enables rapid identification of brain-penetrant, synergistic drug combinations by targeting hidden bottleneck drivers in high-risk tumors. SINBA-guided screening revealed that MEK inhibitors combined with regorafenib selectively eliminate the developmental cell-of-origin in G3 medulloblastoma and reprogram the tumor microenvironment, providing a clinically actionable precision oncology strategy.

53 **INTRODUCTION**

54

55 Brain tumors are the most common pediatric solid tumor, producing more deaths in children under
56 the age of 20 than any other pediatric cancer(1). Among them, the most prevalent is
57 medulloblastoma (MB), an embryonal tumor of the cerebellum that consists of four distinct
58 molecular subtypes: WNT, SHH, Group 3 (G3), and Group 4 (G4)(2,3). Despite the unique
59 molecular and clinical characteristics of these subtypes, standard treatment for medulloblastoma
60 follows a single protocol: maximal surgical resection followed by craniospinal irradiation and
61 adjuvant chemotherapy. While these interventions have improved the 5-year survival rate to over
62 80% for average-risk patients,(4,5) one in three high-risk MB patients will relapse within five years,
63 and the survival rate for relapsed patients remains dismal(6,7).

64

65 Common approaches to therapeutic discovery have yielded few clinically effective treatments for
66 high-risk MB, due to both the nature of the disease and the limitations of current methods(8). Most
67 notably, few high-risk MB cases possess well-characterized druggable alterations—in fact,
68 approximately 20% lack any identifiable genetic mutations—making the development of
69 genomics-driven targeted therapies difficult(9). High-throughput screening (HTS), though useful
70 in research contexts, produces single agent therapies that may have poor blood-brain barrier
71 (BBB) permeability, that are susceptible to rapid tumor resistance, and whose efficacy often
72 depends on the relevance of the disease model used and the extent to which it recapitulates
73 patient tumor biology.

74

75 The recent therapeutic success of combination therapies in certain cancers has generated
76 widespread interest in drug combination screening(10-18); however, standard experimental
77 methods for combination screening are costly and limited in scale. Computational approaches(19-
78 24) (such as RECODR(22) or a graph-embedding machine learning approach of single-cell

79 transcriptomics data, DrugCell(24) or the community-developed approaches generated by the
80 DREAM Consortium) have been developed to circumvent these limitations, but their utility in G3
81 MB is limited by, for example, the nature of their training datasets or their pan-cancer design.
82
83 Although few clinically actionable genes have been identified for MB(25), previous studies have
84 identified cancer driver genes that, rather than possess genetic mutations, are functionally
85 dysregulated through epigenetic modifications or post-translational alterations(26-30). Such
86 "hidden" drivers could be effective therapeutic targets; however, their lack of genetic mutation
87 makes them more challenging to identify. We therefore developed SINBA, an end-to-end workflow
88 that uses network-based Bayesian analysis to identify putative bottleneck drivers and then, based
89 on those drivers, suggests potential therapeutic drug combinations. This approach addresses two
90 of the major challenges of therapeutic discovery in MB: identifying druggable targets and reducing
91 the candidate drug pool for combination screening.
92
93 In this study, we applied SINBA to G3 medulloblastoma, leveraging the transcriptomic data of
94 three medulloblastoma patient cohorts. After validating the synergistic effects of SINBA-predicted
95 drug combinations through *in vitro* HTS, we tested the efficacy of the top-ranked combination
96 (regorafenib and a MEK inhibitor) in preclinical studies using both human xenografts and
97 immunocompetent syngeneic murine G3 MB models. Combining regorafenib-MEK inhibitor
98 treatment with low-dose irradiation improved cancer cell killing, supporting the potential benefit of
99 incorporating these agents into standard MB therapy. Single-cell RNA sequencing (scRNA-seq)
100 analysis revealed elevated driver activity and enhanced drug sensitivity scores in tumor cells that
101 transcriptomically resemble early Unipolar Brush Cell (UBC) progenitors (henceforth "early UBC
102 progenitor-like cells"), suggesting susceptibility to this combination therapy. Critically, this
103 combination profoundly remodeled the tumor microenvironment (TME) in an immunocompetent

104 syngeneic mouse model, demonstrating both direct and immunomodulatory tumor suppression
105 effects.
106
107 **RESULTS**
108
109 **Nominating synergistic brain-penetrant drug combinations for G3 MB using SINBA, a**
110 **hidden-driver-based computational framework**
111 SINBA is a network-based algorithm that unbiasedly predicts synergistic drug combinations based
112 on subtype-specific drivers. Broadly, the SINBA workflow proceeds as follows: users leverage a
113 disease-specific gene-gene interaction network to identify drivers upregulated in a selected
114 cancer subtype; these drivers are then filtered for druggability and provided as input to the SINBA
115 software. SINBA then uses the interaction network and a drug-target database to design HTS
116 experiments, the results of which are fed back into the software as additional input. Using these
117 data, SINBA matches the input drivers with other hub genes to produce gene pairs with synergistic
118 activity; these driver pairs are translated into drug pairs for subsequent combination screening.
119 Finally, the results of combination screening are analyzed for synergy using a third-party algorithm,
120 SynergyFinder(31,32); the drug pairs are then ranked according to their synergy. It should be
121 noted that driver selection and driver-drug pairing are interdependent, concurrent processes. For
122 example, the input drivers are used to select drugs for HTS, but then the results of HTS are used
123 to further refine the list of drivers.
124
125 Using the G3 subtype of MB as a proof-of-concept, we describe the SINBA workflow in greater
126 detail below (**Fig. 1A**):
127
128 ***Preparatory Steps***

129 To equip SINBA to select synergistic drug pairs with good blood-brain barrier permeability, we
130 generated a Brain Penetrant drug-target database (BPdb) consisting of 1,118 potential brain-
131 penetrant agents (targeting 2,476 genes) (**Fig. 1B**). The BPdb expands substantially on the
132 B3DB(33), a database of rigorously validated brain-penetrating compounds, by including
133 additional, potentially-penetrating agents identified in the literature and clinical trials. Agents were
134 presumed to be penetrants if they had been evaluated in neurotherapeutic trials or antibody-
135 based modalities. 41% of the drugs in the BPdb were selected in this manner; overall, 59% of the
136 drugs are FDA-approved. Five drug-gene interaction databases were used to annotate the targets
137 in the BPdb: DrugBank(34), ChEMBL(35), cMAP(36), Repurposing Hub(37), and DGIdb(38-40)
138 (**Fig. 1C; Supplementary Table S1**). Along with the BPdb, these drug-target databases were
139 integrated into SINBA, supplying it with a comprehensive set of drugs and pharmacologically
140 targetable genes to maximize generalizability outside of central nervous system tumors.
141
142 After compiling the BPdb, we pre-trained a disease-specific, gene-gene interaction network for
143 medulloblastoma by applying SJARACNe(41), a mutual-information-based algorithm, to a
144 dataset of 407 human MB patient transcriptome profiles (DKFZ_SJ)(25,42,43). The resulting
145 medulloblastoma interactome (MBi) captures the transcript-level interactions between
146 transcription factor (TF) and signaling (SIG) genes(44)—the network hubs—and their predicted
147 regulons. Altogether, the interactome comprised 1,567,381 interactions between 38,621
148 transcripts (corresponding to 15,317 genes); 12,495 of these transcripts belonged to TF and SIG
149 hub genes (7,155 total).
150 Finally, we used the pretrained MBi and our NetBID2(45) algorithm to identify G3 MB-specific
151 drivers, henceforth referred to as “seed” drivers. To do so, we superimposed the MBi onto the
152 transcriptomic profiles of patients in the pretraining cohort plus two additional validation cohorts,
153 GSE85217(46) and ICGC(9) (**Supplementary Table S2**), generating activity profiles for
154 candidate TF and SIG drivers from the gene expression data. The activity inferred for each

155 candidate driver consisted of the expression of downstream targets weighted by the interaction
156 strength. We then used NetBID2 to analyze the activity of the pretraining cohort, revealing 75
157 drivers that exhibited significantly higher activity in G3 MB compared to the other MB subgroups
158 and normal cerebellum. Drivers for which there were no targeting drugs in the BPdb were
159 discarded, leaving 45 druggable "seed drivers."
160
161 Comparison of the activity and expression profiles of these seed drivers in the two validation
162 cohorts supports SINBA's activity-based approach to driver selection. Seed drivers were found to
163 have consistent differential activity but not expression patterns across cohorts (**Supplementary**
164 **Fig. S1A**), suggesting that activity data may be a more reliable measure of gene function. Data
165 from the GSE85217 cohort, for which clinical outcomes were available, suggested that driver
166 activity may also have greater clinical relevance. Analysis of the 42 drivers with matched activity
167 and expression profiles in this cohort found patient survival to correlate significantly more with
168 driver activity than with driver gene expression. For 67% of the drivers, there was a significant
169 correlation between activity level and patient survival ($P < 0.05$); only 26% of the drivers showed
170 a similar correlation for gene expression (**Supplementary Fig. S1B**; **Supplementary Table S3**).
171 For example, the activity but not expression of BRAF and CDK7 significantly correlated with
172 overall patient survival (**Supplementary Fig. S1C**). Compared to their RNA expression levels,
173 these drivers' inferred activities had a cleaner pattern of elevation in G3 MB compared to the other
174 medulloblastoma subtypes. Likewise, in an independent proteomics cohort of MB patient
175 samples(47), there was an elevation in the phosphorylated protein activity of these genes despite
176 their total protein levels remaining unchanged (**Supplementary Fig. S1D and S1E**).
177
178 Similarly, expression of MYC—whose activation is the hallmark of G3 MB—was insufficient to
179 stratify risk groups in the GSE85217 cohort; on the other hand, there was a clear delineation in
180 MYC *activity* between high- and low-risk MB (**Supplementary Fig. S1F**). Consistent with the

181 findings for BRAF and CDK7, MYC activity—but not total protein expression—was positively
182 correlated with phospho-MYC levels in G3 MB tumors(47) (**Supplementary Fig. S1G**). These
183 results demonstrate how activity-based approaches can be used to identify clinically relevant
184 drivers that may evade discovery by conventional RNA and total protein expression analyses. To
185 explore the drug databases, gene expression and patient survival data, and driver activities
186 imputed in this study, we developed an interactive web application at https://yulab-
187 stjude.shinyapps.io/SINBA_MB.
188
189 ***Nominating Synergistic Drug Pairs with SINBA Algorithm***
190 Using the 45 seed drivers identified for G3 MB as input, SINBA predicted synergistic drug pairs
191 for G3 MB in the following steps:
192
193 First, the software selected 69 drugs from the BPdb to undergo HTS, ensuring that each of the
194 45 seed drivers was a target gene for at least one drug. SINBA then used the results of screening
195 these drugs in a G3 cell line (HDMB03) to select the top 20 most effective drugs with unique seed
196 driver targets.
197
198 To identify synergistic partner genes for the 20 seed drivers, SINBA generated a list of candidate
199 genes. It did this by filtering the hub genes from the MBi for druggability using the BPdb, yielding
200 approximately 800 candidate "partner drivers". The candidate set was further refined by
201 eliminating drivers that failed to demonstrate adequate synergy with any of the seeds. Candidate
202 drivers were considered synergistic if their combined subnetwork with a seed driver yielded higher
203 differential activity than either subnetwork alone. Driver synergy was measured using a custom
204 statistical method that assigns a quantitative “synergy score” to driver pairs (see **Methods**). To
205 select the final partners, SINBA used a greedy algorithm to determine which matrix of 20 seed
206 drivers x 16 partner drivers would generate the highest collective synergistic score (**Fig. 1C**).

207

208 Next, SINBA selected a different drug for each of the 16 partner drivers, with preference given to
209 drugs from the original library. If no suitable drug could be found in the original library, alternative
210 drugs were selected from the BPdb; these drugs (21 in total) were then screened in the G3 cell
211 line and the results used to select final partners for the remaining drivers. (For a summary of the
212 HTS results of our combined libraries (90 drugs total), see **Supplementary Fig. S2A and S2B;**
213 **Supplementary Table S4**). These 16 final partner drugs were then arranged in a matrix with the
214 20 seed drugs, producing 320 unique drug pairs for subsequent combination screening (**Fig. 1C**).
215

216 ***Drug Combination Screening and Synergy Analysis***

217 Before proceeding to comprehensive drug combination screening, we assessed the potential
218 synergy of our 320 drug pairs through a preliminary two-dose screening. Drugs were tested at
219 EC_{20} (low dose) and EC_{50} (high dose) concentrations; drugs lacking EC_{20} or EC_{50} values were
220 assigned the default values of 1 μM and 6 μM, respectively. This dual-dose strategy produced
221 1,280 unique drug-dose combinations for testing in the HDMB03 model. The efficacy of each
222 drug-dose combination was quantified using a $\Delta inhibition_{mean}$ metric: the cell growth inhibition of
223 a two-agent combination minus the mean of the inhibitions produced by using each agent alone
224 at the same dose. Remarkably, 95% of the combinations tested produced efficacies greater than
225 the mean of their parts (**Supplementary Fig. S2C**; **Supplementary Table S5**; see **Methods**).
226

227 For each drug-dose combination, we also calculated the $\Delta inhibition_{max}$, the difference in inhibition
228 between the combination and whichever of its constituents produced greater inhibition alone. We
229 then used this metric to select 32 candidate pairs that met one of the following four conditions: At
230 the low-low dose, (1) combined inhibition >90% and $\Delta inhibition_{max}$ >10%, (2) combined
231 inhibition >50% and $\Delta inhibition_{max}$ >15%, or (3) combined inhibition >80% and each single agent's

232 inhibition >70%; or, at any other dose-combination, (4) combined inhibition >50% and
233 Δinhibition$_{max}$ >20%. These 32 drug pairs were advanced to the comprehensive screening step.
234
235 Drug pairs were comprehensively screened in HDMB03 cells using a 10 × 10 dose-response
236 matrix, yielding 100 drug-dose combinations per pair. Screening was performed in triplicates. For
237 each replicate matrix, we evaluated the synergy of each drug-dose combination using the Zero
238 Interaction Potency (ZIP) model, a hybrid of the Loewe additivity and Bliss independence
239 models(31,32); these values were then averaged to produce an overall ZIP score for the matrix.
240 Each unique drug pair was assigned a ZIP score equalling the average of its three replicate
241 matrices. Notably, 19 of the 32 drug pairs (59.4%) were found to be synergistic (ZIP score >0,
242 **Fig. 1D**; **Supplementary Table S6**), confirming SINBA's effectiveness in identifying synergistic
243 therapeutics.
244
245 Trametinib, a MEK inhibitor, and regorafenib, a multi-kinase inhibitor, emerged as the most
246 synergistic drug pair. These drugs demonstrated profound synergy not only overall, but also in
247 the low dose regions of their synergy score landscapes (**Supplementary Fig. S2D**).
248
249 ***Fine-tuning the drug pair for optimal BBB-penetrability***
250 To confirm the blood-brain-barrier permeability of these drugs, we conducted preclinical
251 pharmacokinetic studies for regorafenib in female CD-1 nude mice (see **Methods**). Following a
252 single oral dose of regorafenib (10 mg/kg), we observed consistent plasma and brain
253 concentrations, with inter- and intra-mouse coefficients of variation ranging from 7.7% to 28.6%
254 (**Supplementary Fig. S3A**). Brain exposure was assessed by determining the unbound brain-to-
255 plasma partition ratio ($K_{p,uu}$), a critical parameter in evaluating CNS drug penetration and
256 distribution. Regorafenib demonstrated reasonable brain distribution ($K_{p,uu}$=0.143), which was
257 consistent with prior murine studies, though slightly lower than previously reported 24-hour

258 estimates(48). Notably, regorafenib has also been shown to have a robust CNS exposure
259 profile(49,50). Similar methods(51) found trametinib to have a less favorable brain distribution
260 ($K_{p,uu}$=0.069, **Supplementary Fig. S3B**). We therefore decided to include mirdametinib, another
261 MEK inhibitor whose BBB-permeability has been established in the literature(52,53), in our testing.
262 Consistent with existing studies, we found mirdametinib to have a superior $K_{p,uu}$ of 0.243
263 (**Supplementary Fig. S3C**). Having confirmed regorafinib's BBB permeability and selected an
264 additional MEK candidate, we advanced the regorafenib-MEK inhibitor combination to preclinical
265 validation.
266
267
268 **Regorafenib-MEK Inhibitor synergistic combination selectively kills G3 MB cells *in vitro***
269 Existing chemoproteomic profiling data has shown overlap between MEK inhibitors and
270 regorafenib's targets on the MAPK signaling pathway(54) (**Supplementary Fig. S3D**). This
271 pathway (KEGG MAPK signaling(55)) is significantly upregulated in G3 tumors compared to
272 normal cerebellum (**Supplementary Fig. S3E**), suggesting selective vulnerability in the G3
273 subtype. To better understand the mechanism underlying the synergy of MEK inhibitors and
274 regorafenib, we expanded our testing to include an additional four G3 MB cell line models (D341,
275 D425, D283, and MB002) as well as an SHH-MB cell line (DAOY with and without GFP).
276
277 First, we mapped the RNA-seq profiles of these cell lines(56) onto our MBi to generate paired
278 activity profiles for MAPK11 (a subunit of p38 MAP kinase) and BRAF, the target drivers for
279 regorafenib and trametinib/mirdametinib, respectively (**Fig. 2A**). We then calculated a signature
280 for the trametinib/regorafenib combination using iLINCS(57) data on the drugs' gene expression
281 signatures in a CNS-disease context. To do so, we used the activity profiles previously generated
282 for each cell line to rank the drivers in each line by activity score. Using these rankings as a
283 reference, we then calculated cell line-specific enrichment scores for the genes in which treatment

284 with regorafenib or trametinib induced up- or down-regulation. These enrichment scores were
285 used to calculate an integrated score for each cell line indicating its sensitivity to a trametinib-
286 regorafenib combination (**Fig. 2A and Supplementary Fig. S4A**, see **Methods**).
287
288 These sensitivity predictions were largely born out in *in vitro* testing, where we used AlamarBlue
289 cell viability assays to evaluate the regorafenib-trametinib and regorafenib-mirdametinib
290 combinations in the MB cell lines. For each cell line, 80 drug-dose combinations were tested per
291 drug pair (eight concentrations of MEK inhibitor and ten concentrations of regorafenib); the results
292 were then used to calculate an overall ZIP score for each drug pair as previously.
293
294 Overall, the greatest collective synergy was observed in the D341 cell line, which ranked No. 1
295 for regorafenib/mirametinib and No. 2 for regorafenib/trametinib (**Fig. 2B and 2C**). Reasonable
296 synergistic effects were also observed for both combinations in MB002 (**Fig. 2B and 2D**). As
297 expected, no synergy was observed for these combinations in the SHH-MB line DAOY
298 (**Supplementary Fig. S4B**). Despite being a G3 MB model, D425 was minimally responsive to
299 both drug pairs, consistent with the low synergy score we had predicted for that cell line
300 (**Supplementary Fig. S4C**). Some difference was observed in the performance of the drug pairs
301 within a single cell line. For instance, the trametinib combination produced the highest synergy in
302 D283, consistent with our predictions, whereas the mirdametinib combination produced no
303 synergy in that line (**Fig. 2B and Supplementary Fig. S4D**).
304
305 To confirm the mechanism of action of regorafenib and the MEK inhibitors in the context of
306 combination therapy, we compared the effects of combination therapy vs. monotherapy on
307 signaling in three responsive G3 MB cell lines (D341, HDMB03, and MB002). For Western blot
308 analysis, we selected three well-established targets of MEK inhibition (MEK, ERK, and BRAF),
309 while for regorafenib—a multi-kinase inhibitor—we chose MAPK11/p38, regorafenib's main target

310 in G3 MB according to our previous analysis with SINBA. Western blot analysis showed that the
311 regorafenib-MEK inhibitor combinations reduced the phosphorylation levels of all four targets
312 (MEK, ERK, BRAF, and p38), while total protein levels remained unchanged. In some cases,
313 combination therapy even produced a greater reduction in a target's phosphorylation compared
314 to monotherapy. These findings confirmed effective on-target suppression of BRAF-MEK
315 signaling by trametinib/mirdametinib and p38 signaling by regorafenib in G3 MB tumor cells in the
316 contexts of both mono- and combination therapy (**Fig. 2E**).
317
318 Together, these *in vitro* studies confirmed the synergistic killing effect of regorafenib-MEK inhibitor
319 combinations on G3 MB but not SHH-MB cells.
320
321
322 **Regorafenib-MEK inhibitor combinations are effective for G3 MB *in vivo***
323 Having identified D341 as the cell line most likely to be sensitive to the regorafenib-MEK inhibitor
324 combination (**Fig. 2A**) and having validated that prediction *in vitro* by demonstrating that
325 regorafenib and MEK inhibitors exhibit the greatest synergy in D341 cells (**Fig. 2B**), we moved to
326 investigate whether our findings would also hold *in vivo* (see **Methods**).
327
328 Given mirdametinib's superior brain penetration (compared to trametinib), as well as its greater
329 synergy with regorafenib in the D341 cell line, we chose to advance the regorafenib-mirdametinib
330 combination to *in vivo* testing (**Fig. 2B**). CD-1 nude mice orthotopically implanted with D341 cells
331 were treated with regorafenib (10 mg/kg), mirdametinib (5 mg/kg), or their combination (**Fig. 3A**).
332 Tumor progression was monitored weekly using IVIS imaging beginning one week post-
333 implantation. The combination therapy surpassed the control and monotherapies in slowing tumor
334 growth (**Fig. 3B** and **3C**), improving survival (**Fig. 3D**), and elevating apoptotic cell percentages
335 (**Fig. 3E**).

336

337 To assess the generalizability of this approach, we also tested the *in vivo* efficacy of the mono-
338 and combination therapies in the SHH model DAOY (**Fig. 3A** and **Supplementary Fig. S5A**).
339 Unlike the aggressive D341 model, the DAOY model exhibited a longer median survival of 90
340 days in the control group, compared to 34 days in D341. However, neither the single drug nor
341 combination treatments provided significant survival benefits in the DAOY model
342 (**Supplementary Fig. S5A** and **S5B**), underscoring the specificity of this therapeutic strategy for
343 G3 MB.

344

345 Recognizing the limitations of cell lines in fully recapitulating tumor biology, we extended our
346 investigation to MB patient-derived xenografts (PDXs)(58,59). G3 MB PDXs produced
347 significantly higher driver pair activity and drug sensitivity scores than normal cerebellum samples.
348 Among the PDX models, PDX5950 was predicted to be the most sensitive (**Fig. 4A**). Mice
349 orthotopically implanted with the PDX5950 model were treated with regorafenib and a reduced
350 dose of mirdametinib (0.5 mg/kg) due to the model's increased MEK inhibitor sensitivity (**Fig. 4B**).
351 Tumor progression was monitored weekly by MRI. As with the D341 model, combination therapy
352 significantly reduced tumor burden in the PDX5950 model (**Fig. 4D**) and substantially extended
353 survival (**Fig. 4C**). Mice treated with combination therapy had a median survival of 69 days,
354 compared to 55, 55, and 59 days for mice treated with vehicle, mirdametinib, or regorafenib,
355 respectively. We also found elevated apoptotic cell percentages in the combination therapy to a
356 greater degree than the controls and monotherapies (**Fig. 4E**).

357

358 Body weight loss was noted in the D341-implanted mice three weeks post-implantation regardless
359 of whether they received monotherapy, combination therapy, or vehicle control (**Supplementary**
360 **Fig. S5C**). Blood analyses showed no significant differences across treatment groups, with all
361 parameters except white blood cell (WBC) count remaining in the normal reference

362 (**Supplementary Fig. S5D**). These findings suggest that weight loss was tumor-burden-related
363 rather than treatment-induced. Mice implanted with PDX5950 experienced slight weight gain
364 during the treatment window, reflecting the less aggressive nature of that model. Blood analyses
365 similarly showed no significant differences across treatment groups, though the WBC counts of
366 mice in the single-treatment arms fell outside the normal range. Notably, WBC count in the
367 combination group remained within normal limits, suggesting a potential protective effect of the
368 combination therapy (**Supplementary Fig. S5E and S5F**).
369
370
371 **Regorafenib plus MEK inhibitor enhances low-dose radiation therapy *in vivo***
372 Radiotherapy remains a cornerstone of medulloblastoma treatment(60), yet patients with G3 MB
373 frequently experience tumor progression and poor survival outcomes(4,6,7,61). To investigate
374 whether regorafenib and MEK inhibitors could enhance the efficacy of radiotherapy, we tested
375 them in combination with low-dose irradiation using the D341 model. Mice were assigned to four
376 treatment groups: vehicle control, drug combination alone, drug combination administered
377 concurrently with radiation, and drug combination administered following radiation
378 (**Supplementary Fig. S6A**). Radiotherapy was delivered in fractions of 0.5 Gy per day for five
379 consecutive days. All treatment arms demonstrated improved survival compared to vehicle
380 controls, with sequential therapy providing the greatest benefit over radiation alone
381 (**Supplementary Fig. S6B and S6C**). Importantly, treatment-related toxicity (measured through
382 body weight and blood analyses) was not observed in any of the experimental groups
383 (**Supplementary Fig. S6D and S6E**).
384
385 These findings suggest that integrating regorafenib-MEK inhibitor combination therapy into
386 existing treatment protocols may offer substantial therapeutic advantages for high-risk G3 MB

387 patients, potentially improving outcomes for this challenging and aggressive subgroup of
388 medulloblastoma.
389
390
391 **Single-cell analysis reveals that regorafenib and MEK inhibitors target the developmental**
392 **origins of G3 MB**
393 Recent single-cell studies of human medulloblastoma have demonstrated significant intra- and
394 inter-tumoral heterogeneity and diverse developmental origins of MB subtypes(62-67). To
395 understand how regorafenib-MEK inhibitor combinations affect different cell subpopulations in
396 heterogeneous G3 MB, we analyzed drug target activity using single-cell RNA sequencing
397 (scRNA-seq) data from human developing cerebellum, MB patient tumor samples, and the D341
398 xenograft model (both with and without treatment).
399
400 To investigate the developmental origins of each MB subtype, we used publicly available scRNA-
401 seq data(66) to construct a developmental reference for human cerebellum, focusing on the
402 glutamatergic lineage in which most MB occur. Our clustering analysis identified seven distinct
403 developmental states based on previously published markers(68-70): neural stem cells (NSC),
404 rhombic lip progenitors (RL_pro), unipolar brush cell and granule cell precursor common
405 progenitors (UBC_GCP_pro), unipolar brush cell progenitors (UBC_pro), granule cells (GC), and
406 unipolar brush cells (UBC) (**Fig. 5A and 5B**; **Supplementary Table S7**). Pseudotime analysis
407 with Slingshot and Monocle 3 produced a putative developmental trajectory in which NSCs
408 progress along a single path to RL_pro and subsequently UBC_GCP_pro, at which point the
409 trajectory bifurcates, ultimately giving rise to the UBC and GC lineages **(Supplementary Fig. S7A**
410 **and S7B**; see **Methods**). This single-cell reference for human glutamatergic development is
411 available via an interactive web portal (https://scminer.stjude.org/study/Glutamatergic-lineage).
412

413 Next, we performed clustering analysis of published MB patient scRNA-seq data(62,63,66)
414 (**Supplementary Table S8**), and then used our developmental reference to assign developmental
415 stages to each cluster. To do so, we extracted the malignant MB cells from the GSE155446
416 dataset (10,537 cells from one WNT, nine SHH, and 18 G3/G4 MB patients; **Supplementary Fig.**
417 **S7C** and **S7D**; **Supplementary Table S9**), annotating the clusters using marker genes for the
418 seven developmental stages of the glutamatergic lineage (**Fig. 5C and Supplementary Fig. S7E**).
419 Our mapped results revealed a predominance of GCP-like cells in SHH tumors, UBC_pro and
420 UBC_GCP_pro cells in G3 tumors, UBC-like cells in G4 tumors, and RL_pro-like cells in WNT
421 tumors. Notably, the UBC_GCP_pro cluster closely resembled the NSC-like cells reported in the
422 original study (**Supplementary Fig. S7D and S7E**). These findings, which suggest potential
423 developmental origins for each MB subtype (**Fig. 5D**), were later validated using two independent
424 scRNA-seq datasets[62,66] (**Supplementary Fig. S7F-I**; **Supplementary Table S10-S11**). The
425 analyzed GSE155446 data, including gene expression and activity profiles, are available through
426 an interactive portal (https://scminer.stjude.org/study/GSE155446).
427
428 In addition to the scRNA-seq analysis, we also employed our recently developed ReDeconv(71)
429 algorithm to deconvolute bulk RNA-seq data from MB patient cohorts and PDX models (see
430 **Methods**). Analysis of the mean percentage of each developmental state among patients with
431 the same tumor subtype(9,58,72) revealed the same patterns observed in the scRNA-seq data
432 (**Supplementary Fig. S8A**): SHH tumors were enriched with GCP-like cells, G3 tumors with
433 UBC_pro and UBC_GCP_pro cells, and G4 tumors with UBC-like cells.
434
435 Next, we investigated the activity of BRAF and MAPK11, the primary targets of MEK inhibitors
436 and regorafenib in G3 MB, across lineage stages. Using our scMINER algorithm(73) and the Mbi,
437 we calculated driver activity at the single-cell level, revealing an elevation in the paired activity of
438 BRAF and MAPK11 in the UBC_GCP_pro and UBC_pro-like subpopulations that are

439 predominant in G3 tumors. No such elevation was observed for G3 minority subpopulations like
440 GC and UBC, which represent more differentiated developmental states (**Fig. 5E**). The drug
441 signature scores for regorafenib + MEK inhibitor showed a similar pattern of elevation in
442 UBC_GCP_pro and UBC_pro-like cells. In contrast, both BRAF and MAPK11 activity and the
443 drug signature scores were minimal in those patients' normal immune cells. Notably, expression
444 of BRAF and MAPK11 was low across all malignant cell types, demonstrating the usefulness of
445 the activity-based approach (**Supplementary Fig. S8B, S8C and S8D**). As expected, the drug
446 signature scores were low in normal human cerebellum. BRAF and MAPK11 expression were
447 also low in normal cerebellum; however, BRAF+MAPK11 *activity* was markedly elevated in those
448 samples' UBC_GCP_pro cells (**Supplementary Fig. S8E and S8F**).
449
450 These findings led us to hypothesize that regorafenib-MEK inhibitor combinations target the
451 potential developmental origins of G3 MB, namely UBC_GCP_pro and UBC_pro cells. To test
452 this hypothesis, we performed scRNA-seq profiling of D341 cells both prior to implantation in mice
453 and then after implantation and treatment with vehicle control, mirdametinib, regorafenib, or their
454 combination. Analysis of the pre-implantation D341 cells revealed high proportions of
455 UBC_GCP_pro and UBC_pro-like subpopulations, much like the G3 MB patient samples
456 (**Supplementary Fig. S8G and S8H**). D341 lacked mature-like populations (GC and UBC) and
457 exhibited slightly higher proportions of GCP-like cells, likely due to culture conditions favoring
458 proliferative progenitor-like states. The combined driver activity and drug signature scores were
459 again exceptionally high in the UBC_GCP_pro-like tumor cells (**Supplementary Fig. S8I**).
460
461 Consistent with our findings *in vitro*, D341 tumor cells extracted from the mice post-treatment
462 consisted primarily of UBC_GCP_pro and UBC_pro-like cells (**Fig. 5F and 5G**; **Supplementary**
463 **Table S12**). There was a reduction in driver activity in the cells from the MIR and MIR+REG
464 groups. Furthermore, the drug signature score was significantly lower in the MIR+REG group than

465 in the vehicle control or single-agent group (**Fig. 5H and 5I**). The treatment effect was specific to
466 cell state. The UBC_GCP_pro-like population demonstrated higher baseline driver activity and
467 was more sensitive to treatment, leading to a decreased UBC_GCP_pro-to-UBC_pro cell ratio in
468 the MIR and MIR+REG groups (**Fig. 5G and 5J**). The appearance of drug-resistant NSC-like
469 tumor cells in the combination treatment group could be a source of treatment resistance.
470
471 Our single-cell analyses traced the major cellular origins of G3 MB to UBC_GCP_pro and
472 UBC_pro cells in the glutamatergic lineage of developing cerebellum. Single-cell analysis of G3
473 MB cells treated *in vivo* confirm that UBC_GCP_pro and UBC_pro-like cells have greater driver
474 activity and drug signature scores than other G3 MB tumor cell subpopulations; and that
475 combination treatment is more effective than monotherapy and control at eliminating these tumor
476 cells but may give rise to resistant populations.
477
478
479 **Regorafenib plus MEK inhibitor is effective and reprograms the suppressive TME in an**
480 **immunocompetent syngeneic mouse model of G3 MB**
481 While our *in vivo* studies of human cell line xenografts (D341) and PDX models (PDX5950) were
482 effective in establishing the efficacy of regorafenib-MEK inhibitor combinations in G3 MB tumors,
483 these models require immune-deficient CD-1 nude mice, making them unsuitable for investigating
484 drug treatment in the context of the tumor immune microenvironment. We therefore utilized CTD,
485 a syngeneic G3 MB mouse model, to assess these combinations' efficacy in an
486 immunocompetent setting and their impact on the TME.
487
488 CTD is a genetically engineered mouse model that resembles human G3 MB both histologically
489 and molecularly(74). In the CTD model, *Ctdnep1,* one of the most frequently altered tumor
490 suppressors in G3 MB, is conditionally knocked out in neuronal progenitor cells or cerebellar stem

491 cells, leading to MYC amplification and p53 inactivation, both hallmarks of G3 MB(74). To confirm
492 the faithfulness of the model, we used scRNA-seq to characterize cultured CTD tumor cells. Most
493 of the CTD tumor cells were UBC_GCP_pro and UBC_pro-like, recapitulating the developmental
494 origins of G3 MB (**Supplementary Fig. S9A**). Consistent with our findings in human G3 MB, the
495 UBC_GCP_pro and UBC_pro-like cells had higher BRAF and MAPK11 activity and drug signature
496 scores than RL_pro-like cells (**Supplementary Fig. S9B**). These results suggested that the CTD
497 model was suited to our needs.
498
499 First, we tested the drug combination's efficacy and synergy in CTD cells *in vitro*. Similar to in the
500 human PDX5950 model (**Fig. 4B**), the CTD mouse line exhibited notable sensitivity to MEK
501 inhibitors. Adding even a low dose of MEK inhibitor significantly lowered the EC_{50} of regorafenib
502 (**Fig. 6A and 6B**). Consistent with what was observed in human G3 MB cell lines (**Fig. 2E**),
503 combination therapy simultaneously downregulated phosphorylated MEK (p-MEK), p-ERK, p-p38,
504 and p-BRAF, while total protein levels remained unchanged (**Fig. 6C**).
505
506 We then evaluated the therapeutic efficacy of this combination *in vivo* using CTD-bearing
507 C57BL/6 mice (**Fig. 6D**). Mirdametinib, selected for its high brain penetration, was administered
508 at a low dose of 0.5 mg/kg given the high sensitivity of CTD to MEK inhibitors *in vitro*. Tumor
509 volume was monitored via MRI weekly, and the relative tumor burden assessed four weeks post-
510 surgery. Only the combination treatment group demonstrated a significant reduction in tumor
511 burden compared to control (**Fig. 6E**). Combination treatment likewise significantly extended
512 overall survival compared to monotherapy and control (**Fig. 6F**).
513
514 To investigate the effect of combination therapy on tumor cell states and the microenvironment,
515 we performed scRNA-seq of endpoint tumor samples from each therapy group. To increase TME
516 cell signal, we used CD45 antibody sorting to enrich the samples in immune TME cells, aiming

517 for an equal ratio of $CD45^+$ and $CD45^-$ cells (**Fig. 7A**). scRNA-seq captured a total of 39,658 cells,
518 including both tumor cells and a variety of TME cell types: macrophages, monocytes, microglia,
519 dendritic cells, T cells, natural killer cells, neutrophils, basophils, endothelial cells, and
520 oligodendrocyte progenitor cells (**Fig. 7B and Supplementary Fig. S9C**)
521
522 CTD tumors treated with regorafenib, both alone and in combination with mirdametinib, had a
523 lower proportion of UBC_GCP_pro-like and UBC_pro-like tumor cells and a higher proportion of
524 RL-pro-like cells compared to control and mirdametinib alone (**Fig. 7C and 7D**). Tumor cells
525 treated with REG and REG + MIR also showed reduced driver activity and drug signature scores
526 overall (**Supplementary Fig. S9D**). Not surprisingly, RL-pro-like tumors have lower drug
527 signature scores and driver activity compared to the drug-sensitive UBC_GCP_pro and UBC_pro-
528 like tumors (**Supplementary Fig. S9E**). Altogether, these data suggest that treating CTD tumors
529 with REG or REG + MIR reduces populations of drug-sensitive UBC_GCP_pro-like and UBC_pro-
530 like cells and increases populations of drug-tolerant RL-pro-like cells, producing the lower overall
531 driver activity and drug signature scores observed in these treatment groups.
532
533 To investigate whether drug treatment impacts tumor cells in other ways, we performed differential
534 expressed gene (DEG) analysis on the scRNA-seq data generated for our treatment groups.
535 Tumor cells treated with combination therapy showed up-regulation of MHC complex genes (*H2-*
536 *D1*, *H2-K1, H2-Aa, H2-Ab1, B2m* and *H2-Eb1*) and downregulation of *Lgals3*, a ligand of LAG3,
537 an immune checkpoint receptor expressed on T cells(75) (**Fig. 7E**). The function enrichment
538 analysis show the upregulated DE genes (avg_log2FC > 1, adjusted p value < 0.05) are related
539 to tumor antigen presentation(76) (**Fig. 7F**). We summarized antigen presentation related genes
540 into a module score and found across all treatment groups, with combination therapy producing
541 the highest score (**Fig. 7G and Supplementary Fig. S9F**).
542

543 Next, we used the scRNA-seq data to compare the immune cell type proportions of our treatment
544 groups (**Supplementary Table S13**). Sixteen immune cell types were captured, including seven
545 T cell populations (**Fig. 7B and 7H**). Monocytes (Mono) and T effector cells (Teffector) were
546 increased, and T regulatory cells (Treg) were decreased, in the combination therapy group
547 compared to control and monotherapy (**Fig. 7H and 7I**). Notably, the combination therapy group
548 had increased macrophages (**Fig. 7I**), but a greater proportion of those were of the M1 phenotype
549 (**Supplementary Fig. S9G**; **Supplementary Table S14**), consistent with a previous report that
550 regorafenib enhances M1/M2 polarization in head and neck cancers(77). In terms of T cells, we
551 found a reduction in immunosuppressive Tregs and an increase in CD8+ T effector cells in the
552 combination therapy group (**Fig. 7I**); in fact, this group had the highest ratio of CD8+ T effector
553 cells to Tregs (**Fig. 7J**), indicating more robust anti-tumor immunity compared to the other groups.
554 This owes to the increased antigen presentation previously observed in tumor cells.
555
556 Then to understand how the drugs changed TME globally, we calculated drug scores for immune
557 cells. Immune cells in the combination therapy group scored highest for MIR and REG, indicating
558 that these treatments may alter the transcriptomes of immune cells (**Supplementary Fig. S10A**,
559 see **Methods**). Tregs had the highest scores for both drugs; T effector cells and monocytes also
560 presented high scores (**Supplementary Fig. S10B**). These results suggest that drug treatment
561 may directly shape the cell type composition of the TME.
562
563 We also found that CD8+ T cells (Tex, T effector cells, Tcm and proliferative T cells) were more
564 activated, as indicated by increased expression of *Ifng*, *Prf1*, in the combination treatment group
565 (**Supplementary Fig. S10C**). These T cells also expressed more *Ccl3* and *Ccl4*, which have been
566 shown to increase T cell activation(78,79). CCL3 and CCL4 secretion has also been reported in
567 T effector cells activated by infections(80). CD8+ T cells in the combination therapy group also
568 showed upregulation of *Cxcr6* and downregulation of *Cxcr4*. *Cxcr6* has been noted to promote T

569 cell activation and recruit T cells into tumors, while *Cxcr4* mainly mediates the exclusion of T cells
570 from the tumor center. Collectively, these evidence suggest that combination treatment could
571 promote CD8+ T cells anti-tumor immunity(81-83)(84). CD8+ T cells in the combination treatment
572 group also showed increased expression of several immune checkpoints and immunotherapy
573 targets(85,86), including PD1, LAG3, TIM3, CD160, and CD39 (**Supplementary Fig. S10C and**
574 **D**), indicative of CD8+ T cell exhaustion—a potential source of the resistance observed in this
575 treatment group. Supplementing regorafenib + MEK inhibitors with immunotherapy may therefore
576 achieve better efficacy in clinical settings and is a strategy worth exploring (**Supplementary Fig.**
577 **S10E**).
578
579 Previous studies have shown that besides direct activation by TCR, expression of CCL3 and
580 CCL4 in T cells can also be induced by IL12, IL18 and IFNg(80,87). Among the cell types captured
581 in the TME, monocytes exhibited the greatest expression of *Il18*, while its receptors (*Il18r* and
582 *Il18rap*) were highly expressed on T cells (**Supplementary Fig. S10F-S10I**). Given the higher
583 proportion of monocytes in the combination therapy group, the increased T cell activation
584 observed in this group could be explained by increased secretion of CCL3 and CCL4 in CD8+ T
585 cells induced by monocyte-derived IL18 (**Supplementary Fig. S10J and S10K**). This explanation
586 was partially supported by CellChat analysis(88) of ligand-receptor interactions on the IL18-IL18R
587 and CCL3/4-CCR5 axis. T effector cells in the combination therapy group received more
588 communications from IL18 (**Fig. 7K**, see **Methods**). However, no trend was observed in the IL18
589 communications received by immune-suppressive Tregs. For the CCL3/4-CCR5 axis, we found
590 an increase in communications received by T effector cells in both the mono- and combination
591 therapy groups, with communication levels greatest in the latter. Notably, MIR treatment blocked
592 CCL3/4-CCR5 communications received by Tregs. Together, these data demonstrate
593 combination therapy-induced activation of the CCL3/4-CCR5 axis in T effector cells but not

594 immunosuppressive Tregs, potentially explaining the greater active antitumoral immunity in the
595 combination therapy group.
596
597 In summary, regorafenib and MEK inhibitors not only demonstrated robust anti-tumor efficacy in
598 a syngeneic mouse model of G3 MB, but also triggered anti-tumor immunity through the activation
599 of cytotoxic CD8+ T cells, suggesting the combination's promise for overcoming tumor
600 progression and immune evasion in the clinic.
601
602 **DISCUSSION**
603
604 To our knowledge, this study is the first to use systems biology approaches to guide high-
605 throughput combination drug screening in high-risk medulloblastoma. The SINBA platform brings
606 together gene activity data, a brain-penetrating drug database, and single-agent high-throughput
607 screening results to nominate synergistic drug pairs for combination screening. Through single-
608 agent screening, we identified both novel and previously reported G3 MB-specific drugs, such as
609 mycophenolate mofetil and digoxin(89). Applied to transcriptomic data from three MB patient
610 cohorts, SINBA predicted a regorafenib-MEK inhibitor combination for G3 MB; these drugs were
611 later confirmed to be synergistic both *in vitro* (through drug screening) and *in vivo* (through efficacy
612 studies). We found that tumor cells sensitive to the regorafenib-MEK inhibitor combinations share
613 transcriptomic signatures with early unipolar brush cell (UBC) progenitors, which have previously
614 been proposed as the cell-of-origin for G3 MB(62,64,65,90,91). We also showed that a
615 regorafenib-MEK inhibitor combination reprograms the tumor microenvironment, enhancing
616 CD8+ T cell recruitment in an immunocompetent G3 MB mouse model.
617
618 G3 medulloblastoma is an aggressive cerebellar tumor arising from malignantly transformed early
619 UBC progenitors within the rhombic lip subventricular zone (RL^{svz})(64,65,91). Single-cell analyses

620 comparing MB cells to normal cerebellar references have found that MB cells arise from early
621 developmental arrest(92) driven by genetic mutations or epigenetic dysregulation[(64),](9,93). Novel
622 immunotherapies, such as CAR-T cells targeting Protogenin-expressing stem cells, have shown
623 efficacy in preclinical G3 MB models in immunocompromised mice(91). However, drug
624 repurposing strategies that target origin cell populations *in vivo* are lacking. While SINBA is not
625 expressly designed to select drugs that target originating populations, it may nonetheless propose
626 drug pairs that do so, as it did for G3 MB.
627
628 Robust clinical and preclinical evidence suggest that combining regorafenib with MEK inhibitors
629 may effectively treat brain tumors(94-97). In the phase II REGOMA trial, treating relapsed
630 glioblastoma patients with regorafenib produced better therapeutic outcomes than lomustine[28].
631 The MEK inhibitor trametinib, in combination with the BRAF inhibitor dabrafenib, received FDA
632 approval in 2022 for the treatment of advanced tumors with BRAF V600E mutations, including
633 adult and pediatric gliomas. Another MEK inhibitor, mirdametinib, recently gained FDA approval
634 for treating plexiform neurofibromas in both adult and pediatric populations. Notably, combining
635 mirdametinib with the PI3K/mTOR inhibitor paxalisib significantly extends survival in mouse
636 models of pediatric high-grade gliomas(53). Given its more favorable pharmacokinetics and CNS
637 activity, mirdametinib replaced trametinib as the MEK inhibitor in our experiments *in vivo*.
638
639 Through the SINBA algorithm, trametinib and regorafenib were identified as a potentially
640 synergistic drug combination that targets BRAF and MAPK11 (a p38 subunit), hidden drivers in
641 G3 MB. Although this drug combination has not previously been tested in MB, MEK inhibitors and
642 regorafenib have demonstrated synergistic effects in colorectal cancer(98,99), gastric cancer(100)
643 and melanoma models harboring BRAF V600E mutations(101). While BRAF mutations are rare
644 in MB, upregulation of MEK kinase activity—a downstream target of BRAF—is common, even in
645 the absence of changes to the total protein levels(47). Overexpression of the PDGFA/RAS/MAPK

646 signaling pathway has been implicated in MB metastasis(102,103), and inhibition of MEK1/2 with
647 U0126 has been shown to reduce viability in MB(104). Additionally, treatment-resistant MB cells
648 maintain a stem cell-like state through overexpression of the BPIFB4 (bactericidal/permeability-
649 increasing fold-containing family B member 4) longevity factor. Reducing BPIFB4 levels in
650 recurrent MB cells diminishes their aggressiveness both *in vitro* and *in vivo*, with the ERK1/2 and
651 p38α proteins most affected by BPIFB4 knockdown(105). These findings align with previous
652 studies demonstrating that targeting ERK (a downstream target of MEK) and p38-MAPK signaling
653 with liposomal honokiol induces ROS-mediated apoptosis in MB cell line models(106).
654
655 The regorafenib-MEK inhibitor combination inhibits cancer progression both directly, by targeting
656 cancer-driving genes, and indirectly, through modulation of the TME. MEK inhibition protects
657 tumor-infiltrating CD8+ T cells from exhaustion driven by chronic TCR stimulation while preserving
658 cytotoxic activity(107). Regorafenib promotes a tumor suppressive microenvironment by
659 promoting Macrophage M1/M2 polarization and by decreasing expression of PD-L1 and
660 increasing expression of MHC-I class genes in tumor cells(77,108,109). These observations are
661 consistent with our finding that regorafenib-MEK inhibitor therapy promotes an antitumor TME in
662 G3 MB. Combination therapy-induced up-regulation of CD8+ T cell immunotherapy targets could
663 explain the resistance observed, as well as offer a potential solution: adding an immune
664 checkpoint blockade, such as PD-L1/PD1, LAG3, or TIM3. At present, no immunotherapy has
665 been approved for G3 MB tumors, which are typically immunotherapy-resistant and considered
666 immunologically "cold". Adjunctive regorafenib-MEK inhibitor therapy could sensitize these
667 tumors to immunotherapy, providing a path forward for that treatment modality in G3 MB.
668
669 This study establishes SINBA as a powerful tool for uncovering synergistic drug combinations
670 that target critical hidden drivers in high-risk MB and beyond. A regorafenib + MEK inhibitor
671 combination based on SINBA's predictions was found to disrupt key oncogenic pathways and

actively reprogram the TME towards an anti-tumor state, presenting a compelling therapeutic strategy for G3 MB. Future directions include further refinement of SINBA's drug-target database as well as translational investigations aimed at bringing the regorafenib + MEK inhibitor combination into clinical use. Further studies should evaluate the combination as an adjunct to standard chemotherapy, radiation, and immune checkpoint inhibitors, particularly the latter given MB's immune-cold nature and the combination's TME-modulatory effects. To maximize efficacy and address potential resistance, investigations should also be made into this combination's impact on tumor cell plasticity and dynamic immune system interactions.

680 **Authors' Disclosures**

681

682 The authors declare no competing interests.

683

684 **Authors' Contributions**

685

686 J.Y. and J.L. conceptualized the study; J.L., X.Y. and M.Z. performed all the experiments with
687 B.B., B.M.J., W.L., and X.F.; J.L. performed all the data analysis with X.Y., M.Z., X.D., H.Z., B.M.J.,
688 L.Y., B.B.F.III, A.W. and R.J.; T.C., G.W.R., M.F.R., T.E.M. and A.G. provided relevant intellectual
689 input and edited the manuscript. J.L., X.Y., and M.Z. interpreted the results. J.L., X.Y., M.Z. and
690 J.Y. wrote the manuscript. All the authors reviewed and commented on the manuscript.

691

692 **Acknowledgements**

693

694 We extend our sincere gratitude to Sarah August for her exceptional contributions to this project,
695 including her dedicated efforts in manuscript preparation and revision, her creative input, and her
696 expertise in data presentation. We are also deeply grateful to the following St. Jude Children's
697 Research Hospital core facilities for their consistent support and expertise: the Center for *In Vivo*
698 Imaging and Therapy (Melissa Johnson and team), the Animal Research Center (Chandra
699 Savage and team), the Flow Cytometry and Cell Sorting Core, and the Comparative Pathology
700 Core. We thank Dr. Anang A. Shelat for his expert assistance in analyzing the high-throughput
701 screening data and Dr. Suzanne J. Baker for her insightful suggestions on the design of our *in*
702 *vivo* experiments. We are also grateful to Dr. Till Milde for sharing the HDMB03 line and Dr. Q.
703 Richard Lu for generously sharing multiple MB models including CTD. This work is supported, in
704 part, by National Institutes of Health grants R01GM134382 (to J.Y.), U01CA264610 (to J.Y.), and
705 U01CA281868 (to J.Y.), by the COOKIES FOR KIDS CANCER translational award (to J.Y.), by

706 the Big Hope Little Warrior Cancer Foundation, and by the American Lebanese Syrian Associated
707 Charities.

REFERENCES

1. Siegel DA, Richardson LC, Henley SJ, Wilson RJ, Dowling NF, Weir HK*, et al.* Pediatric cancer mortality and survival in the United States, 2001-2016. Cancer **2020**;126(19):4379-89 doi 10.1002/cncr.33080.
2. Kool M, Korshunov A, Remke M, Jones DT, Schlanstein M, Northcott PA*, et al.* Molecular subgroups of medulloblastoma: an international meta-analysis of transcriptome, genetic aberrations, and clinical data of WNT, SHH, Group 3, and Group 4 medulloblastomas. Acta Neuropathol **2012**;123(4):473-84 doi 10.1007/s00401-012-0958-8.
3. Taylor MD, Northcott PA, Korshunov A, Remke M, Cho YJ, Clifford SC*, et al.* Molecular subgroups of medulloblastoma: the current consensus. Acta Neuropathol **2012**;123(4):465-72 doi 10.1007/s00401-011-0922-z.
4. Gajjar A, Chintagumpala M, Ashley D, Kellie S, Kun LE, Merchant TE*, et al.* Risk-adapted craniospinal radiotherapy followed by high-dose chemotherapy and stem-cell rescue in children with newly diagnosed medulloblastoma (St Jude Medulloblastoma-96): long-term results from a prospective, multicentre trial. The Lancet Oncology **2006**;7(10):813-20 doi 10.1016/s1470-2045(06)70867-1.
5. Gajjar A, Robinson GW, Smith KS, Lin T, Merchant TE, Chintagumpala M*, et al.* Outcomes by Clinical and Molecular Features in Children With Medulloblastoma Treated With Risk-Adapted Therapy: Results of an International Phase III Trial (SJMB03). J Clin Oncol **2021**:JCO2001372 doi 10.1200/JCO.20.01372.
6. Koschmann C, Bloom K, Upadhyaya S, Geyer JR, Leary SE. Survival After Relapse of Medulloblastoma. J Pediatr Hematol Oncol **2016**;38(4):269-73 doi 10.1097/MPH.0000000000000547.
7. Sabel M, Fleischhack G, Tippelt S, Gustafsson G, Doz F, Kortmann R*, et al.* Relapse patterns and outcome after relapse in standard risk medulloblastoma: a report from the HIT-SIOP-PNET4 study. J Neurooncol **2016**;129(3):515-24 doi 10.1007/s11060-016-2202-1.
8. Aldape K, Brindle KM, Chesler L, Chopra R, Gajjar A, Gilbert MR*, et al.* Challenges to curing primary brain tumours. Nat Rev Clin Oncol **2019**;16(8):509-20 doi 10.1038/s41571-019-0177-5.
9. Northcott PA, Buchhalter I, Morrissy AS, Hovestadt V, Weischenfeldt J, Ehrenberger T*, et al.* The whole-genome landscape of medulloblastoma subtypes. Nature **2017**;547(7663):311-7 doi 10.1038/nature22973.
10. Ibrahim YH, Garcia-Garcia C, Serra V, He L, Torres-Lockhart K, Prat A*, et al.* PI3K inhibition impairs BRCA1/2 expression and sensitizes BRCA-proficient triple-negative breast cancer to PARP inhibition. Cancer Discov **2012**;2(11):1036-47 doi 10.1158/2159-8290.CD-11-0348.
11. Robert C, Karaszewska B, Schachter J, Rutkowski P, Mackiewicz A, Stroiakovski D*, et al.* Improved overall survival in melanoma with combined dabrafenib and trametinib. N Engl J Med **2015**;372(1):30-9 doi 10.1056/NEJMoa1412690.
12. DiNardo CD, Jonas BA, Pullarkat V, Thirman MJ, Garcia JS, Wei AH*, et al.* Azacitidine and Venetoclax in Previously Untreated Acute Myeloid Leukemia. N Engl J Med **2020**;383(7):617-29 doi 10.1056/NEJMoa2012971.
13. Turner NC, Ro J, Andre F, Loi S, Verma S, Iwata H*, et al.* Palbociclib in Hormone-Receptor-Positive Advanced Breast Cancer. N Engl J Med **2015**;373(3):209-19 doi 10.1056/NEJMoa1505270.
14. Mok TSK, Wu YL, Kudaba I, Kowalski DM, Cho BC, Turna HZ*, et al.* Pembrolizumab versus chemotherapy for previously untreated, PD-L1-expressing, locally advanced or metastatic non-small-cell lung cancer (KEYNOTE-042): a randomised, open-label,

controlled, phase 3 trial. Lancet **2019**;393(10183):1819-30 doi 10.1016/S0140-6736(18)32409-7.

15. Larkin J, Hodi FS, Wolchok JD. Combined Nivolumab and Ipilimumab or Monotherapy in Untreated Melanoma. N Engl J Med **2015**;373(13):1270-1 doi 10.1056/NEJMc1509660.
16. Chen EX, Jonker DJ, Loree JM, Kennecke HF, Berry SR, Couture F*, et al.* Effect of Combined Immune Checkpoint Inhibition vs Best Supportive Care Alone in Patients With Advanced Colorectal Cancer: The Canadian Cancer Trials Group CO.26 Study. JAMA Oncol **2020**;6(6):831-8 doi 10.1001/jamaoncol.2020.0910.
17. Eng C, Kim TW, Bendell J, Argilés G, Tebbutt NC, Di Bartolomeo M*, et al.* Atezolizumab with or without cobimetinib versus regorafenib in previously treated metastatic colorectal cancer (IMblaze370): a multicentre, open-label, phase 3, randomised, controlled trial. Lancet Oncol **2019**;20(6):849-61 doi 10.1016/s1470-2045(19)30027-0.
18. Pei Y, Liu KW, Wang J, Garancher A, Tao R, Esparza LA*, et al.* HDAC and PI3K Antagonists Cooperate to Inhibit Growth of MYC-Driven Medulloblastoma. Cancer Cell **2016**;29(3):311-23 doi 10.1016/j.ccell.2016.02.011.
19. Preuer K, Lewis RPI, Hochreiter S, Bender A, Bulusu KC, Klambauer G. DeepSynergy: predicting anti-cancer drug synergy with Deep Learning. Bioinformatics **2018**;34(9):1538-46 doi 10.1093/bioinformatics/btx806.
20. Liu W, Wang Z, Liu X, Zeng N, Liu Y, Alsaadi FE. A survey of deep neural network architectures and their applications. Neurocomputing **2017**;234:11-26 doi 10.1016/j.neucom.2016.12.038.
21. Adam G, Rampasek L, Safikhani Z, Smirnov P, Haibe-Kains B, Goldenberg A. Machine learning approaches to drug response prediction: challenges and recent progress. NPJ Precis Oncol **2020**;4:19 doi 10.1038/s41698-020-0122-1.
22. Jassim A, Nimmervoll BV, Terranova S, Nathan E, Hu L, Taylor JT*, et al.* Gene context drift identifies drug targets to mitigate cancer treatment resistance. Cancer Cell **2025**;43(9):1608-21 e9 doi 10.1016/j.ccell.2025.06.005.
23. Bansal M, Yang J, Karan C, Menden MP, Costello JC, Tang H*, et al.* A community computational challenge to predict the activity of pairs of compounds. Nat Biotechnol **2014**;32(12):1213-22 doi 10.1038/nbt.3052.
24. Kuenzi BM, Park J, Fong SH, Sanchez KS, Lee J, Kreisberg JF*, et al.* Predicting Drug Response and Synergy Using a Deep Learning Model of Human Cancer Cells. Cancer Cell **2020**;38(5):672-84 e6 doi 10.1016/j.ccell.2020.09.014.
25. Robinson G, Parker M, Kranenburg TA, Lu C, Chen X, Ding L*, et al.* Novel mutations target distinct subgroups of medulloblastoma. Nature **2012**;488(7409):43-8 doi 10.1038/nature11213.
26. Califano A, Alvarez MJ. The recurrent architecture of tumour initiation, progression and drug sensitivity. Nat Rev Cancer **2017**;17(2):116-30 doi 10.1038/nrc.2016.124.
27. Piovan E, Yu J, Tosello V, Herranz D, Ambesi-Impiombato A, Da Silva AC*, et al.* Direct reversal of glucocorticoid resistance by AKT inhibition in acute lymphoblastic leukemia. Cancer Cell **2013**;24(6):766-76 doi 10.1016/j.ccr.2013.10.022.
28. Autry RJ, Paugh SW, Carter R, Shi L, Liu J, Ferguson DC*, et al.* Integrative genomic analyses reveal mechanisms of glucocorticoid resistance in acute lymphoblastic leukemia. Nature Cancer **2020**;1(3):329-44 doi 10.1038/s43018-020-0037-3.
29. Zeleke TZ, Pan Q, Chiuzan C, Onishi M, Li Y, Tan H*, et al.* Network-based assessment of HDAC6 activity predicts preclinical and clinical responses to the HDAC6 inhibitor ricolinostat in breast cancer. Nat Cancer **2023**;4(2):257-75 doi 10.1038/s43018-022-00489-5.
30. Gocho Y, Liu J, Hu J, Yang W, Dharia NV, Zhang J*, et al.* Network-based systems pharmacology reveals heterogeneity in LCK and BCL2 signaling and therapeutic

808 sensitivity of T-cell acute lymphoblastic leukemia. Nature Cancer **2021** doi
809 10.1038/s43018-020-00167-4.
810 31. Ianevski A, Giri AK, Aittokallio T. SynergyFinder 2.0: visual analytics of multi-drug
811 combination synergies. Nucleic Acids Res **2020**;48(W1):W488-W93 doi
812 10.1093/nar/gkaa216.
813 32. Yadav B, Wennerberg K, Aittokallio T, Tang J. Searching for Drug Synergy in Complex
814 Dose-Response Landscapes Using an Interaction Potency Model. Comput Struct
815 Biotechnol J **2015**;13:504-13 doi 10.1016/j.csbj.2015.09.001.
816 33. Meng F, Xi Y, Huang J, Ayers PW. A curated diverse molecular database of blood-brain
817 barrier permeability with chemical descriptors. Sci Data **2021**;8(1):289 doi
818 10.1038/s41597-021-01069-5.
819 34. Wishart DS, Feunang YD, Guo AC, Lo EJ, Marcu A, Grant JR*, et al.* DrugBank 5.0: a
820 major update to the DrugBank database for 2018. Nucleic Acids Res **2018**;46(D1):D1074-
821 D82 doi 10.1093/nar/gkx1037.
822 35. Cheng F, Kovacs IA, Barabasi AL. Network-based prediction of drug combinations. Nat
823 Commun **2019**;10(1):1197 doi 10.1038/s41467-019-09186-x.
824 36. Subramanian A, Narayan R, Corsello SM, Peck DD, Natoli TE, Lu X*, et al.* A Next
825 Generation Connectivity Map: L1000 Platform and the First 1,000,000 Profiles. Cell
826 **2017**;171(6):1437-52 e17 doi 10.1016/j.cell.2017.10.049.
827 37. Corsello SM, Bittker JA, Liu Z, Gould J, McCarren P, Hirschman JE*, et al.* The Drug
828 Repurposing Hub: a next-generation drug library and information resource. Nat Med
829 **2017**;23(4):405-8 doi 10.1038/nm.4306.
830 38. Cotto KC, Wagner AH, Feng YY, Kiwala S, Coffman AC, Spies G*, et al.* DGIdb 3.0: a
831 redesign and expansion of the drug-gene interaction database. Nucleic Acids Res
832 **2018**;46(D1):D1068-D73 doi 10.1093/nar/gkx1143.
833 39. Cannon M, Stevenson J, Stahl K, Basu R, Coffman A, Kiwala S*, et al.* DGIdb 5.0:
834 rebuilding the drug-gene interaction database for precision medicine and drug discovery
835 platforms. Nucleic Acids Res **2024**;52(D1):D1227-D35 doi 10.1093/nar/gkad1040.
836 40. Griffith M, Griffith OL, Coffman AC, Weible JV, McMichael JF, Spies NC*, et al.* DGIdb:
837 mining the druggable genome. Nat Methods **2013**;10(12):1209-10 doi
838 10.1038/nmeth.2689.
839 41. Khatamian A, Paull EO, Califano A, Yu J. SJARACNe: a scalable software tool for gene
840 network reverse engineering from big data. Bioinformatics **2019**;35(12):2165-6 doi
841 10.1093/bioinformatics/bty907.
842 42. Northcott PA, Shih DJ, Peacock J, Garzia L, Morrissy AS, Zichner T*, et al.* Subgroup-
843 specific structural variation across 1,000 medulloblastoma genomes. Nature
844 **2012**;488(7409):49-56 doi 10.1038/nature11327.
845 43. de Bont JM, Kros JM, Passier MM, Reddingius RE, Sillevis Smitt PA, Luider TM*, et al.*
846 Differential expression and prognostic significance of SOX genes in pediatric
847 medulloblastoma and ependymoma identified by microarray analysis. Neuro Oncol
848 **2008**;10(5):648-60 doi 10.1215/15228517-2008-032.
849 44. Ashburner M, Ball CA, Blake JA, Botstein D, Butler H, Cherry JM*, et al.* Gene Ontology:
850 tool for the unification of biology. Nature Genetics **2000**;25(1):25-9 doi Doi 10.1038/75556.
851 45. Dong X, Ding L, Thrasher A, Wang X, Liu J, Pan Q*, et al.* NetBID2 provides comprehensive
852 hidden driver analysis. Nat Commun **2023**;14(1):2581 doi 10.1038/s41467-023-38335-6.
853 46. Cavalli FMG, Remke M, Rampasek L, Peacock J, Shih DJH, Luu B*, et al.* Intertumoral
854 Heterogeneity within Medulloblastoma Subgroups. Cancer Cell **2017**;31(6):737-54 e6 doi
855 10.1016/j.ccell.2017.05.005.
856 47. Archer TC, Ehrenberger T, Mundt F, Gold MP, Krug K, Mah CK*, et al.* Proteomics, Post-
857 translational Modifications, and Integrative Analyses Reveal Molecular Heterogeneity

858 within Medulloblastoma Subgroups. Cancer Cell **2018**;34(3):396-410 e8 doi
859 10.1016/j.ccell.2018.08.004.
860 48. Kort A, Durmus S, Sparidans RW, Wagenaar E, Beijnen JH, Schinkel AH. Brain and Testis
861 Accumulation of Regorafenib is Restricted by Breast Cancer Resistance Protein
862 (BCRP/ABCG2) and P-glycoprotein (P-GP/ABCB1). Pharm Res **2015**;32(7):2205-16 doi
863 10.1007/s11095-014-1609-7.
864 49. Jiang J, Zhang L, Chen H, Lei Y, Zhang T, Wang Y*, et al.* Regorafenib induces lethal
865 autophagy arrest by stabilizing PSAT1 in glioblastoma. Autophagy **2020**;16(1):106-22 doi
866 10.1080/15548627.2019.1598752.
867 50. Zeiner PS, Kinzig M, Dive I, Maurer GD, Filipski K, Harter PN*, et al.* Regorafenib CSF
868 Penetration, Efficacy, and MRI Patterns in Recurrent Malignant Glioma Patients. J Clin
869 Med **2019**;8(12) doi 10.3390/jcm8122031.
870 51. Freeman BB, 3rd, Yang L, Rankovic Z. Practical approaches to evaluating and optimizing
871 brain exposure in early drug discovery. Eur J Med Chem **2019**;182:111643 doi
872 10.1016/j.ejmech.2019.111643.
873 52. de Gooijer MC, Zhang P, Weijer R, Buil LCM, Beijnen JH, van Tellingen O. The impact of
874 P-glycoprotein and breast cancer resistance protein on the brain pharmacokinetics and
875 pharmacodynamics of a panel of MEK inhibitors. Int J Cancer **2018**;142(2):381-91 doi
876 10.1002/ijc.31052.
877 53. He C, Xu K, Zhu X, Dunphy PS, Gudenas B, Lin W*, et al.* Patient-derived models
878 recapitulate heterogeneity of molecular signatures and drug response in pediatric high-
879 grade glioma. Nat Commun **2021**;12(1):4089 doi 10.1038/s41467-021-24168-8.
880 54. Klaeger S, Heinzlmeir S, Wilhelm M, Polzer H, Vick B, Koenig PA*, et al.* The target
881 landscape of clinical kinase drugs. Science **2017**;358(6367) doi 10.1126/science.aan4368.
882 55. Kanehisa M, Goto S. KEGG: kyoto encyclopedia of genes and genomes. Nucleic Acids
883 Res **2000**;28(1):27-30 doi 10.1093/nar/28.1.27.
884 56. Ghandi M, Huang FW, Jane-Valbuena J, Kryukov GV, Lo CC, McDonald ER, 3rd*, et al.*
885 Next-generation characterization of the Cancer Cell Line Encyclopedia. Nature
886 **2019**;569(7757):503-8 doi 10.1038/s41586-019-1186-3.
887 57. Pilarczyk M, Fazel-Najafabadi M, Kouril M, Shamsaei B, Vasiliauskas J, Niu W*, et al.*
888 Connecting omics signatures and revealing biological mechanisms with iLINCS. Nat
889 Commun **2022**;13(1):4678 doi 10.1038/s41467-022-32205-3.
890 58. Smith KS, Xu K, Mercer KS, Boop F, Klimo P, DeCupyere M*, et al.* Patient-derived
891 orthotopic xenografts of pediatric brain tumors: a St. Jude resource. Acta Neuropathol
892 **2020**;140(2):209-25 doi 10.1007/s00401-020-02171-5.
893 59. McLeod C, Gout AM, Zhou X, Thrasher A, Rahbarinia D, Brady SW*, et al.* St. Jude Cloud:
894 A Pediatric Cancer Genomic Data-Sharing Ecosystem. Cancer Discov **2021**;11(5):1082-
895 99 doi 10.1158/2159-8290.CD-20-1230.
896 60. Padovani L, Horan G, Ajithkumar T. Radiotherapy Advances in Paediatric
897 Medulloblastoma Treatment. Clin Oncol (R Coll Radiol) **2019**;31(3):171-81 doi
898 10.1016/j.clon.2019.01.001.
899 61. Hill RM, Richardson S, Schwalbe EC, Hicks D, Lindsey JC, Crosier S*, et al.* Time, pattern,
900 and outcome of medulloblastoma relapse and their association with tumour biology at
901 diagnosis and therapy: a multicentre cohort study. The Lancet Child & Adolescent Health
902 **2020**;4(12):865-74 doi 10.1016/s2352-4642(20)30246-7.
903 62. Hovestadt V, Smith KS, Bihannic L, Filbin MG, Shaw ML, Baumgartner A*, et al.* Resolving
904 medulloblastoma cellular architecture by single-cell genomics. Nature **2019** doi
905 10.1038/s41586-019-1434-6.
906 63. Riemondy KA, Venkataraman S, Willard N, Nellan A, Sanford B, Griesinger AM*, et al.*
907 Neoplastic and immune single-cell transcriptomics define subgroup-specific intra-tumoral

908 heterogeneity of childhood medulloblastoma. Neuro Oncol **2022**;24(2):273-86 doi
909 10.1093/neuonc/noab135.
910 64. Hendrikse LD, Haldipur P, Saulnier O, Millman J, Sjoboen AH, Erickson AW*, et al.* Failure
911 of human rhombic lip differentiation underlies medulloblastoma formation. Nature
912 **2022**;609(7929):1021-8 doi 10.1038/s41586-022-05215-w.
913 65. Smith KS, Bihannic L, Gudenas BL, Haldipur P, Tao R, Gao Q*, et al.* Unified rhombic lip
914 origins of group 3 and group 4 medulloblastoma. Nature **2022**;609(7929):1012-20 doi
915 10.1038/s41586-022-05208-9.
916 66. Luo Z, Xia M, Shi W, Zhao C, Wang J, Xin D*, et al.* Human fetal cerebellar cell atlas informs
917 medulloblastoma origin and oncogenesis. bioRxiv **2022**:2022.08.17.504304 doi
918 10.1101/2022.08.17.504304.
919 67. Gibson P, Tong Y, Robinson G, Thompson MC, Currle DS, Eden C*, et al.* Subtypes of
920 medulloblastoma have distinct developmental origins. Nature **2010**;468(7327):1095-9 doi
921 10.1038/nature09587.
922 68. Erickson AW, Tan H, Hendrikse LD, Millman J, Thomson Z, Golser J*, et al.* Mapping the
923 developmental profile of ventricular zone-derived neurons in the human cerebellum. Proc
924 Natl Acad Sci U S A **2025**;122(17):e2415425122 doi 10.1073/pnas.2415425122.
925 69. Sepp M, Leiss K, Murat F, Okonechnikov K, Joshi P, Leushkin E*, et al.* Cellular
926 development and evolution of the mammalian cerebellum. Nature **2024** doi
927 10.1038/s41586-023-06884-x.
928 70. Aldinger KA, Thomson Z, Phelps IG, Haldipur P, Deng M, Timms AE*, et al.* Spatial and
929 cell type transcriptional landscape of human cerebellar development. Nat Neurosci
930 **2021**;24(8):1163-75 doi 10.1038/s41593-021-00872-y.
931 71. Lu S, Yang J, Yan L, Liu J, Wang JJ, Jain R*, et al.* Transcriptome size matters for single-
932 cell RNA-seq normalization and bulk deconvolution. Nat Commun **2025**;16(1):1246 doi
933 10.1038/s41467-025-56623-1.
934 72. Luo Z, Dong X, Yu J, Xia Y, Berry KP, Rao R*, et al.* Genomic and Transcriptomic Analyses
935 Reveals ZNF124 as a Critical Regulator in Highly Aggressive Medulloblastomas. Front
936 Cell Dev Biol **2021**;9:634056 doi 10.3389/fcell.2021.634056.
937 73. Pan Q, Ding L, Hladyshau S, Yao X, Zhou J, Yan L*, et al.* scMINER: a mutual information-
938 based framework for clustering and hidden driver inference from single-cell
939 transcriptomics data. Nat Commun **2025**;16(1):4305 doi 10.1038/s41467-025-59620-6.
940 74. Luo Z, Xin D, Liao Y, Berry K, Ogurek S, Zhang F*, et al.* Loss of phosphatase CTDNEP1
941 potentiates aggressive medulloblastoma by triggering MYC amplification and genomic
942 instability. Nat Commun **2023**;14(1):762 doi 10.1038/s41467-023-36400-8.
943 75. Bae J, Accardi F, Hideshima T, Tai YT, Prabhala R, Shambley A*, et al.* Targeting
944 LAG3/GAL-3 to overcome immunosuppression and enhance anti-tumor immune
945 responses in multiple myeloma. Leukemia **2022**;36(1):138-54 doi 10.1038/s41375-021-
946 01301-6.
947 76. Blum JS, Wearsch PA, Cresswell P. Pathways of antigen processing. Annu Rev Immunol
948 **2013**;31:443-73 doi 10.1146/annurev-immunol-032712-095910.
949 77. Chen YH, Lee YM, Ou DL, Hsu CL, Hsu C, Chen CN*, et al.* Regorafenib enhances M1/M2
950 macrophage polarization by inhibiting the secretion of plasminogen activator inhibitor-1 in
951 head and neck squamous cell carcinoma. Life Sci **2024**;358:123147 doi
952 10.1016/j.lfs.2024.123147.
953 78. Allen F, Bobanga ID, Rauhe P, Barkauskas D, Teich N, Tong C*, et al.* CCL3 augments
954 tumor rejection and enhances CD8(+) T cell infiltration through NK and CD103(+) dendritic
955 cell recruitment via IFNgamma. Oncoimmunology **2018**;7(3):e1393598 doi
956 10.1080/2162402X.2017.1393598.

79. Kang TG, Park HJ, Moon J, Lee JH, Ha SJ. Enriching CCL3 in the Tumor Microenvironment Facilitates T cell Responses and Improves the Efficacy of Anti-PD-1 Therapy. Immune Netw **2021**;21(3):e23 doi 10.4110/in.2021.21.e23.
80. Eberlein J, Davenport B, Nguyen TT, Victorino F, Jhun K, van der Heide V*, et al.* Chemokine Signatures of Pathogen-Specific T Cells I: Effector T Cells. J Immunol **2020**;205(8):2169-87 doi 10.4049/jimmunol.2000253.
81. Wang BL, Wang Y, Sun XF, Deng GL, Huang W, Wu XX*, et al.* CXCR6 is required for antitumor efficacy of intratumoral CD8 T cell. Journal for Immunotherapy of Cancer **2021**;9(8) doi ARTN e00310010.1136/jitc-2021-003100.
82. Di Pilato M, Kfuri-Rubens R, Pruessmann JN, Ozga AJ, Messemaker M, Cadilha BL*, et al.* CXCR6 positions cytotoxic T cells to receive critical survival signals in the tumor microenvironment. Cell **2021**;184(17):4512-+ doi ARTN e22
10.1016/j.cell.2021.07.015.
83. Muthuswamy R, McGray AJR, Battaglia S, He WJ, Miliotto A, Eppolito C*, et al.* CXCR6 by increasing retention of memory CD8
T cells in the ovarian tumor microenvironment promotes immunosurveillance and control of ovarian cancer. Journal for Immunotherapy of Cancer **2021**;9(10) doi ARTN e003329
10.1136/jitc-2021-003329.
84. Seo YD, Jiang XY, Sullivan KM, Jalikis FG, Smythe KS, Abbasi A*, et al.* Mobilization of CD8⁺ T Cells via CXCR4 Blockade Facilitates PD-1 Checkpoint Therapy in Human Pancreatic Cancer. Clinical Cancer Research **2019**;25(13):3934-45 doi 10.1158/1078-0432.Ccr-19-0081.
85. Liu SY, Zhang W, Liu K, Wang YC. CD160 expression on CD8
T cells is associated with active effector responses but limited activation potential in pancreatic cancer. Cancer Immunol Immun **2020**;69(5):789-97 doi 10.1007/s00262-020-02500-3.
86. Duhen T, Duhen R, Montler R, Moses J, Moudgil T, de Miranda NF*, et al.* Co-expression of CD39 and CD103 identifies tumor-reactive CD8 T cells in human solid tumors. Nature Communications **2018**;9 doi ARTN 2724
10.1038/s41467-018-05072-0.
87. Lamichhane R, Schneider M, de la Harpe SM, Harrop TWR, Hannaway RF, Dearden PK*, et al.* TCR- or Cytokine-Activated CD8(+) Mucosal-Associated Invariant T Cells Are Rapid Polyfunctional Effectors That Can Coordinate Immune Responses. Cell Rep **2019**;28(12):3061-76 e5 doi 10.1016/j.celrep.2019.08.054.
88. Jin SQ, Guerrero-Juarez CF, Zhang LH, Chang I, Ramos R, Kuan CH*, et al.* Inference and analysis of cell-cell communication using CellChat. Nature Communications **2021**;12(1) doi ARTN 1088
10.1038/s41467-021-21246-9.
89. Huang L, Garrett Injac S, Cui K, Braun F, Lin Q, Du Y*, et al.* Systems biology-based drug repositioning identifies digoxin as a potential therapy for groups 3 and 4 medulloblastoma. Sci Transl Med **2018**;10(464) doi 10.1126/scitranslmed.aat0150.
90. Hovestadt V, Ayrault O, Swartling FJ, Robinson GW, Pfister SM, Northcott PA. Medulloblastomics revisited: biological and clinical insights from thousands of patients. Nat Rev Cancer **2020**;20(1):42-56 doi 10.1038/s41568-019-0223-8.
91. Visvanathan A, Saulnier O, Chen C, Haldipur P, Orisme W, Delaidelli A*, et al.* Early rhombic lip Protogenin(+ve) stem cells in a human-specific neurovascular niche initiate and maintain group 3 medulloblastoma. Cell **2024**;187(17):4733-50 e26 doi 10.1016/j.cell.2024.06.011.
92. Jessa S, Blanchet-Cohen A, Krug B, Vladoiu M, Coutelier M, Faury D*, et al.* Stalled developmental programs at the root of pediatric brain tumors. Nat Genet **2019**;51(12):1702-13 doi 10.1038/s41588-019-0531-7.

1007 93. Xie X, Zhang O, Yeo MJR, Lee C, Tao R, Harry SA*, et al.* Converging mechanism of
1008 UM171 and KBTBD4 neomorphic cancer mutations. Nature **2025**;639(8053):241-9 doi
1009 10.1038/s41586-024-08533-3.
1010 94. Lombardi G, De Salvo GL, Brandes AA, Eoli M, Rudà R, Faedi M*, et al.* Regorafenib
1011 compared with lomustine in patients with relapsed glioblastoma (REGOMA): a multicentre,
1012 open-label, randomised, controlled, phase 2 trial. The Lancet Oncology **2019**;20(1):110-9
1013 doi 10.1016/s1470-2045(18)30675-2.
1014 95. Weiss BD, Wolters PL, Plotkin SR, Widemann BC, Tonsgard JH, Blakeley J*, et al.* NF106:
1015 A Neurofibromatosis Clinical Trials Consortium Phase II Trial of the MEK Inhibitor
1016 Mirdametinib (PD-0325901) in Adolescents and Adults With NF1-Related Plexiform
1017 Neurofibromas. J Clin Oncol **2021**:JCO2002220 doi 10.1200/JCO.20.02220.
1018 96. Banerjee A, Jakacki R, Onar-Thomas A, Wu SJ, Nicolaides T, Turner D*, et al.* A phase I
1019 study of AZD6244 in children with recurrent or refractory low-grade gliomas: A Pediatric
1020 Brain Tumor Consortium report. Journal of Clinical Oncology **2014**;32(15) doi DOI
1021 10.1200/jco.2014.32.15_suppl.10065.
1022 97. Andrew N, Sterin A, Solas C, Le Deley MC, Probst A, Aerts I*, et al.* Phase 1 Study of
1023 Fluvastatin-Celecoxib Combination in Children with Relapsing/Refractory Optico-
1024 Chiasmatic Low-Grade Glioma or High-Grade Gliomas (Fluvabrex): Final Results. Neuro-
1025 Oncology **2020**;22:305-6.
1026 98. Corcoran RB, Atreya CE, Falchook GS, Kwak EL, Ryan DP, Bendell JC*, et al.* Combined
1027 BRAF and MEK Inhibition With Dabrafenib and Trametinib in BRAF V600-Mutant
1028 Colorectal Cancer. J Clin Oncol **2015**;33(34):4023-31 doi 10.1200/JCO.2015.63.2471.
1029 99. Wu CS, Wu SY, Chen HC, Chu CA, Tang HH, Liu HS*, et al.* Curcumin functions as a MEK
1030 inhibitor to induce a synthetic lethal effect on KRAS mutant colorectal cancer cells
1031 receiving targeted drug regorafenib. J Nutr Biochem **2019**;74:108227 doi
1032 10.1016/j.jnutbio.2019.108227.
1033 100. Lau DK, Luk IY, Jenkins LJ, Martin A, Williams DS, Schoffer KL*, et al.* Rapid Resistance
1034 of FGFR-driven Gastric Cancers to Regorafenib and Targeted FGFR Inhibitors can be
1035 Overcome by Parallel Inhibition of MEK. Mol Cancer Ther **2021**;20(4):704-15 doi
1036 10.1158/1535-7163.MCT-20-0836.
1037 101. Adamopoulos C, Ahmed TA, Tucker MR, Ung PMU, Xiao M, Karoulia Z*, et al.* Exploiting
1038 Allosteric Properties of RAF and MEK Inhibitors to Target Therapy-Resistant Tumors
1039 Driven by Oncogenic BRAF Signaling. Cancer Discov **2021** doi 10.1158/2159-8290.CD-
1040 20-1351.
1041 102. MacDonald TJ, Brown KM, LaFleur B, Peterson K, Lawlor C, Chen Y*, et al.* Expression
1042 profiling of medulloblastoma: PDGFRA and the RAS/MAPK pathway as therapeutic
1043 targets for metastatic disease Nature Genetics **2003**;35(3):287- doi DOI 10.1038/ng1103-
1044 287a.
1045 103. Abeysundara N, Rasnitsyn A, Fong V, Bahcheli A, Van Ommeren R, Juraschka K*, et al.*
1046 Metastatic medulloblastoma remodels the local leptomeningeal microenvironment to
1047 promote further metastatic colonization and growth. Nat Cell Biol **2025** doi
1048 10.1038/s41556-025-01660-7.
1049 104. da Cunha Jaeger M, Ghisleni EC, Cardoso PS, Siniglaglia M, Falcon T, Brunetto AT*, et*
1050 *al.* HDAC and MAPK/ERK Inhibitors Cooperate To Reduce Viability and Stemness in
1051 Medulloblastoma. J Mol Neurosci **2020**;70(6):981-92 doi 10.1007/s12031-020-01505-y.
1052 105. Bakhshinyan D, Adile AA, Liu J, Gwynne WD, Suk Y, Custers S*, et al.* Temporal profiling
1053 of therapy resistance in human medulloblastoma identifies novel targetable drivers of
1054 recurrence. Sci Adv **2021**;7(50):eabi5568 doi 10.1126/sciadv.abi5568.
1055 106. Li S, Chen J, Fan Y, Wang C, Wang C, Zheng X*, et al.* Liposomal Honokiol induces ROS-
1056 mediated apoptosis via regulation of ERK/p38-MAPK signaling and autophagic inhibition
1057 in human medulloblastoma. 2022 Feb 21. Report nr 2059-3635 (Electronic)

2059-3635 (Linking). 49 p.
107. Ebert PJR, Cheung J, Yang Y, McNamara E, Hong R, Moskalenko M*, et al.* MAP Kinase Inhibition Promotes T Cell and Anti-tumor Activity in Combination with PD-L1 Checkpoint Blockade. Immunity **2016**;44(3):609-21 doi 10.1016/j.immuni.2016.01.024.
108. Liu J, Tao H, Yuan T, Li J, Li J, Liang H*, et al.* Immunomodulatory effects of regorafenib: Enhancing the efficacy of anti-PD-1/PD-L1 therapy. Front Immunol **2022**;13:992611 doi 10.3389/fimmu.2022.992611.
109. Ou DL, Chen CW, Hsu CL, Chung CH, Feng ZR, Lee BS*, et al.* Regorafenib enhances antitumor immunity via inhibition of p38 kinase/Creb1/Klf4 axis in tumor-associated macrophages. J Immunother Cancer **2021**;9(3) doi 10.1136/jitc-2020-001657.
110. Zheng S, Wang W, Aldahdooh J, Malyutina A, Shadbahr T, Tanoli Z*, et al.* SynergyFinder Plus: Toward Better Interpretation and Annotation of Drug Combination Screening Datasets. Genomics Proteomics Bioinformatics **2022**;20(3):587-96 doi 10.1016/j.gpb.2022.01.004.
111. Hao Y, Stuart T, Kowalski MH, Choudhary S, Hoffman P, Hartman A*, et al.* Dictionary learning for integrative, multimodal and scalable single-cell analysis. Nat Biotechnol **2024**;42(2):293-304 doi 10.1038/s41587-023-01767-y.
112. Korsunsky I, Millard N, Fan J, Slowikowski K, Zhang F, Wei K*, et al.* Fast, sensitive and accurate integration of single-cell data with Harmony. Nat Methods **2019**;16(12):1289-96 doi 10.1038/s41592-019-0619-0.
113. Marsh S. scCustomize: Custom Visualizations & Functions for Streamlined Analyses of Single Cell Sequencing. **2025**.
114. Cao J, Spielmann M, Qiu X, Huang X, Ibrahim DM, Hill AJ*, et al.* The single-cell transcriptional landscape of mammalian organogenesis. Nature **2019**;566(7745):496-502 doi 10.1038/s41586-019-0969-x.
115. Street K, Risso D, Fletcher RB, Das D, Ngai J, Yosef N*, et al.* Slingshot: cell lineage and pseudotime inference for single-cell transcriptomics. BMC Genomics **2018**;19(1):477 doi 10.1186/s12864-018-4772-0.
116. Kassambara; I, Kosinski; M, Biecek P. survminer: Drawing Survival Curves using 'ggplot2'}. **2025**.
117. Therneau TM. A Package for Survival Analysis in R. **2024**.
118. Korotkevich G, Sukhov V, Budin N, Shpak B, Artyomov MN, Sergushichev A. **2021** doi 10.1101/060012.
119. Gu Z, Eils R, Schlesner M. Complex heatmaps reveal patterns and correlations in multidimensional genomic data. Bioinformatics **2016**;32(18):2847-9 doi 10.1093/bioinformatics/btw313.
120. Ritz C, Baty F, Streibig JC, Gerhard D. Dose-Response Analysis Using R. PLoS One **2015**;10(12):e0146021 doi 10.1371/journal.pone.0146021.
121. Margolin AA, Nemenman I, Basso K, Wiggins C, Stolovitzky G, Dalla Favera R*, et al.* ARACNE: an algorithm for the reconstruction of gene regulatory networks in a mammalian cellular context. BMC Bioinformatics **2006**;7 Suppl 1:S7 doi 10.1186/1471-2105-7-S1-S7.
122. Scrucca L. GA: A Package for Genetic Algorithms in R. Journal of Statistical Software **2013**;53(4):1–37 doi 10.18637/jss.v053.i04.
123. Jonchere B, Williams J, Zindy F, Liu J, Robinson S, Farmer DM*, et al.* Combination of Ribociclib with BET-Bromodomain and PI3K/mTOR Inhibitors for Medulloblastoma Treatment In Vitro and In Vivo. Mol Cancer Ther **2023**;22(1):37-51 doi 10.1158/1535-7163.MCT-21-0896.
124. Milde T, Lodrini M, Savelyeva L, Korshunov A, Kool M, Brueckner LM*, et al.* HD-MB03 is a novel Group 3 medulloblastoma model demonstrating sensitivity to histone deacetylase inhibitor treatment. J Neurooncol **2012**;110(3):335-48 doi 10.1007/s11060-012-0978-1.

125. Bandopadhayay P, Bergthold G, Nguyen B, Schubert S, Gholamin S, Tang Y*, et al.* BET bromodomain inhibition of MYC-amplified medulloblastoma. Clin Cancer Res **2014**;20(4):912-25 doi 10.1158/1078-0432.CCR-13-2281.
126. Kawauchi D, Robinson G, Uziel T, Gibson P, Rehg J, Gao C*, et al.* A mouse model of the most aggressive subgroup of human medulloblastoma. Cancer Cell **2012**;21(2):168-80 doi 10.1016/j.ccr.2011.12.023.
127. Xie J, Kuriakose T, Bianski B, Twarog N, Savage E, Xu K*, et al.* ATM inhibition enhances the efficacy of radiation across distinct molecular subgroups of pediatric high-grade glioma. Neuro Oncol **2023**;25(10):1828-41 doi 10.1093/neuonc/noad064.
128. Qiu X, Mao Q, Tang Y, Wang L, Chawla R, Pliner HA*, et al.* Reversed graph embedding resolves complex single-cell trajectories. Nat Methods **2017**;14(10):979-82 doi 10.1038/nmeth.4402.

1120 **Figure legends**

1121

1122 **Figure 1. SINBA leverages gene activity data and knowledge-based drug databases to**
1123 **predict and guide screening of synergistic drug pairs for high-risk medulloblastoma**

1124 **A,** Overview of the SINBA workflow for identifying synergistic drug combinations in
1125 medulloblastoma. Preparatory steps include using SJARACNe to generate a disease-specific
1126 gene interaction network and NetBID2 to identify subtype-specific driver genes. SINBA then
1127 selects drugs for single-agent screening before predicting synergistic drug pairs for combination
1128 testing. Finally, combination screening and synergy analysis identify promising drug pairs for
1129 validation. **B,** Breakdown of the Brain Penetrant Database (BPdb), a manually curated repository
1130 of potential and clinically validated blood-brain barrier penetrating (BBB+) drugs. SINBA
1131 integrates the BPdb with five additional drug-gene interaction databases for comprehensive target
1132 annotation. **C,** An optimized driver pair matrix based on SINBA's predictions of synergy *in silico*.
1133 Seed drivers (columns) and partner drivers (rows) are listed with their respective drugs. Delta Z-
1134 scores indicate the predicted synergy of each driver pair. **D,** Synergy analysis of the results of 10-
1135 dose combination screening. Synergy is expressed as a Zero Interaction Potency (ZIP) score.
1136 Data are represented as the mean ± SEM.

1137 See also Supplementary Figures S1, S2 and S3.

1138

1139

1140 **Figure 2. Synergistic and on-target effects of MEK inhibitor and regorafenib combination**
1141 **in human G3 MB models**

1142 **A,** Left panel shows the combined activities of BRAF and MAPK11 in five human MB cell lines.
1143 Right panel shows those cell lines' drug sensitivity scores for trametinib (TRA) plus regorafenib
1144 (REG). **B,** Ranked ZIP scores for two regorafenib + MEK inhibitor (trametinib or mirdametinib)
1145 combinations in human MB cell lines. Data are represented as mean ± SEM.

1146 **C,** Cell growth inhibition contour plots and synergy landscapes for drug-dose combinations of
1147 regorafenib and trametinib (left) and regorafenib and mirdametinib (right) in D341 cells. **D,** Cell
1148 growth inhibition contour plots and synergy landscapes for drug-dose combinations of regorafenib
1149 and trametinib (left) and regorafenib and mirdametinib (right) in MB002 cells. E, Western blot
1150 analysis comparing total and phosphorylated MEK, ERK, p38, and BRAF following single agent
1151 and combination treatment with regorafenib + trametinib (left) or regorafenib + mirdametinib (right)
1152 at indicated time points.
1153 See also Supplementary Figure S4.
1154
1155
1156 **Figure 3. MEK inhibitor and regorafenib combination has synergistic anti-tumor efficacy *in***
1157 ***vivo* with G3 cell line model**
1158 **A,** Schematic of experimental design for drug administration and imaging in CD-1 nude mice
1159 implanted intracranially with D341, PDX5950, or DAOY tumor cells (created with BioRender.com).
1160 Mice were randomized to receive vehicle (p.o.), mirdametinib (5 mg/kg or 0.5 mg/kg, p.o.),
1161 regorafenib (10 mg/kg, p.o.), or the combination, starting one week post-implantation and
1162 continuing three times per week for six weeks. IVIS or MRI imaging was performed weekly starting
1163 one week after surgery. **B,** Representative *in vivo* bioluminescent images of mice bearing
1164 orthotopic D341 tumors from weeks 1 to 5 post-implantation. **C,** Quantification of bioluminescence
1165 signal (BLI) at week 2 post-treatment in the D341 model, showing significant tumor growth
1166 reduction in the combination group. Data are presented as mean ± SEM. **D,** Kaplan–Meier survival
1167 curves for mice implanted with D341 cells and treated as described in (B). Group sizes (n) are
1168 indicated in the risk table; log-rank test results: *P < 0.05, **P < 0.01, ***P < 0.001; ns, not
1169 significant. **E,** Left: Representative IHC staining for cleaved caspase-3 in D341 tumors. Right:
1170 Quantification of cleaved caspase-3-positive cells. Data are presented as mean ± SEM. *P < 0.05;
1171 **P < 0.01.

1172 See also Supplementary Figures S5 and S6.

1173

1174

1175 **Figure 4. MEK inhibitor and regorafenib combination has synergistic anti-tumor efficacy *in***

1176 ***vivo* with patient derived orthotopic xenograft model**

1177 **A,** Left panel shows the combined activities of BRAF and MAPK11 in normal cerebellum and

1178 human G3 MB PDOX models. Right panel shows their drug sensitivity scores for trametinib (TRA)

1179 plus regorafenib (REG). **B,** Top: Heatmap of PDX5950 cell viability with regorafenib and MEK

1180 inhibitor combinations. Bottom: Dose–response curves for regorafenib in combination with fixed

1181 concentrations of trametinib or mirdametinib. **C,** Kaplan–Meier survival curves for mice implanted

1182 with PDX5950 and treated as described in Figure 3A. Group sizes (n) are indicated in the risk

1183 table; log-rank test results: ***P < 0.001; ns, not significant. **D,** MRI-quantified tumor volumes at

1184 week 4 post-treatment. *P < 0.05. **E,** Left: Representative IHC staining for cleaved caspase-3 in

1185 PDX5950 tumors. Right: Quantification of cleaved caspase-3-positive cells. Data are represented

1186 as mean ± SEM. *P < 0.05; **P < 0.01.

1187

1188

1189 **Figure 5. MEK inhibitor and regorafenib combination therapy targets on UBC_GCP**

1190 **common progenitor and UBC progenitor like tumor cells**

1191 **A,** Re-annotation of the normal glutamatergic neuronal lineage, projected onto a UMAP

1192 embedding using scRNA-seq data from Lu et al. **B,** Expression patterns of key marker genes

1193 defining glutamatergic lineage cell states. **C,** Cell state annotation of Medulloblastoma tumor cells

1194 (patient scRNA-seq data, GSE156053*; Riemondy et al.*) using the normal developmental

1195 reference from A. Visualization restricted to tumor cells. **D,** Proportional distribution of tumor cell

1196 states across medulloblastoma patient subgroups. **E,** Feature and violin plots showing driver

1197 combination activities and predicted drug sensitivity scores within tumor populations. **F,** UMAP

1198 visualization of orthotopically implanted D341 tumor cells (in CD-1 mice) from treated mice,
1199 annotated with cell states using the normal developmental reference. **G,** Proportional distribution
1200 of tumor cell states across treatment groups. **H-J,** Single-cell feature plots (**H**) and violin plots (**I**,
1201 **J**) of driver activities and drug sensitivity scores across treatment arms (**I**) and predicted cell states
1202 (**J**).
1203 See also Supplementary Figures S7 and S8.
1204
1205
1206 **Figure 6. The combination of MEK inhibitor and regorafenib is effective in CTD, an**
1207 **immunocompetent syngenetic mouse model of G3 MB**
1208 **A-B,** Top: Heatmap of the CTD syngenetic mouse tumor cell viability treated with regorafenib and
1209 MEK inhibitor combinations. Bottom: Dose-response curves of regorafenib with fixed
1210 concentrations of trametinib (left) or mirdametinib (right). **C,** Western blot analysis of total and
1211 phosphorylated Mek, Erk, p38, and Braf in CTD cells following treatment at indicated time points.
1212 **D,** Schematic of experimental design for drug administration and MRI imaging in C57BL/6J mice
1213 (created with BioRender.com). Seven days after intracranial implantation of CTD cells, mice were
1214 randomized into four treatment groups and treated three times per week for six weeks with vehicle
1215 (p.o.), mirdametinib (0.5 mg/kg p.o.), regorafenib (10 mg/kg p.o.), or the combination. **E,** MRI-
1216 measured tumor volumes across treatment groups. Unpaired two-sided t tests were used; **P <
1217 0.01. **F,** Kaplan–Meier survival curves for mice treated as described in (D). Group sizes (n) are
1218 indicated in the risk table; log-rank test results: *P < 0.05, **P < 0.01, ***P < 0.001, ns, not
1219 significant.
1220
1221
1222 **Figure 7. MEK inhibition combined with regorafenib remodels tumor cell states and the**
1223 **tumor microenvironment in the CTD syngenetic mouse model**

1224 **A,** Schematic of experimental design for generating scRNA-seq data from the CTD syngeneic
1225 model preclinical study (created with BioRender.com). **B,** UMAP visualization of the cells from
1226 the CTD model treated with monotherapy or combination therapy *in vivo*, with cells colored by
1227 their annotated cell types. **C,** UMAP plot of tumor cell states in the four treatment groups. **D,**
1228 Proportional distribution of tumor cell states across treatment groups. **E,** Volcano plot of
1229 differentially expressed genes in tumor cells from the MIR_REG combination group versus other
1230 treatments. **F,** Functional enrichment of top upregulated genes (avg_log2FC > 1, adjusted p <
1231 0.05) in tumor cells from the MIR_REG combination group. **G,** Antigen presentation module
1232 scores in tumor cells across treatment groups; two-sided t tests were used to compare
1233 combination treatment with other groups. *P < 0.05, **P < 1.0e-10, ***P < 1.0e-20. **H,**
1234 Proportional distribution of Cd45+ immune cells across treatment groups. **I,** Log2 fold-change in
1235 abundance of immune cell populations for each treatment group relative to the vehicle control.
1236 **J,** Ratio of T effector (Teffector) to T regulatory (Treg) cells across treatment groups. **K,**
1237 CellChat-inferred ligand–receptor communication probabilities from monocytes to Teffector and
1238 Treg cells.
1239 See also Supplementary Figures S9 and S10.

1240 **MEHTODS**

1241

1242 **Chemicals**

1243 Regorafenib monohydrate (HY-10331A), Trametinib (HY-10999), and Mirdametinib (PD0325901,
1244 HY-10254) were obtained from MedChemExpress (MCE). For in vitro studies, each compound
1245 was dissolved in dimethyl sulfoxide (DMSO; FisherScientific, BP231-100) to a final stock
1246 concentration of 10 mM. For in vivo preclinical studies, the compounds were formulated as follows.
1247 1. Regorafenib: The free base equivalent of regorafenib was calculated using a correction factor
1248 of 1.0373 for its monohydrate form. The drug was first dissolved in an 80% non-aqueous vehicle
1249 consisting of propylene glycol (PG, 42.5%), polyethylene glycol 400 (PEG400, 42.5%), and
1250 Pluronic F68 (15%) (v/v/v) by heating to 60 °C with agitation and vortexing. The solution was then
1251 brought to final volume with ultra-pure water at room temperature, yielding a clear formulation for
1252 oral gavage at a concentration of 3 mg/mL, administered at 10 mL/kg. 2. Trametinib: A 3 mg/mL
1253 stock solution was prepared in DMSO. For oral administration, the stock was diluted to 1% DMSO
1254 in a vehicle consisting of 10% Cremophor RH40, 10% PEG400, and 80% ultra-pure water,
1255 resulting in a final dose concentration of 0.03 mg/mL, delivered at 10 mL/kg. 3. Mirdametinib: The
1256 compound was formulated at 2.5 mg/mL in an aqueous suspension containing 1%
1257 methylcellulose and 1% Tween 80. The formulation was prepared using sonication to ensure
1258 uniform dispersion and administered by oral gavage at a dose volume of 10 mL/kg.

1259

1260 **The SINBA algorithm to identify synergistic drug pairs for G3 MB**

1261 The SINBA package is available on GitHub with a detailed tutorial
1262 (https://github.com/jyyulab/SINBA). Below, we outline the steps used to identify synergistic
1263 therapeutics for Group 3 medulloblastoma (G3 MB) using SINBA.

1264

1265 1. Construction of medulloblastoma-specific gene-gene interaction network

1266 To reconstruct medulloblastoma-specific interactomes (MBi), we applied the SJARACNe
1267 algorithm(41,121) to a curated microarray dataset, DKFZ_SJ, comprising 407 medulloblastoma
1268 patient samples. Using Gene Ontology classifications, we compiled a list of 11,239 transcription
1269 factor (TF) genes and signaling molecules to serve as hub genes in the MBi. Separate
1270 transcription factor (TF) and signaling molecule (SIG) networks were generated using SJARACNe.
1271 In this final network, drivers were linked to their downstream targets through edges based on
1272 gene–gene mutual information derived from their expression patterns. The reconstructed MBi
1273 consisted of 38,621 probe nodes and 1,567,381 interactions, representing 12,495 hub probes
1274 (corresponding to 7,155 genes) and their downstream target probes.
1275
1276 2. Identification of G3-Specific Drivers
1277 Hub gene activities for each sample in the DKFZ_SJ dataset (407 MB patients, 4 normal
1278 cerebellum) were inferred using NetBID2 package(45) function **cal.Activity** (es.method =
1279 "weightedmean"), which integrates gene expression profiles with the MBi. G3-specific drivers
1280 were selected based on the following criteria, resulting in 75 candidates:
1281 - Adjusted p-value for G3 vs. other subgroups < 1e-5, with Z-score > 0.
1282 - Adjusted p-value for G3 vs. normal cerebellum < 1e-3, with Z-score > 0.
1283 - Regulon size between 50 and 500.
1284
1285 3. Refinement of G3-Specific Drivers
1286 To refine the list, we used SINBA's built-in Brain Penetrant database (BPdb) to filter for druggable
1287 drivers, yielding 45 seed drivers targeted by 69 compounds. TF and SIG networks were merged
1288 using the SINBA function **get.combined.network** to prepare for activity calculations and driver-
1289 pair predictions. Driver pairs were generated either manually or by unbiasedly combining seed
1290 drivers with all druggable hub genes using the **combineNet2Target_list** function.

1291 Following seed drug library screening, 20 drugs (targeting 20 seed drivers) with EC20 < 10 μM or
1292 the solo agent targeting on the interesting seed drivers.
1293
1294 4. Prediction of Driver Pairs and Drug Pairs
1295 Driver-pair predictions were performed by combining the TF and SIG networks and pairing the 20
1296 seed drivers with all druggable MBi hub genes using the **combineNet2Target_list** function.
1297 Activities for single drivers and driver pairs were calculated using **cal.SINBA.Activity**. Driver pairs
1298 were ranked using **get.SINBA.DE.2G**, which computes statistical values comparing G3 with other
1299 subtypes and normalizes p-values into Z scores (Z.pair). Z scores for seed (Z.seed) and partner
1300 drivers (Z.partner) were calculated similarly. The delta.Z score was defined as:
1301

1302 $$\mathrm{delta.Z} = \frac{\mathrm{Z.pair(G3.vs.other\ subtype)}}{\sqrt{2}}$$

1303 $$- \frac{\mathrm{Z.seed(G3.vs.other\ subtype)} + \mathrm{Z.partner(G3.vs.other\ subtype)}}{2}$$

1304
1305 A genetic algorithm(122) (implemented in the function **find_max_sum_submatrix**) was then
1306 employed to optimize the maximum sum of delta.Z scores (*in silicon* synergistic scores) for G3
1307 vs. other subtypes. The final matrix layout consisted of 20 seed drivers × 16 partner drivers. BPdb
1308 was then used to convert driver pairs into drug pairs.
1309
1310 **SINBA-guided drug combination screening**
1311 1. Single-Drug Dose–Response Testing
1312 A total of 90 compounds (69 predicted seed drugs and 21 partner drugs) identified by the SINBA
1313 algorithm were screened. Compounds were tested in 10-point dose-response curves (10 μM to
1314 0.47 nM, 1:3 serial dilution) against the HDMB03 cell line. Cell culture conditions, tumor

1315 dissociation protocols, and density optimization followed established methods(123). HDMB03
1316 cells were seeded in 384-well plates. After 24 hours, compounds were pin-transferred (Biomek
1317 FX Workstation; Beckman Coulter) with negative (0.08% DMSO) and positive control (1.6 μM
1318 staurosporine; MedChemExpress, HY-15141). Cell viability was assessed 7 days post-treatment
1319 using CellTiter-Glo® (Promega, G7572). Dose-response curves were fitted using the drc
1320 package(120) with four-parameter log-logistic function to estimate EC_{20}, EC_{50} values, which
1321 defined low- and high-dose conditions (with fixed defaults of 1 μM and 6 μM, respectively, for
1322 drugs lacking EC_{20} or EC_{50} values).The four-parameter log-logistic function is given by the
1323 expression:
1324

1325 $$f(x) = c + \frac{d - c}{1 + \exp\left(b(\log(x) - \log(e))\right)}$$

1326
1327
1328 2. Two-dose combination testing
1329 To prioritize the drug pairs testing for synergy, 320 SINBA-predicted drug pairs were tested in
1330 384-well plates (64 wells reserved for controls). Each pair included four conditions: drug1 low
1331 dose+ drug2 high dose; drug1 high dose + drug2 high dose; drug1 low dose + drug2 low dose;
1332 drug1 high dose + drug2 low dose. 7 days after treatment, viability was measured (CellTiter-Glo®,
1333 Promega) and normalized to controls. Combination effects were quantified as:
1334

1335 $$Combo_{effect} = Ecombo - \frac{Edrug1 + Edrug2}{2}$$

1336
1337 3. 10-dose combination screening
1338 32 prioritized pairs were tested in full dose-response matrices (10×10 concentrations, 10 mmol/L
1339 to 0.14 nmol/L). Drugs were added simultaneously, and viability was assessed after 7 days.

1340 Synergy score were calculated using the synergyFinder package(110) with zero interaction
1341 potency (ZIP) model(32).
1342
1343 **Medulloblastoma Patient SINBA Shiny App**
1344 We developed a medulloblastoma-specific SINBA Shiny app to provide a comprehensive
1345 resource for exploring MB patient data(https://yulab-stjude.shinyapps.io/SINBA_MB). The app
1346 includes pre-built MBi networks, curated six drug-gene interaction databases, driver and driver-
1347 pair activity profiles, gene expression profiles, and patient clinical outcomes. Users can flexibly
1348 select druggable drivers using six integrated drug-gene interaction databases and explore
1349 potential synergistic driver pairs. This tool is designed to support hypothesis generation and
1350 facilitate the identification of therapeutic targets in medulloblastoma research.
1351
1352 **Cell culture and transfection**
1353 G3 MB human cell line HDMB03 and MB002 were generously provided by Dr. Till Milde and Dr.
1354 Jae-Youn Cho, respectively(124,125). PDX model SJMBG3-12-5950 (PDX5950) was utilized as
1355 described in the published work(58). Human SHH subgroup DAOY cell line was purchased from
1356 American Tissue Culture Collection (ATCC, HTB-186). Human G3 cell lines D341, D283, D425
1357 and mouse model CTD(74) were generously provided by Dr. Richard Q. Lu. Human cell lines and
1358 PDX model were cultured as neurospheres in supplemented neurobasal medium per established
1359 protocol(126). All lines underwent quarterly mycoplasma testing (MycoAlert™, Lonza) and
1360 maintained <10 passages post-thaw.
1361
1362 To generate the luciferase-expressing D341 cell line, cells were infected with a lentiviral vector
1363 (CL20SF2-Luc2aYFP) containing the firefly luciferase and yellow fluorescent protein (YFP) genes
1364 at a multiplicity of infection (MOI) of 20. Following infection, cells were sorted based on YFP
1365 fluorescence to select for positively transduced cells.

1366

1367 The mouse model CTD was cultured using previously published methods. Briefly, CTD cells were
1368 grown in DMEM/F-12 medium supplemented with HEPES buffer, sodium pyruvate, non-essential
1369 amino acids, GlutaMax (Thermofisher Cat# 35050061) and B-27 supplement (Thermofisher Cat#
1370 17504044) at 37°C and 5% CO2. A total of $1x10^6$ CTD cells were infected with 1µl of virus (titer
1371 $4x10^{10}$) for 48h. Then YFP+ cells were sorted by fluorescent-activated cell sorting (FACS).

1372

1373 **Drug signature score calculation in medulloblastoma tumors**

1374 Gene signatures induced by regorafenib and trametinib treatment in the central nervous system
1375 were obtained from the iLINCS database (https://www.ilincs.org/ilincs/;regorafenib: CTRS_2230;
1376 trametinib: CTRS_2295; Table S15). Differentially expressed genes were identified using cutoffs
1377 of |logFC| > 1.5 and p-value < 0.01. This analysis identified 103 upregulated and 42
1378 downregulated genes following regorafenib treatment, and 32 upregulated and 28 downregulated
1379 genes following trametinib treatment. The upregulated and downregulated gene sets from both
1380 treatments were merged to represent the combined effects of the drug pair.

1381

1382 To calculate MEK inhibitor plus regorafenib signature scores in MB tumor cells, gene expression
1383 profiles were first converted to activity profiles by integrating the medulloblastoma-specific
1384 interactome (MBi) for bulk or single-cell RNA-seq samples. Activity profiles were standardized
1385 using z-transformation. Upregulated and downregulated gene sets were analyzed separately
1386 using the NetBID2 function **cal.Activity.GS** (es.method = "ssgsea"). For each sample, the drug
1387 pair signature score was calculated by subtracting the ssGSEA score of the upregulated gene set
1388 from that of the downregulated gene set, quantifying sensitivity to the combination treatment.

1389

1390 ***Ex vivo* evaluation of MEK inhibitor and regorafenib combination efficacy by AlamarBlue**
1391 **assay**

1392 The viability of D341, MB002, D283, D425, DAOY, SJMBG3-12-5950 (PDX5950), and CTD cells
1393 were assessed in the presence of MEK inhibitors (trametinib or mirdametinib/PD901) in
1394 combination with regorafenib using full dose-response matrices (10×10 concentrations, ranging
1395 from 10 mmol/L to 1 nmol/L Drugs were transferred into 384-well plates using the Echo 650 series
1396 acoustic liquid handler for precise nanoliter-scale dispensing.
1397
1398 Cells were seeded into the drug-treated plates at a density of 1×10^3 cells per 30 μL of medium
1399 and incubated for seven days under standard culture conditions. After seven days, cell viability
1400 was measured using the AlamarBlue assay. Briefly, 10% AlamarBlue reagent was added to the
1401 cells in complete medium, and the plates were incubated for 1-4 hours according to the
1402 manufacturer's protocol. Absorbance was measured using a plate reader to quantify cell viability.
1403 The calculation of synergistic effects was performed as described in the SINBA-guided high-
1404 throughput screening section.
1405
1406 **Drug treatment and western blot**
1407 Human G3 cell lines or mouse mode CTD cells were seeded into 6-well plates and treated with
1408 regorafenib, either alone or in combination with trametinib or mirdametinib, at the indicated
1409 concentrations. After 3 days of treatment(72 h), cells were harvested and lysed in RIPA buffer
1410 supplemented with protease and phosphatase inhibitors (#78440, Thermo Fisher Scientific) for
1411 20 minutes. Total protein extracts were separated by SDS-PAGE and transferred onto
1412 polyvinylidene fluoride (PVDF) membranes (Millipore, USA) using the Trans-Blot Turbo™ transfer
1413 system (Bio-Rad, USA).
1414
1415 The PVDF membranes were blocked with 5% non-fat dry milk in TBS-T for 1 h at room
1416 temperature. Following blocking, the membranes were incubated overnight at 4°C with primary
1417 antibodies (Cell Signaling Technology). After washing three times with TBS-T, the membranes

1418 were incubated with HRP-conjugated secondary antibodies (ABclonal) for 1 h at room
1419 temperature. Protein bands were visualized using an enhanced chemiluminescence (ECL) kit
1420 (ABclonal) and imaged with the Bio-Rad ChemiDoc MP Imaging System.
1421
1422 **Pharmacokinetics of regorafenib, mirdametinib and trametinib in mice**
1423 The plasma and brain pharmacokinetic (PK) profile of regorafenib was evaluated in normal female
1424 Crl:CD1 (ICR) nude mice (7 to 11 weeks old; Charles River Laboratories, Stock Number 086).
1425 Regorafenib monohydrate (MedChem Express, CAT# HY-10331A, LOT# 09764) was suspended
1426 in 80% (propylene glycol 42.5% / polyethylene glycol 400 42.5% / Pluronic F68 15%) and 20%
1427 ultra-pure water (Millipore), at 1 mg/mL for a 10 mg/kg free base equivalent dose. Terminal
1428 samples, one from each mouse, were collected over a 24-hour post-dose period by cardiac
1429 puncture using a 1 mL syringe, the blood placed in a Sarstedt Microvette K3EDTA 500 µL tube
1430 and immediately separated to plasma. The carcass was then perfused with PBS, the brain
1431 extracted, rinsed, and placed in a microcentrifuge tube. All samples were immediately stored on
1432 dry ice and transferred to -80 °C until analysis. Remaining regorafenib dosing suspension was
1433 submitted for verification of potency, and chemical and physical stability during the study period.
1434
1435 For brain exposure studies of trametinib and mirdametinib, 10 mmol/L stock solutions were initially
1436 prepared in DMSO. These stocks were subsequently diluted to a final concentration of 1 mmol/L
1437 using a sequential dilution method with 30% polyethylene glycol 400 (PEG400) and 60%
1438 phosphate-buffered saline (PBS). Intravenous dosing was performed at 5 mL/kg. Samples were
1439 collected as regorafenib study.
1440
1441 Brain exposure was assessed by determining the unbound brain-to-plasma partition ratio ($K_{p,uu}$),
1442 a critical parameter in evaluating central nervous system (CNS) drug penetration and distribution.
1443 $K_{p,uu}$, derived from the total brain-to-plasma partition ratio (K_p), was calculated using Equation (1),

1444 as previously described(51). Unbound drug exposures were estimated based on measured total
1445 drug concentrations in plasma and brain, in combination with experimentally determined fractions
1446 unbound in plasma ($f_{u,plasma}$) and brain tissue ($f_{u,brain}$). Plasma and brain concentration-time data
1447 for the agents were summarized, with the mean values subjected to standard noncompartmental
1448 analysis (NCA) using Phoenix WinNonlin 8.1 (Certara USA, Inc., Princeton, NJ). The apparent
1449 plasma-to-brain partition coefficient (Kp) in mice was estimated as the ratio of the area under the
1450 concentration-time curve (AUC) in brain to the AUC in plasma.
1451
1452
1453 $$K_{p,uu} = K_p \times \frac{f_{u,brain}}{f_{u,plasma}} = \frac{AUC_{brain} \times f_{u,brain}}{AUC_{plasma} \times f_{u,plasma}} \quad (1)$$
1454
1455
1456 ***In vivo* evaluation the efficacy of mirdametinib plus regorafenib**
1457 Luciferase-positive D341 cells (30,000 cells/mouse), PDX5950 (SJMBG3-12-5950) tumor cells
1458 (500,000 cells/mouse), DAOY cells (500,000 cells/mouse) and luciferase-positive CTD cells
1459 (1,000,000 cells/mouse) were resuspended in 5 µL Matrigel (BD Biosciences, 356234) and
1460 stereotactically implanted into the cortices of 7–11-week-old female CD-1 nude mice or male
1461 C57BL/6J mice (for CTD models; The Jackson Laboratory, Cat. 000664). Tumor growth was
1462 monitored weekly using bioluminescence imaging (BLI) with a PerkinElmer IVIS system or
1463 magnetic resonance imaging (MRI), as previously described(123). Treatment was initiated one
1464 week after implantation surgery. Mice were randomized into treatment groups and continuously
1465 dosed for six weeks with vehicle, mirdametinib, regorafenib, or the combination of mirdametinib
1466 and regorafenib. Regorafenib was administered at a fixed dose of 10 mg/kg across all models,
1467 while mirdametinib was dosed at 5 mg/kg for D341 and DAOY models and 0.5 mg/kg for PDX
1468 SJMBG3-12-5950 and CTD models. For combination therapy tested with D341 model, involving

1469 regorafenib (10 mg/kg), mirdametinib (5 mg/kg), and irradiation, radiation was delivered using the
1470 Small Animal Radiation Research Platform (SARRP, Xstrahl Life Sciences). An 8 mmx 11 mm
1471 treatment field was delivered to the brain using opposed lateral beams 0.5 Gy/day for 5 days to a
1472 total dose of 2.5 Gy. Detailed irradiation protocols have been previously published(127).
1473
1474 Mice that reached the experimental endpoint were euthanized, and tumors were harvested and
1475 snap-frozen for molecular analysis. Mice were excluded from the study if they died prematurely,
1476 failed to develop tumors, or required humane euthanasia due to unrelated health conditions
1477 without tumor burden. All experiments were conducted in accordance with the National Institutes
1478 of Health's Guide for the Care and Use of Laboratory Animals and were approved by the St. Jude
1479 Children's Research Hospital (SJCRH) Institutional Animal Care and Use Committee (IACUC
1480 protocol #3078).
1481
1482 Toxicity was assessed weekly by measuring body weight and performing endpoint blood work.
1483 Complete blood counts were obtained from whole blood treated with ethylenediamine tetra-acetic
1484 acid (EDTA) using a Forcyte Hematology Analyzer (Oxford Scientific), which employs impedance
1485 and laser technology. Serum diagnostic chemistry panels were analyzed using the Trilogy
1486 chemistry analyzer (Drew Scientific).
1487
1488 **Visualization Web Portal for Single-Cell Glutamatergic Lineage Developmental Reference**
1489 **and Medulloblastoma Patient Data**
1490 To facilitate data exploration and visualization, we developed two interactive web portals: one for
1491 the glutamatergic lineage reference (https://scminer.stjude.org/study/Glutamatergic-lineage) and
1492 one for medulloblastoma patient data (https://scminer.stjude.org/study/GSE155446). The portals
1493 were built with JavaScript and Vue.js for the frontend, Java and Spring Boot for the backend, and

1494 Neo4j and MySQL databases for efficient data management. The web portal provides access to
1495 three main functionalities: dataset presentation, data visualization, and data downloading.
1496
1497 For glutamatergic lineage analysis, we curated a public scRNA-seq dataset of the human fetal
1498 cerebellum generated with the 10X Chromium platform(66). From this dataset, glutamatergic
1499 lineage cells were filtered by selecting cell populations annotated as "01xNSC,"
1500 "06xGCP_progenitor," "07xGCP_1," "08xGCP_2," "09xGranule_cell," "10xUBC_progenitor,"
1501 "11xDiff.UBC," and "11xUBC" in the original study. To account for major sequencing batch effects,
1502 present in the dataset, UMAP-level batch correction was performed using Harmony prior to
1503 downstream clustering and visualization. Unsupervised Leiden clustering, combined with
1504 previous annotations and manual curation informed by known lineage markers, resulted in the
1505 identification of seven distinct glutamatergic lineage cell types: neural stem cells (NSC), rhombic
1506 lip progenitors (RL_pro), unipolar brush cell and granule cell precursor common progenitors
1507 (UBC_GCP_pro), unipolar brush cell progenitors (UBC_pro), granule cell precursors (GCP),
1508 granule cells (GC), and unipolar brush cells (UBC).
1509
1510 For medulloblastoma patient data, single-cell RNA-seq profiles from 28 pediatric tumors (1 WNT,
1511 9 SHH, 7 Group 3, 11 Group 4; GEO accession GSE155446) were processed using the Seurat
1512 workflow, with batch correction via Harmony. Cell type annotations were adopted from the original
1513 publication or re-annotated using the glutamatergic lineage reference.
1514
1515 Both portals integrate single-cell expression profiles with the medulloblastoma-specific
1516 interactome (MBi), utilizing the scMINER algorithm(73) to generate activity profiles. Users can
1517 query both gene expression and activity profiles for any given list of driver genes. The portal
1518 supports various visualization tasks, including clustering UMAPs, heatmaps, bubble plots, violin

1519 plots, and network plots, enabling users to explore lineage-specific patterns and driver activity in
1520 a user-friendly environment.
1521
1522 **Pseudotime trajectory analysis for the glutamatergic lineage cells**
1523 The differentiation trajectory of glutamatergic lineage cells was reconstructed using Slingshot(115)
1524 (v2.10) and Monocle 3(128) (v1.3). The UMAP projection of glutamatergic lineage cells was
1525 imported from a Seurat object for downstream analysis. For pseudotime calculation with Slingshot,
1526 the slingshot function was applied to compute the arc length from the starting point (neural stem
1527 cells, NSC) to all projected points along the principal curve, assigning pseudotime values to each
1528 cell. To construct the trajectory with Monocle 3, sample-based batch effects were corrected using
1529 the align_cds function. The UMAP projection was imported from the Seurat object, and the
1530 differentiation trajectory was generated using the learn_graph function. NSC cells were selected
1531 as the starting point for the pseudotime trajectory. The trajectory, aligned with the UMAP
1532 projections, was visualized using the plot_cells function in Monocle 3.
1533
1534 **Deconvolution of Glutamatergic Lineage Developmental States in Bulk RNA-seq Samples**
1535 **of MB Patients or PDOX**
1536 To prepare the dataset for deconvolution, we normalized the reference glutamatergic lineage
1537 single-cell counts to 1×10^6 and used the seven cell type annotations as input for ReDeconv
1538 package(71) built-in functions **get_initial_Signature_Candidates** and
1539 **Get_signature_gene_matrix**. The following parameters were applied:
1540 - L_topNo = 200
1541 - L_max_pv = 0.05
1542 - L_min_fold_change = 2.0
1543 - L_CellType_CellNo_LB = 30

1544 • L_NoSep_sampleNo_UB = 2

1545

1546 After generating the glutamatergic lineage cell type signature gene matrix, we applied the
1547 **ReDeconv** function to deconvolute glutamatergic lineage developmental state proportions in bulk
1548 RNA-seq samples from public medulloblastoma patient datasets and patient-derived orthotopic
1549 xenograft (PDOX) bulk RNA-seq data, which were quantified as FPKM. The seven cell type
1550 signature matrix served as input for this deconvolution process, allowing us to estimate the
1551 relative proportions of developmental states in each bulk RNA-seq sample.

1552

1553 **Single-cell RNA-seq profiling of human cell line D341 and mouse model CTD *in vitro***

1554 Cells from either the mouse syngeneic G3 MB model (CTD) or the human G3 MB cell line (D341)
1555 were dissociated with Accutase (Stemcell Technologies, Cat# 07922) at 37°C for 5 minutes. Then
1556 we input 8000 cells with 80% viability to the workflow of 3' gene expression of 10x genomics. The
1557 10x Genomics Chromium controller instrument was used for Gel Bead-in-Emulsion (GEMs)
1558 preparation. Gel Bead-in-Emulsion (GEM) generation was performed using the Chromium
1559 Controller, followed by single-cell library preparation using Chromium Next GEM Single Cell 3′ Kit
1560 v3.1 (PN-1000269), Chromium Next GEM Chip G Single Cell Kit (PN-1000127) and Dual Index
1561 Kit TT Set A (PN-1000215). cDNA and final barcoded sequencing libraries were constructed
1562 following the manufacturer's guidelines and subsequently assessed for quality and concentration
1563 using Tapestation.

1564

1565 **Single-cell RNA-seq profiling of human model and mouse model after treatment in**
1566 **preclinical study**

1567 *In vivo*-implanted D341 mouse tumors were harvested at the endpoint. Tumor tissues were
1568 minced and digested at 37°C for 30 minutes using the Human Tumor Dissociation Kit (Miltenyi
1569 Biotec, catalog no. 30-095-929). Red blood cells were removed by treatment with ACK lysis buffer

1570 (Thermo Fisher Scientific, catalog no. A1049201). The digested tissues were then passed through
1571 a 70 μm cell strainer to obtain a single-cell suspension. Approximately 8,000 cells with over 80%
1572 viability were selected and processed using the Flex Gene Expression workflow from 10x
1573 Genomics for downstream analysis.
1574
1575 Mouse CTD tumors were harvested at end point. Mouse tissues were minced and digested at
1576 37°C for 1 h (1mg/mL papain, 10 μg/mL DNase I, 10% heat-inactivated FBS in RPMI) to dissociate
1577 cells. Red blood cells were lysed with ACK lysis buffer (Thermo Fisher Scientific, catalog no.
1578 A1049201). Then tissues were passed through 70 μm cell strainer to get single-cell suspension.
1579 Then cells were incubated with CD16/32 antibody (Miltenyi Biotec, Cat#130-092-575) for 20
1580 minutes on ice to block Fc receptors. Next, they were stained with PE-CD45 antibody (Biolegend,
1581 Cat# 157603) on ice for 20 minutes and DAPI (1ug/ml) on ice for 3 minutes. Then live immune
1582 cells (CD45+) and tumor cells (YFP+) were sorted by FACS and combined for downstream library
1583 preparations.
1584
1585 Then we input 8000 cells with 80% viability to the workflow of Flex gene expression of 10x
1586 genomics. The 10x Genomics Chromium controller instrument was used for Gel Bead-in-
1587 Emulsion (GEMs) preparation. Gel Bead-in-Emulsion (GEM) generation was performed using the
1588 Chromium Controller, followed by single-cell library preparation using GEM-X Flex Sample
1589 Preparation v2 Kit (PN-1000781), GEM-X Flex Gene Expression Chip Kit (PN-1000791), GEM-X
1590 Flex Gene Expression Mouse Transcriptome probe kit (PN-1000786) and Dual Index Kit TT Set A
1591 (PN-1000215). cDNA and final barcoded sequencing libraries were constructed following the
1592 manufacturer's guidelines and subsequently assessed for quality and concentration using
1593 Tapestation.
1594
1595 **Single-cell RNA-seq data analysis**

1596 Raw sequencing data generated from the Illumina NovaSeq platform were processed using the
1597 Cell Ranger pipeline (version 8.0.1, 10X Genomics). This pipeline performed demultiplexing,
1598 alignment to the reference genome (hg GRCh38 or mm39), and barcode processing to produce
1599 gene–cell matrices for downstream analysis. To ensure consistent filtering, datasets from in vivo
1600 samples treated with either vehicle or drug were merged into a single dataset.
1601
1602 Unsupervised clustering of single-cell RNA sequencing (scRNA-seq) data was performed using
1603 the R package Seurat(111) (version 5.3.0). Cells were filtered based on quality metrics, excluding
1604 those with low or high unique molecular identifier (UMI) counts, low or high gene numbers, or
1605 elevated mitochondrial gene expression (>10%). Gene expression levels were normalized to
1606 10,000 UMIs per cell and log-transformed by adding 1 to the expression matrix. Highly variable
1607 genes (top 2000) were identified using Seurat's "vst" method, which were subsequently used for
1608 principal component analysis (PCA). The first 30 principal components (PCs) were utilized for
1609 dimensionality reduction via uniform manifold approximation and projection (UMAP) and
1610 clustering. Cell type markers were applied to annotate tumor cell types within each cluster.
1611
1612 **Drug signature score calculation in normal immune cells**
1613 Context-matched gene signatures induced by regorafenib and mirdametinib were curated from
1614 bone marrow dataset (regorafenib: SCP_87407; mirdametinib: SCP_86814; Table S15) using
1615 cutoffs of |logFC| > 1.5 and p-value < 0.05. This yielded 48 upregulated and 55 downregulated
1616 genes for mirdametinib, and 58 upregulated and 93 downregulated genes for regorafenib.
1617
1618 For normal cells, gene expression values in each single cell were standardized, and the drug
1619 signature score was calculated by subtracting the ssGSEA score of the upregulated gene set
1620 from the ssGSEA score of the downregulated gene set for the mirdametinib-regorafenib
1621 combination.

1622

1623 **Cell–cell interaction analysis**

1624 Cell–cell interaction analysis was conducted using samples from 16 mice (4 mice per treatment
1625 arm) profiled with the 10x Flex Gene Expression platform. Interactions were analyzed using
1626 CellChat (V2.1.2), focusing on secreted signaling ligand-receptor pairs from the CellChatDB
1627 database. The selected cell types included: "Tcm," "Teffector," "Tex," "Tfh," "Th17," "Treg,"
1628 "Mono," "Macrophage" "Microglia" and "Tumor" The number and strength of inferred interactions
1629 were analyzed between the 10 selected cell types. Differential interaction strength was compared
1630 between each treatment arm and the control group. Additionally, the relative interaction strength
1631 and information flow for specific receptor-ligand signaling pathways were assessed.

1632

1633 **Data Availability**

1634 The 10x Genomics single-cell RNA-seq data generated in this study are available from NCBI GEO
1635 under accession numbers GSE308633, GSE308635, GSE308649, and GSE308692. SINBA
1636 package is available on GitHub (https://github.com/jyyulab/SINBA). Additional resources include
1637 the SINBA medulloblastoma portal (https://yulab-stjude.shinyapps.io/SINBA_MB), the normal
1638 glutamatergic lineage developmental reference portal
1639 (https://scminer.stjude.org/study/Glutamatergic-lineage), and the medulloblastoma patient
1640 scRNA-seq portal (https://scminer.stjude.org/study/GSE155446). 10x Genomics scRNA-seq data
1641 from developing human cerebellum and medulloblastoma patients were obtained from Luo et
1642 al.(66) and are also available via the China National GeneBank Data Base (CNP0002781).
1643 Additional medulloblastoma patient 10x scRNA-seq data were downloaded from GEO
1644 (GSE155446), and Smart-seq2 scRNA-seq data from GEO (GSE119926).

1645 **Supplementary Figures**

1646

1647 **Figure S1. Druggable hidden drivers in high-risk medulloblastoma**

1648 **A,** Heatmap displaying druggable hidden driver activities and expressions in three
1649 medulloblastoma cohorts. **B,** Druggable hidden driver genes identified by the SINBA algorithm
1650 were evaluated for association with overall survival in the GSE85217 cohort. MB Patients were
1651 stratified by high (>75th percentile) versus low (<25th percentile) gene expression or activity.
1652 Kaplan–Meier survival analysis; p values calculated by log-rank test. **C,** Kaplan–Meier curves
1653 showing overall survival of MB patients stratified by BRAF or CDK7 activity or expression.
1654 **D,** BRAF activity, mRNA expression, total protein and phosphorylated BRAF (S1264) levels
1655 across MB subgroups and normal samples. **E,** CDK7 activity, mRNA expression, total protein and
1656 phosphorylated CDK7 (S164/T170) levels across MB subgroups and normal samples. **F,** Kaplan–
1657 Meier curves showing overall survival of MB patients stratified by MYC activity or expression.
1658 **G,** MYC activity, mRNA expression, total protein and phosphorylated MYC (T365) levels across
1659 MB subgroups and normal samples.
1660 For (**D**), (**E**), and (**G**), unpaired two-sided t tests were performed between G3 MB and other
1661 subgroups. For (**C**) and (**F**), P value was calculated by log-rank test.

1662

1663 **Figure S2. SINBA-guided multi-step drug screening identifies potential therapeutic**
1664 **combinations for high-risk medulloblastoma**

1665 **A,** Seed and partner drugs with half-maximal effective concentrations (EC50) below 10 μM.
1666 **B,** Summary of HTS results from the seed drug and partner drug libraries. **C,** Overview of two-
1667 dose combination screening outcomes. **D,** Representative contour plots showing HDMB03 cell
1668 growth inhibition across varying concentrations of trametinib, axitinib or ponatinib in combination
1669 with regorafenib.

1670

1671 **Figure S3. Pharmacokinetic profile of the MEK inhibitors and regorafenib**

1672 **A,** Pharmacokinetic profile of regorafenib: plasma and brain concentrations measured over 24
1673 hours post-dose with the statistical analysis of regorafenib plasma and brain concentration–time
1674 (Ct) profiles. **B-C**, Pharmacokinetic profiles of trametinib and mirdametinib: plasma and brain
1675 concentrations measured over 4 hours post-dose. **D,** Chemical proteomic profiling of clinical
1676 kinase inhibitors, showing predicted interaction targets of trametinib, mirdametinib, and
1677 regorafenib. **E,** Comparative analysis of driver activity within the KEGG MAPK signaling cascade
1678 between G3 and normal samples in the DKFZ_SJ cohort. Nodes are color-coded according to Z-
1679 score (normalized p value) differentials reflecting G3 versus normal cerebellum. Genes targeted
1680 by trametinib and regorafenib are accentuated in magenta.

1681 For (**A**), (**B**), and (**C**), each time point data are represented as mean ± SEM.

1682

1683 **Figure S4. Drug sensitivity and synergy analysis for MEK inhibitor and regorafenib**
1684 **combinations in medulloblastoma models**

1685 **A,** Schematic representation of the drug sensitivity calculation framework, leveraging CNS-
1686 specific drug signatures from the iLINCS database to identify responsive medulloblastoma models.
1687 Refer to the Methods section for further details. **B,** Surface plots of ZIP synergy score landscapes
1688 for trametinib plus regorafenib (left) and mirdametinib plus regorafenib (right) in the DAOY cell
1689 line. **C,** Surface plots of ZIP synergy score landscapes for trametinib plus regorafenib (left) and
1690 mirdametinib plus regorafenib (right) in the D425 cell line. **D,** Contour plots of cell viability and
1691 surface plots of ZIP synergy score landscapes for trametinib plus regorafenib (left) and
1692 mirdametinib plus regorafenib (right) in D283 cells.

1693

1694 **Figure S5. The MEKi + regorafenib combination lacks synergistic efficacy in the SHH model**
1695 **DAOY and shows no significant toxicity in mice**

1696 **A,** Kaplan–Meier survival curves for mice implanted with DAOY cells and treated as in Figure 3A.
1697 Group sizes (n) are indicated in the risk table; log-rank test: ns, not significant. **B,** Quantified
1698 bioluminescence imaging (BLI) for each treatment group in the DAOY model at week 3 post-
1699 treatment. Data are mean ± SEM. **C,** Weekly body weight changes in D341-bearing mice after
1700 surgery. Data are represented as mean ± SEM. **D,** Endpoint toxicity assessment by complete
1701 blood counts (n = 2–4 per group) in the D341 study; dashed lines indicate normal reference
1702 ranges. **E,** Weekly body weight changes in PDX5950-bearning mice after surgery. Data are
1703 represented as mean ± SEM. F, Endpoint toxicity assessment by complete blood counts (n = 2–
1704 4 per group) in the PDX5950 study.
1705 For (**B**) unpaired two-sided t tests were used. *P < 0.05, **P < 0.01, ***P < 0.001; ns, not significant.
1706 For (**D**) and (**F**), one-way ANOVA was performed among treatment groups.
1707
1708 **Figure S6. Evaluating the combination of mirdametinib, regorafenib, and radiation**
1709 **therapy in the D341 Model**
1710 **A,** Schematic of experimental design for drug administration and bioluminescence imaging (IVIS)
1711 in CD-1 nude mice (created with BioRender.com). Mice with intracranial D341 cell implants were
1712 randomized into four treatment groups: vehicle (p.o.), drug combination (Comb: mirdametinib at
1713 5 mg/kg p.o. and Regorafenib at 10 mg/kg p.o.), radiation therapy (RT: 0.5 Gy/day for 5
1714 consecutive days), concurrent RT + drug combination (RT_Con), or sequential RT + drug
1715 combination (RT_Seq). Treatments commenced one week post-implantation and continued for
1716 six weeks. **B,** Kaplan–Meier survival curves for mice treated as described in (A). Group sizes (n)
1717 are indicated in the risk table; log-rank test results: *P < 0.05, **P < 0.01, ***P < 0.001. **C,**
1718 Quantified bioluminescence imaging (BLI) measurements for each treatment group in the D341
1719 model at week 3 post-treatment enrollment. Data are represented as mean ± SEM. Unpaired two-
1720 sided t tests were used. *P < 0.05, ns, not significant. **D,** Weekly body weight changes in D341-

1721 bearing mice after surgery. Data are represented as mean ± SEM. E, Endpoint toxicity
1722 assessment by complete blood counts (n = 2–4 per group) in the D341 study as shown in (**A**).
1723
1724 **Figure S7. Enrichment of UBC_GCP_pro and UBC_pro like tumor cells in G3 and G4 MB**
1725 **revealed by scRNA-seq**
1726 **A,** UMAP plot showing developmental trajectories of normal glutamatergic lineage neurons
1727 inferred by Slingshot. **B,** UMAP plot of pseudotime trajectories generated by Monocle3, with cells
1728 colored by inferred developmental time. **C-D,** UMAP plots displaying medulloblastoma tumor
1729 subgroup and cell type annotations from the original study (GSE156053; Riemondy et al.). **E,**
1730 UMAP plot of tumor cell state and normal cell types (GSE156053). **F-G,** UMAP plots of two
1731 medulloblastoma patient scRNA-seq datasets, annotated by MB subgroup or cell type. **H-I,**
1732 Proportional distribution of tumor cell states in individual medulloblastoma patients.
1733
1734 **Figure S8. UBC_GCP_Pro like tumor cells exhibiting the highest driver activities and drug**
1735 **signature scores**
1736 **A,** Transcriptomic deconvolution of RNA-seq profiles via the ReDeconv algorithm across three
1737 independent medulloblastoma patient cohorts and a PDOX dataset, stratified by cellular
1738 subpopulations as delineated in Figure 5A. **B,** Feature plot of driver combination activities and
1739 drug signature scores in malignant cells and normal immune cells (GSE156053). **C-D,** Feature
1740 and violin plots of BRAF and MAPK11 expression in tumor cells (GSE156053).
1741 **E,** Feature and violin plots of driver combination activity and drug signature scores in the normal
1742 reference. **F,** Feature and violin plots of BRAF and MAPK11 expression in the normal reference.
1743 **G,** UMAP of D341 cell clusters and tumor cell states. **H,** Proportional distribution of tumor cell
1744 states in D341. I, Feature and violin plots showing driver combination activities and predicted drug
1745 sensitivity scores across tumor cell sate.

1746 For (**D**), (**E**), and (**F**), unpaired two-sided t tests were used to compare progenitor-like
1747 UBC_GCP_pro and GCP_pro cells with mature-like UBC cells. For (**I**), unpaired two-sided t tests
1748 were used to compare UBC_GCP_pro with UBC_pro cells.
1749

1750 **Figure S9. Effects of combination therapy on CTD tumor cells and tumor**
1751 **microenvironment**

1752 **A,** Tumor cell states in CTD mapped using normal reference marker genes (Figure 5A), with bar
1753 plot showing proportions of CTD cell states. **B,** Feature and violin plots of driver combination
1754 activities and predicted drug sensitivity scores across tumor cell states in the CTD model. Two-
1755 sided t tests were used to compare RL_pro with UBC_GCP_pro and UBC_pro. *P < 0.05, **P <
1756 1.0e-10, ***P < 1.0e-20. **C,** Dot plot showing marker gene expression patterns in immune cell
1757 types and tumor cells. **D,** Feature and violin plots of driver combination activities and predicted
1758 drug sensitivity scores across treatment arms from CTD preclinical study. **E,** Violin plots of driver
1759 combination activities and predicted drug sensitivity scores across tumor cell states. **F,** Dot plot
1760 showing antigen presentation gene expression in tumor cells across the four treatment groups.
1761 **G,** Gene set enrichment analysis of M2-macrophage related genes in macrophages, comparing
1762 combination treatment versus other treatment groups.
1763

1764 **Figure S10. The combination of MEK inhibition and regorafenib reconfigures the tumor**
1765 **microenvironment**

1766 **A,** Dot plot of mirdametinib and regorafenib drug signature scores in immune cells across four
1767 treatment groups. **B,** Violin plot of mirdametinib and regorafenib drug signature scores across
1768 immune cell types; two-sided t test comparing Treg cells with other immune cells. **C,** Volcano plot
1769 of differentially expressed genes in CD8+ T cells from the MIR_REG combination group versus
1770 other treatments. **D,** Dot plot showing immune therapy–related target gene expression in CD8+ T
1771 cells across treatment groups. **E,** Module scores for immune therapy target genes; two-sided t

1772 tests comparing combination treatment with other groups. *P < 0.05, **P < 1.0e-10, ***P < 1.0e-
1773 20. **F,** Feature plot of Il18 expression in immune cells from the CTD model. **G,** Violin plot of Il18
1774 expression across immune cell types; two-sided t test comparing monocytes with other immune
1775 cells. **H,** Feature plots of Il18r1 and Il18rap expression in immune cells from the CTD model. **I,**
1776 Dot plot of Il18r1 and Il18rap expression in T cells across four treatment groups. **J-K,** Feature and
1777 violin plots of Ccl3, Ccl4, and Ccr5 expression in CD8+ T cells across treatment groups; two-sided
1778 t test comparing combination treatment with other groups.

1779 **Supplementary Tables**

1780

1781 **Table S1. Unique genes, drugs, interactions, and drug phases in the six built-in drug-gene**
1782 **interaction databases, related to Figure 1.**

1783 **Table S2. Bulk RNA-seq profiles from medulloblastoma patient cohorts, related to Figure**
1784 **1, Supplementary Figure S1 and S8.**

1785 **Table S3. The correlation between seed-driver activity or expression with MB patient**
1786 **survival, related to Supplementary Figure S1.**

1787 **Table S4. Seed drug and partner drug libraries for HTS, related to Figure 1 and**
1788 **Supplementary Figure S2.**

1789 **Table S5. Two-dose combination screening, related to Figure 1 and Supplementary Figure**
1790 **S2.**

1791 **Table S6. 10-dose combination screening, related to Figure 1.**

1792 **Table S7. Normal glutamatergic lineage neuron developmental reference 10x scRNA-seq**
1793 **data QC, related to Figure 5.**

1794 **Table S8. MB patients sample information from the public single-cell RNA-seq datasets,**
1795 **related to Figure 5, Supplementary Figure S7, and S8.**

1796 **Table S9. GSE155446 MB patient 10x scRNA-seq data QC, related to Figure 5,**
1797 **Supplementary Figure S7 and S8.**

1798 **Table S10. Hovestadt et al. MB patient SMART-seq2 data QC, related to Supplementary**
1799 **Figure S7.**

1800 **Table S11. Luo et al. MB patient 10x scRNA-seq data QC, related to Supplementary Figure**
1801 **S7.**

1802 **Table S12. D341 *in vivo* 10x scRNA-seq data QC table, related to Figure 5.**

1803 **Table S13. CTD *in vivo* 10x scRNA-seq data QC table, related to Figure 7, Supplementary**
1804 **Figure S9 and S10.**

1805 **Table S14. M1/G2 microphage signature gene sets, related to Supplementary Figure S9.**

1806 **Table S15. Trametinib, regorafenib and mirdametinib drug signature genes sets, related to**

1807 **Figure 2, 4, 5 and Supplementary Figure S4, S8, S9 and S10.**

Figure 1

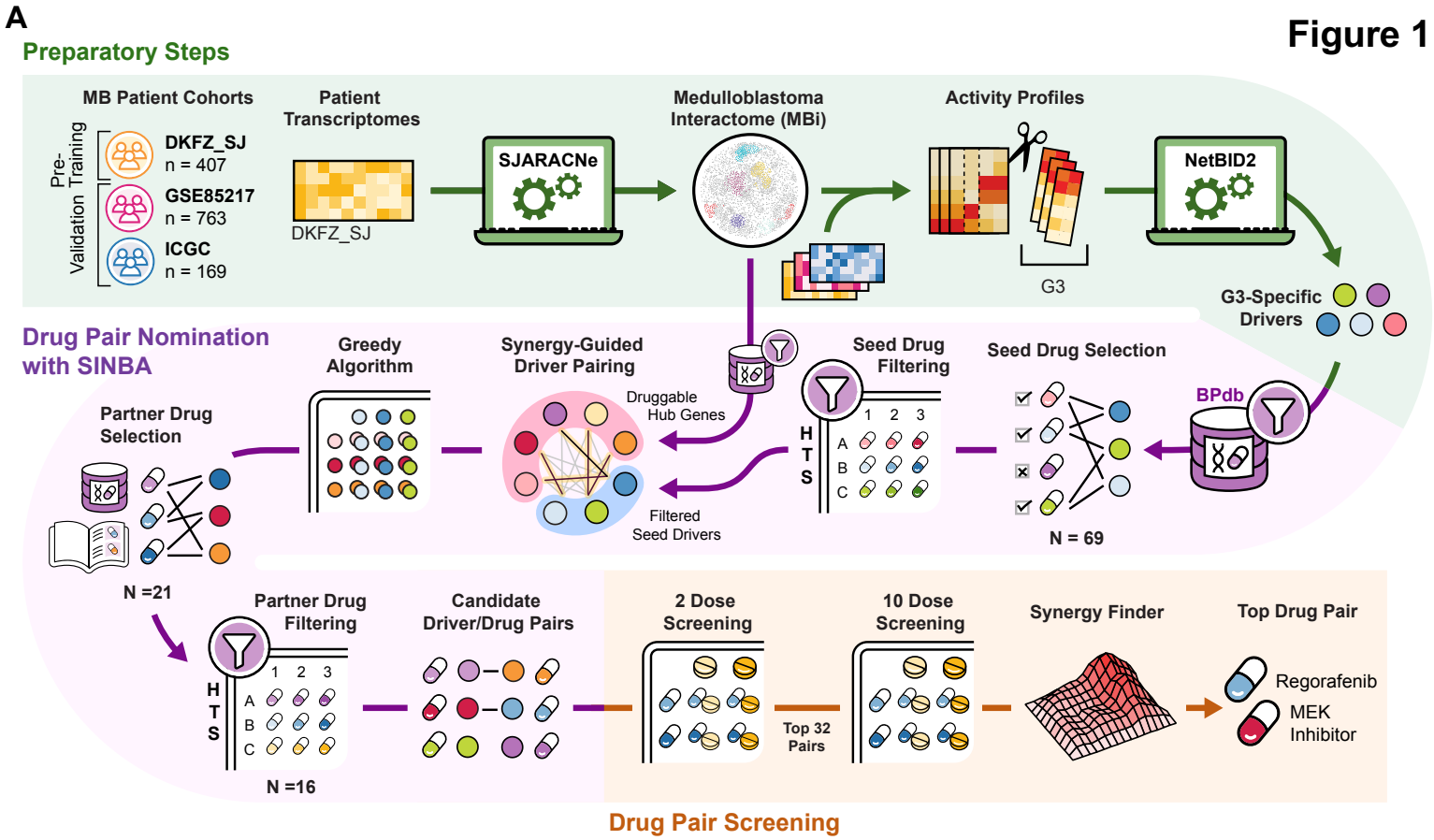
A
Preparatory Steps
MB Patient Cohorts
Pre-Training
Vaidation
DKFZ_SJ
n = 407
GSE85217
n = 763
ICGC
n = 169
Patient Transcriptomes
DKFZ_SJ
SJARACNe
Medulloblastoma Interactome (MBi)
Activity Profiles
G3
NetBID2
G3-Specific Drivers
Drug Pair Nomination with SINBA
Greedy Algorithm
Synergy-Guided Driver Pairing
Druggable Hub Genes
Filtered Seed Drivers
Seed Drug Filtering
HTS
1 2 3
A
B
C
Seed Drug Selection
BPdb
N = 69
Partner Drug Selection
N =21
Partner Drug Filtering
N =16
Candidate Driver/Drug Pairs
2 Dose Screening
Top 32 Pairs
10 Dose Screening
Synergy Finder
Top Drug Pair
Regorafenib
MEK Inhibitor
Drug Pair Screening

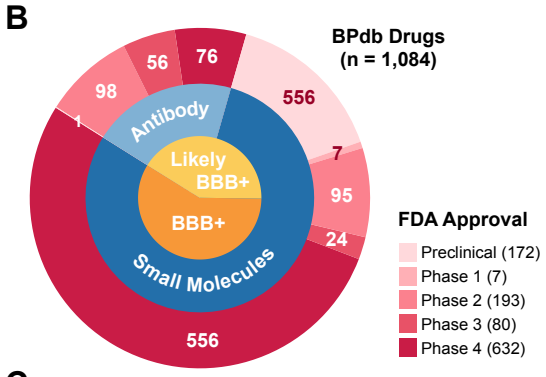
B
BPdb Drugs (n = 1,084)
Antibody
Likely BBB+
BBB+
Small Molecules
76
556
7
95
24
556
1
98
56
FDA Approval
Preclinical (172)
Phase 1 (7)
Phase 2 (193)
Phase 3 (80)
Phase 4 (632)

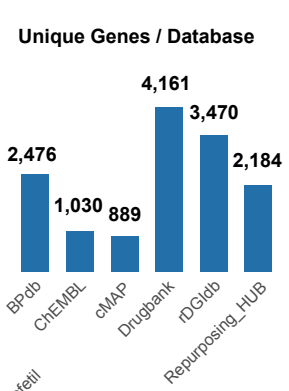
Unique Genes / Database
2,476
1,030
889
4,161
3,470
2,184
BPdb
ChEMBL
cMAP
Drugbank
rDGIdb
Repurposing_HUB

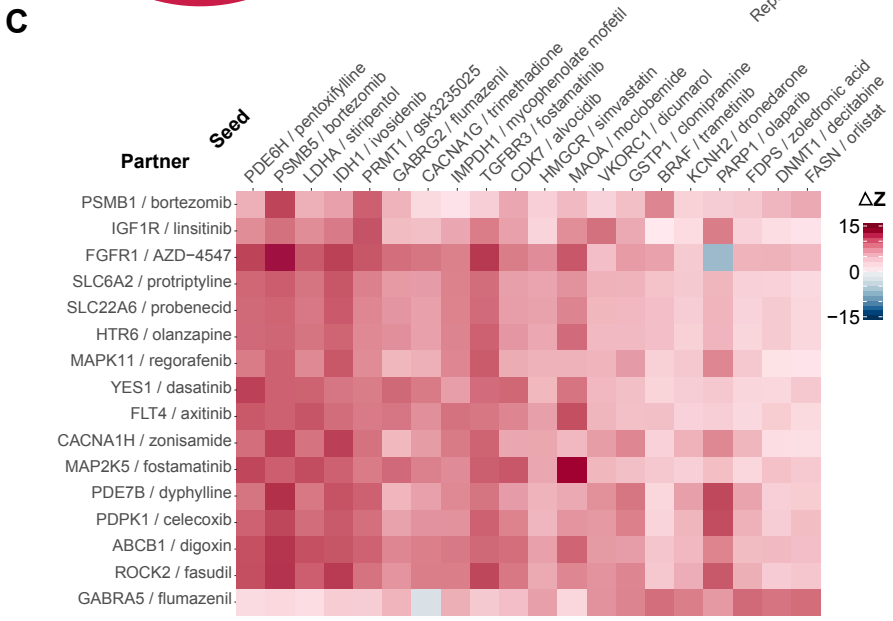
C
Seed
Partner
PDE6H / pentoxifylline
PSMB5 / bortezomib
LDHA / stiripentol
IDH1 / ivosidenib
PRMT1 / gsk3235025
GABRG2 / flumazenil
CACNA1G / trimethadione
IMPDH1 / mycophenolate mofetil
TGFBR3 / fostamatinib
CDK7 / alvocidib
HMGCR / simvastatin
MAOA / moclobemide
VKORC1 / dicumarol
GSTP1 / clomipramine
BRAF / trametinib
KCNH2 / dronedarone
PARP1 / olaparib
FDPS / zoledronic acid
DNMT1 / decitabine
FASN / orlistat
PSMB1 / bortezomib
IGF1R / linsitinib
FGFR1 / AZD−4547
SLC6A2 / protriptyline
SLC22A6 / probenecid
HTR6 / olanzapine
MAPK11 / regorafenib
YES1 / dasatinib
FLT4 / axitinib
CACNA1H / zonisamide
MAP2K5 / fostamatinib
PDE7B / dyphylline
PDPK1 / celecoxib
ABCB1 / digoxin
ROCK2 / fasudil
GABRA5 / flumazenil
ΔZ
15
0
−15

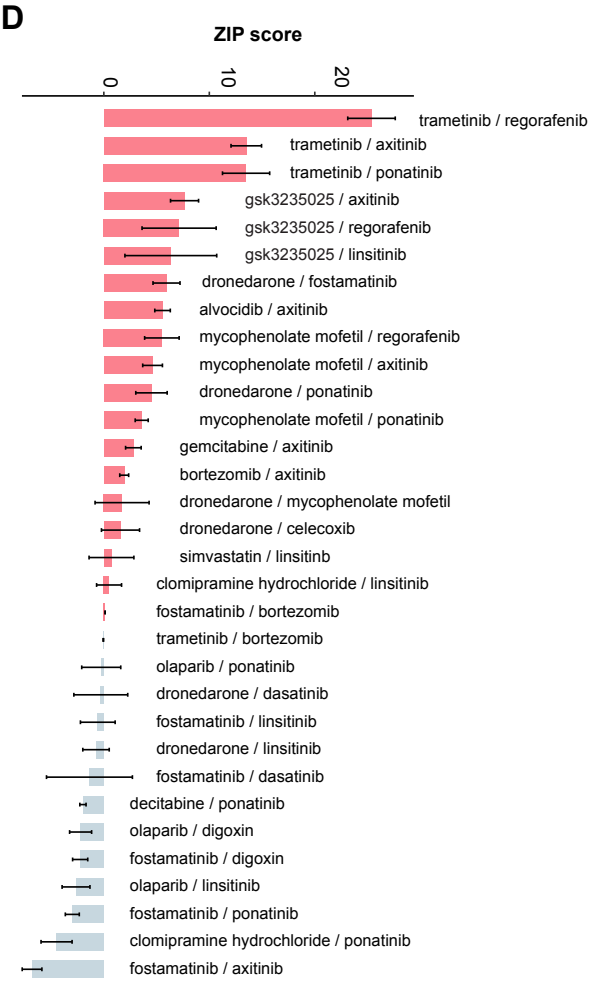
D
ZIP score
0
10
20
trametinib / regorafenib
trametinib / axitinib
trametinib / ponatinib
gsk3235025 / axitinib
gsk3235025 / regorafenib
gsk3235025 / linsitinib
dronedarone / fostamatinib
alvocidib / axitinib
mycophenolate mofetil / regorafenib
mycophenolate mofetil / axitinib
dronedarone / ponatinib
mycophenolate mofetil / ponatinib
gemcitabine / axitinib
bortezomib / axitinib
dronedarone / mycophenolate mofetil
dronedarone / celecoxib
simvastatin / linsitinb
clomipramine hydrochloride / linsitinib
fostamatinib / bortezomib
trametinib / bortezomib
olaparib / ponatinib
dronedarone / dasatinib
fostamatinib / linsitinib
dronedarone / linsitinib
fostamatinib / dasatinib
decitabine / ponatinib
olaparib / digoxin
fostamatinib / digoxin
olaparib / linsitinib
fostamatinib / ponatinib
clomipramine hydrochloride / ponatinib
fostamatinib / axitinib

Figure 2

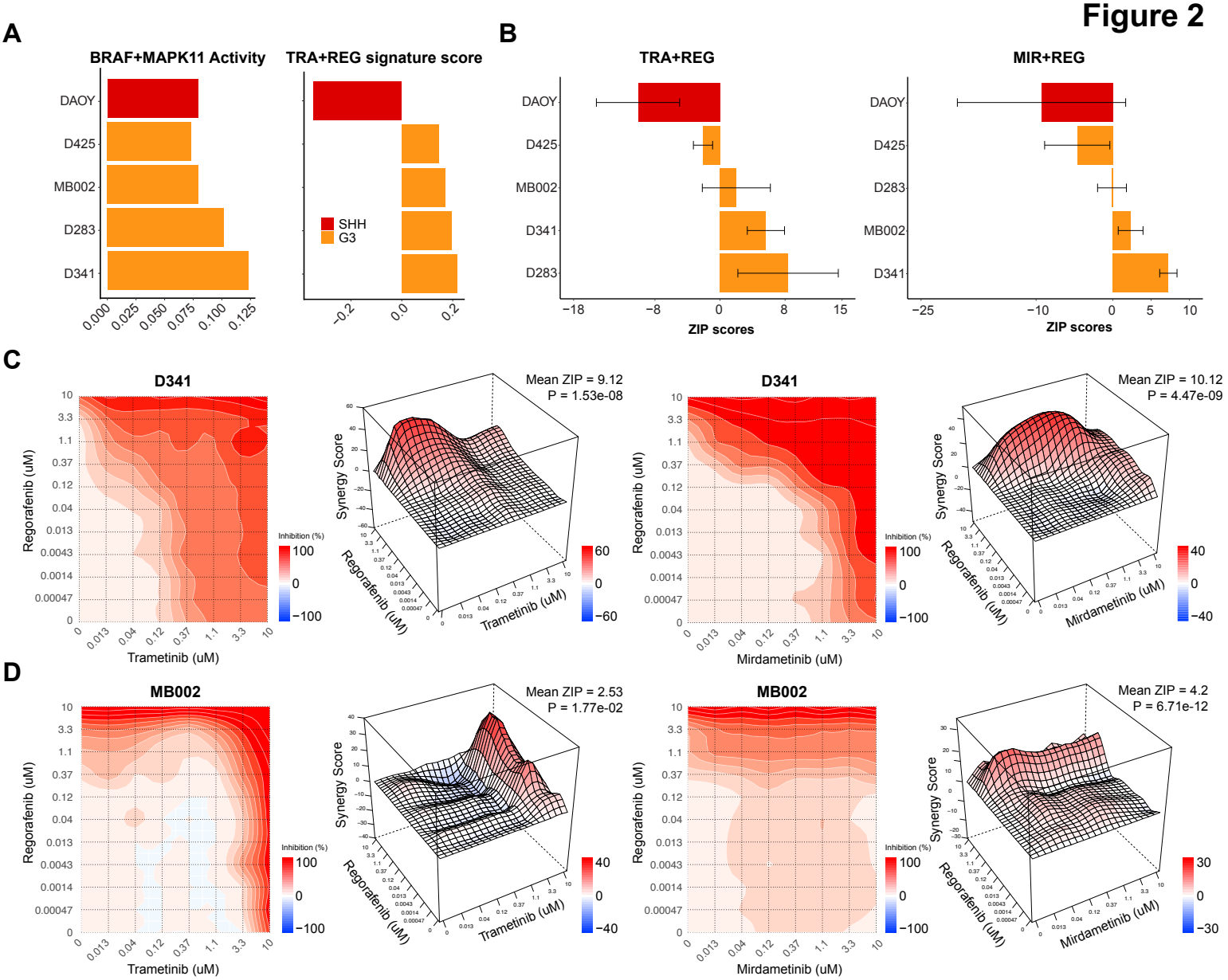
A
BRAF+MAPK11 Activity
TRA+REG signature score
DAOY
D425
MB002
D283
D341
SHH
G3
B
TRA+REG
MIR+REG
ZIP scores
C
D341
Mean ZIP = 9.12
P = 1.53e-08
Mean ZIP = 10.12
P = 4.47e-09
Regorafenib (uM)
Trametinib (uM)
Mirdametinib (uM)
Synergy Score
Inhibition (%)
D
MB002
Mean ZIP = 2.53
P = 1.77e-02
Mean ZIP = 4.2
P = 6.71e-12

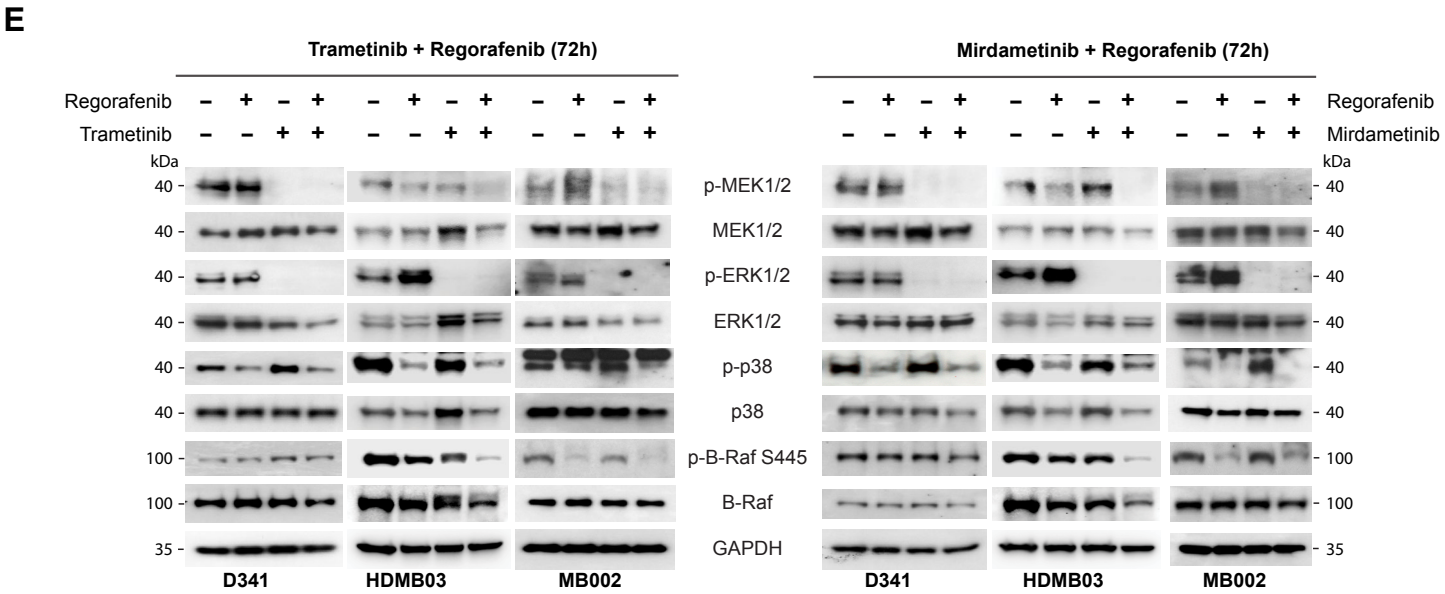
E
Trametinib + Regorafenib (72h)
Mirdametinib + Regorafenib (72h)
Regorafenib
Trametinib
Mirdametinib
kDa
p-MEK1/2
MEK1/2
p-ERK1/2
ERK1/2
p-p38
p38
p-B-Raf S445
B-Raf
GAPDH
D341
HDMB03
MB002

Figure 3

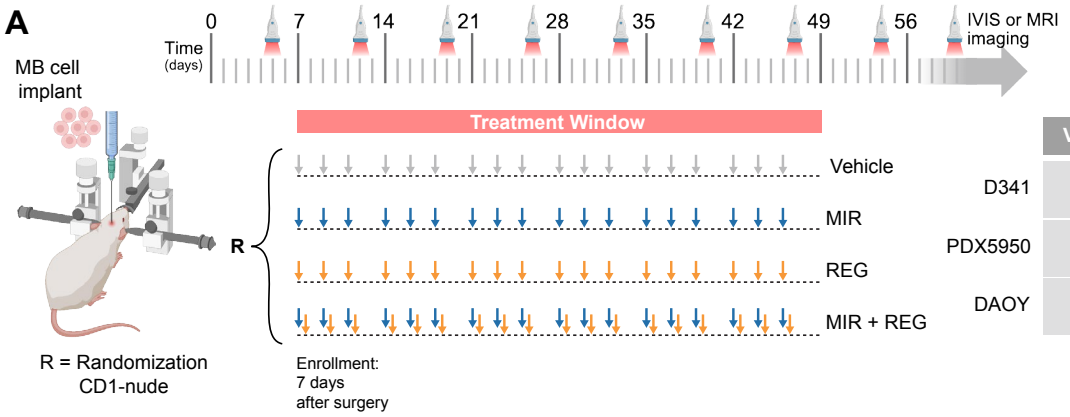

	Vehicle	MIR	REG	MIR + REG
D341	0	5 mg/kg	10 mg/kg	5 mg/kg 10 mg/kg
PDX5950	0	0.5 mg/kg	10 mg/kg	0.5 mg/kg 10 mg/kg
DAOY	0	5 mg/kg	10 mg/kg	5 mg/kg 10 mg/kg

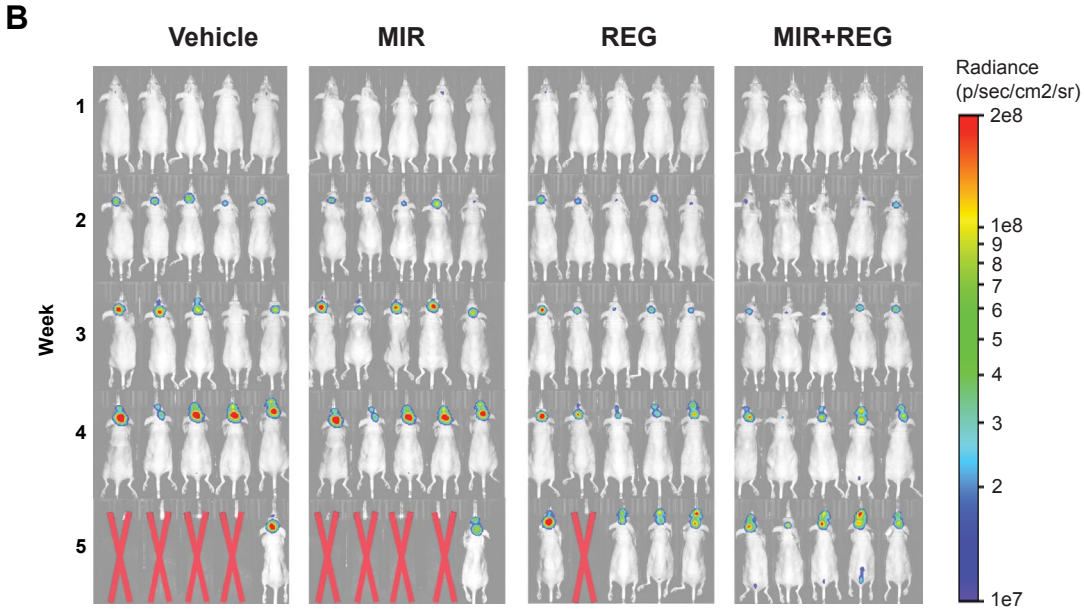

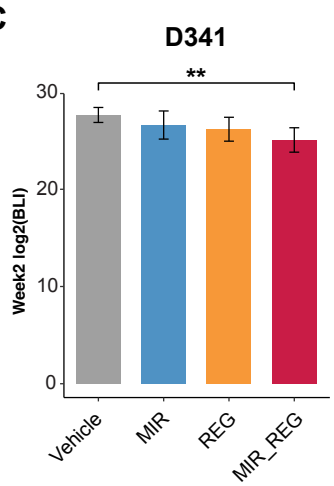

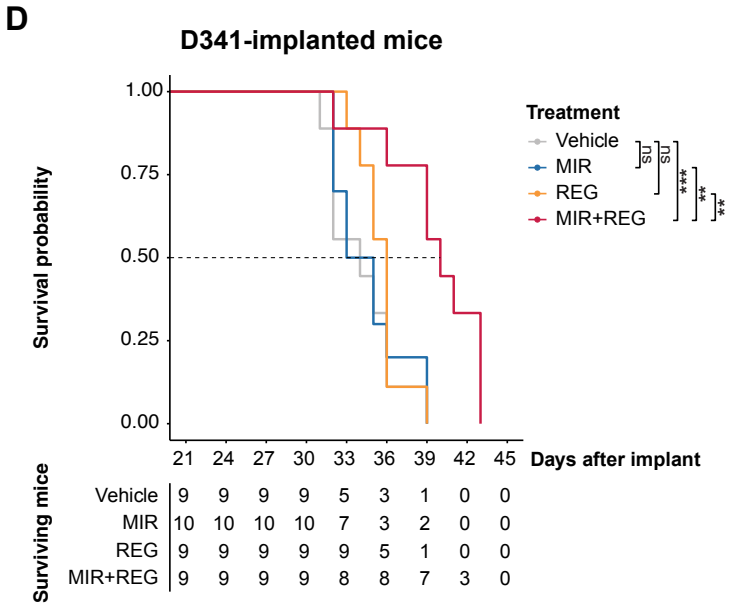

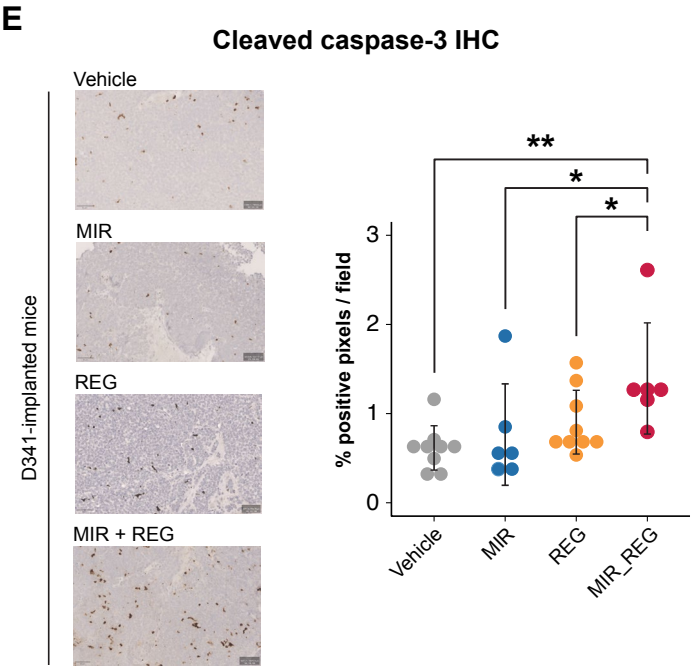

Figure 4

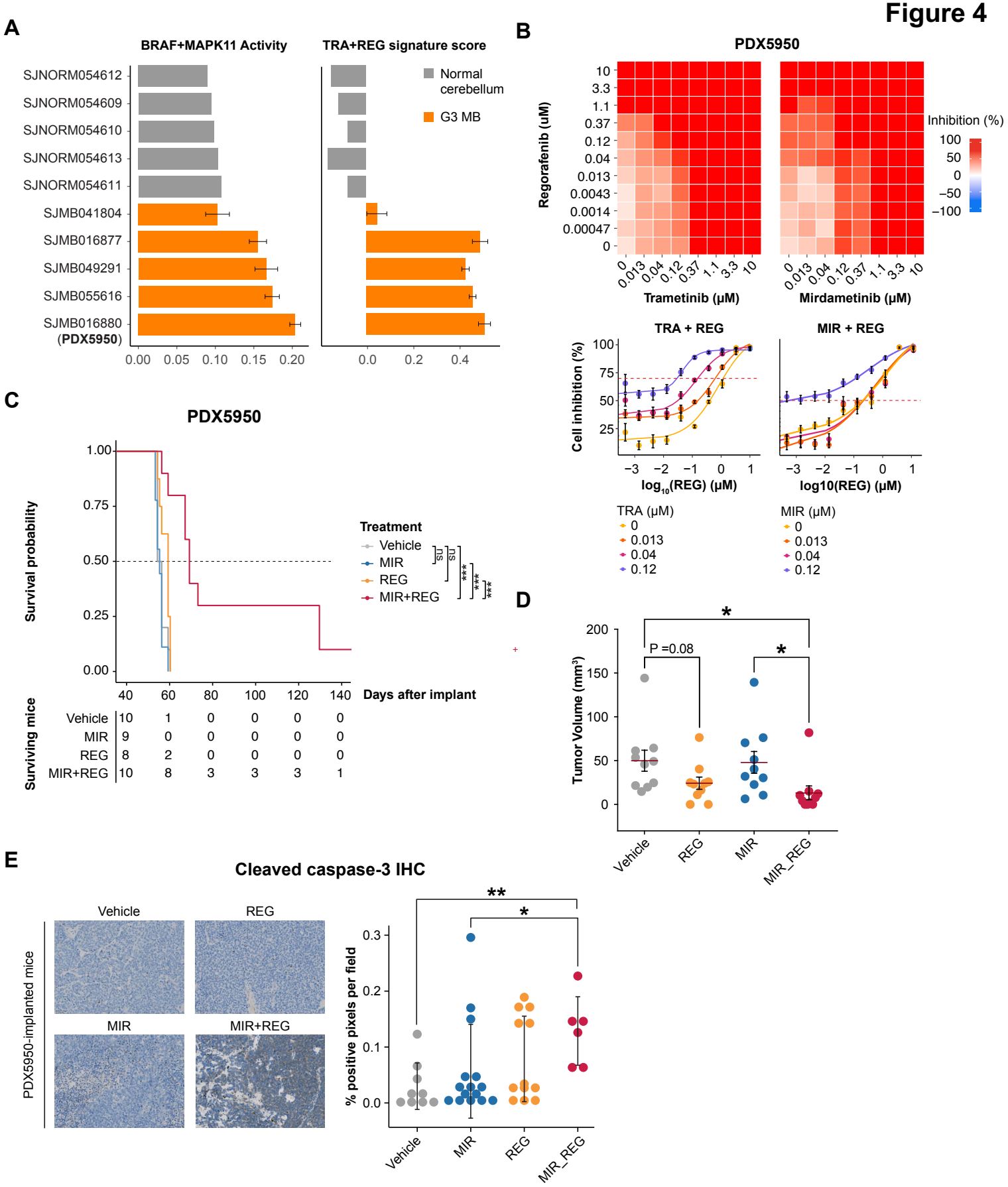
A
BRAF+MAPK11 Activity
TRA+REG signature score
SJNORM054612
SJNORM054609
SJNORM054610
SJNORM054613
SJNORM054611
SJMB041804
SJMB016877
SJMB049291
SJMB055616
SJMB016880 (PDX5950)
Normal cerebellum
G3 MB
B
PDX5950
Regorafenib (uM)
Trametinib (μM)
Mirdametinib (μM)
Inhibition (%)
TRA + REG
MIR + REG
Cell inhibition (%)
log10(REG) (μM)
TRA (μM)
MIR (μM)
C
PDX5950
Survival probability
Treatment
Vehicle
MIR
REG
MIR+REG
Days after implant
Surviving mice
D
Tumor Volume (mm³)
P =0.08
Vehicle
REG
MIR
MIR_REG
E
Cleaved caspase-3 IHC
PDX5950-implanted mice
Vehicle
REG
MIR
MIR+REG
% positive pixels per field

Figure 5

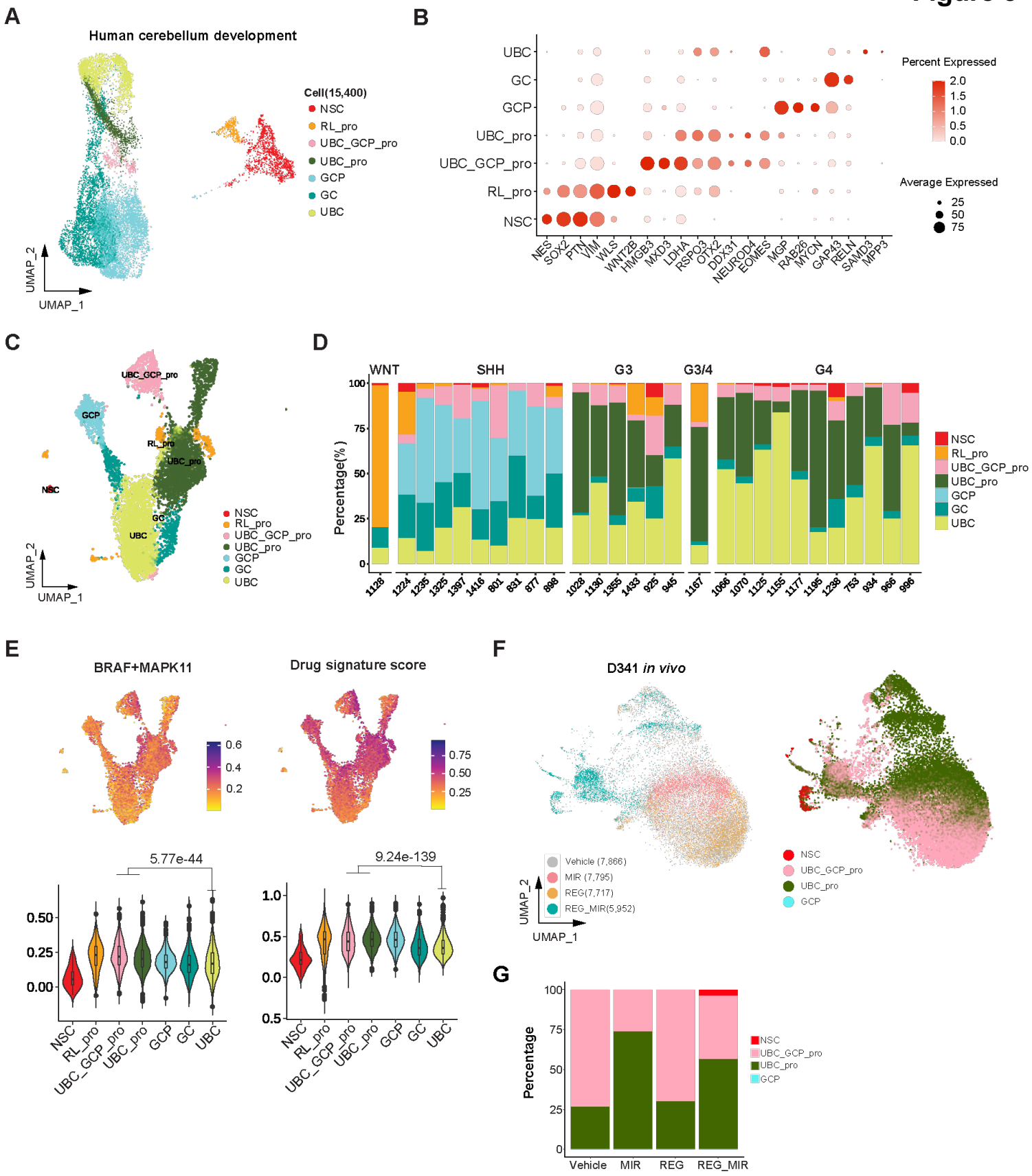
A
Human cerebellum development
Cell(15,400)
NSC
RL_pro
UBC_GCP_pro
UBC_pro
GCP
GC
UBC
UMAP_2
UMAP_1
B
UBC
GC
GCP
UBC_pro
UBC_GCP_pro
RL_pro
NSC
NES
SOX2
PTN
VIM
WLS
WNT2B
HMGB3
MXD3
LDHA
RSPO3
OTX2
DDX31
NEUROD4
EOMES
MGP
RAB26
MYCN
GAP43
RELN
SAMD3
MPP3
Percent Expressed
2.0
1.5
1.0
0.5
0.0
Average Expressed
25
50
75
C
UBC_GCP_pro
GCP
RL_pro
UBC_pro
NSC
GC
UBC
NSC
RL_pro
UBC_GCP_pro
UBC_pro
GCP
GC
UBC
UMAP_2
UMAP_1
D
WNT
SHH
G3
G3/4
G4
Percentage(%)
100
75
50
25
0
1128
1224
1235
1325
1397
1416
801
831
877
898
1028
1130
1355
1433
925
945
1167
1066
1070
1125
1155
1177
1195
1238
753
934
966
996
NSC
RL_pro
UBC_GCP_pro
UBC_pro
GCP
GC
UBC
E
BRAF+MAPK11
Drug signature score
0.6
0.4
0.2
0.75
0.50
0.25
5.77e-44
9.24e-139
0.50
0.25
0.00
1.0
0.5
0.0
0.5
NSC
RL_pro
UBC_GCP_pro
UBC_pro
GCP
GC
UBC
F
D341 in vivo
Vehicle (7,866)
MIR (7,795)
REG(7,717)
REG_MIR(5,952)
NSC
UBC_GCP_pro
UBC_pro
GCP
UMAP_2
UMAP_1
G
Percentage
100
75
50
25
0
Vehicle
MIR
REG
REG_MIR
NSC
UBC_GCP_pro
UBC_pro
GCP

Figure 5

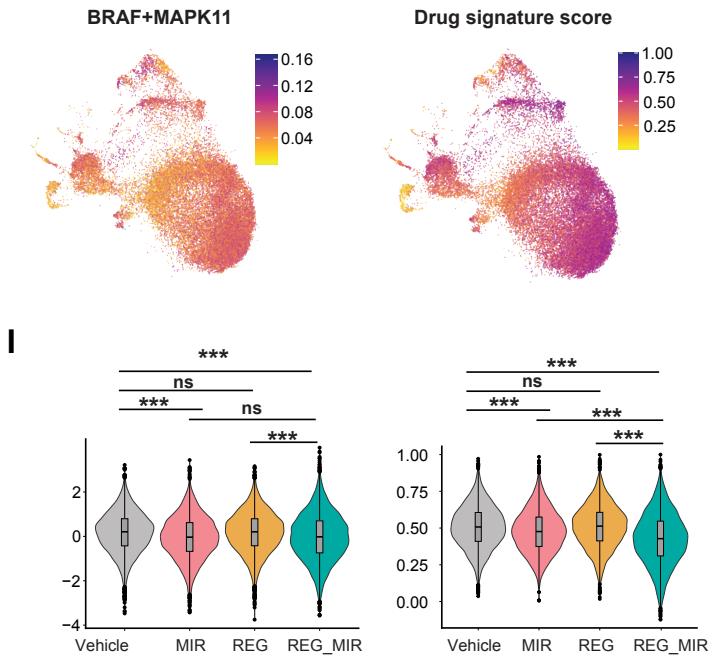
H
BRAF+MAPK11
0.16
0.12
0.08
0.04
Drug signature score
1.00
0.75
0.50
0.25
I
***
ns
***
ns
***
2
0
−2
−4
Vehicle
MIR
REG
REG_MIR
***
ns
***
***
***
1.00
0.75
0.50
0.25
0.00
Vehicle
MIR
REG
REG_MIR

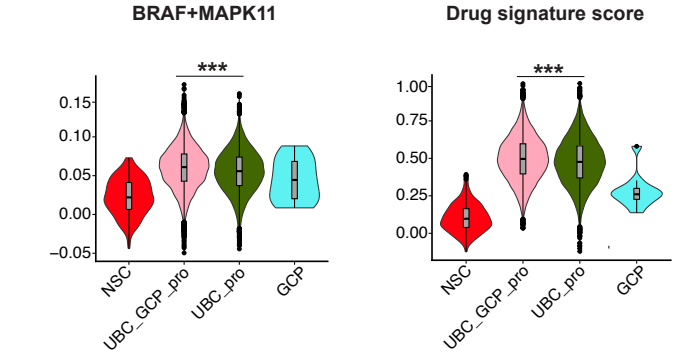
J
BRAF+MAPK11
***
0.15
0.10
0.05
0.00
−0.05
NSC
UBC_GCP_pro
UBC_pro
GCP
Drug signature score
***
1.00
0.75
0.50
0.25
0.00
NSC
UBC_GCP_pro
UBC_pro
GCP

Figure 6

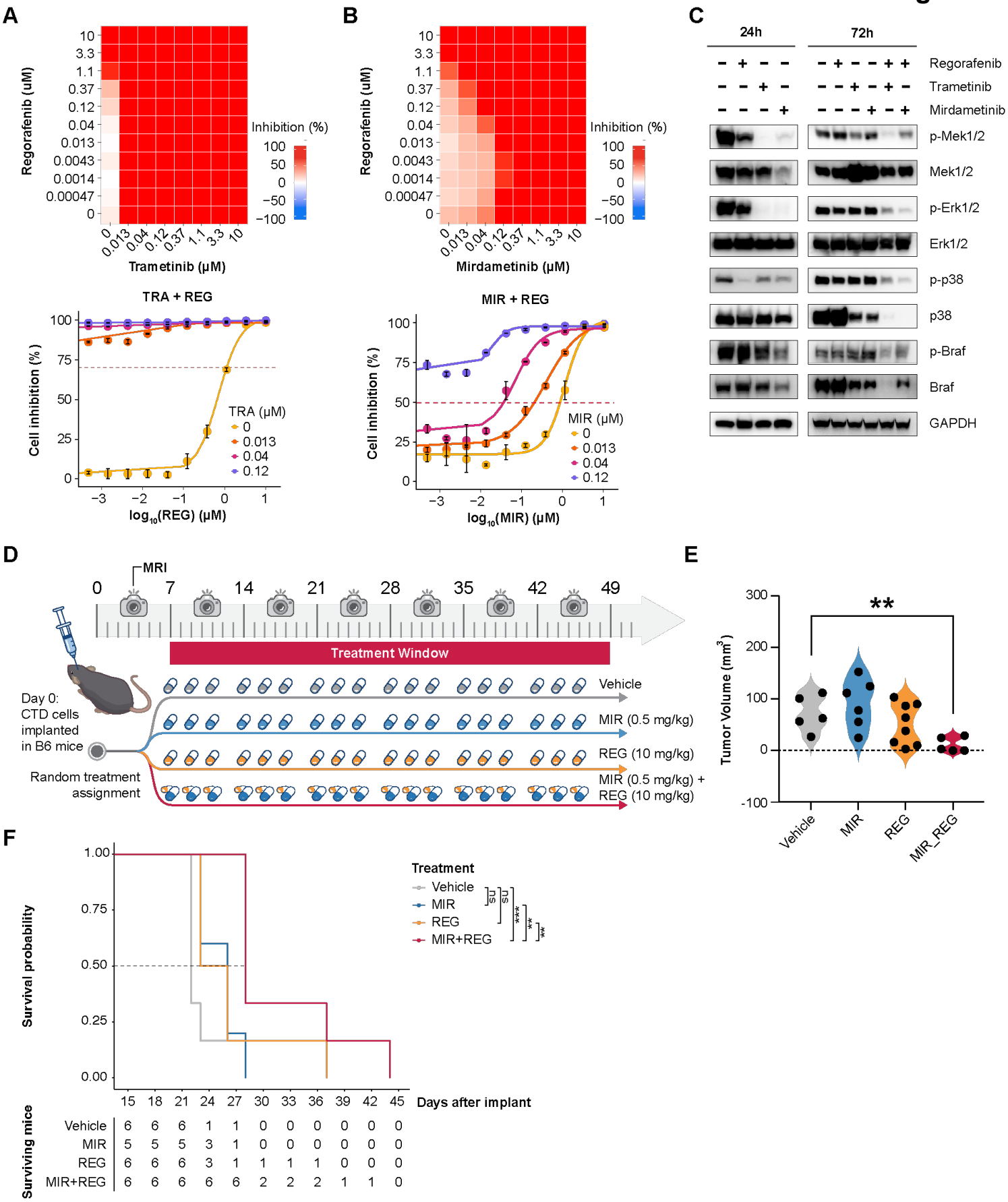
A
Regorafenib (uM)
Trametinib (μM)
Inhibition (%)
B
Regorafenib (uM)
Mirdametinib (μM)
Inhibition (%)
TRA + REG
Cell inhibition (%)
TRA (μM)
log10(REG) (μM)
MIR + REG
Cell inhibition (%)
MIR (μM)
log10(MIR) (μM)
C
24h
72h
Regorafenib
Trametinib
Mirdametinib
p-Mek1/2
Mek1/2
p-Erk1/2
Erk1/2
p-p38
p38
p-Braf
Braf
GAPDH
D
MRI
Treatment Window
Day 0:
CTD cells
implanted
in B6 mice
Random treatment
assignment
Vehicle
MIR (0.5 mg/kg)
REG (10 mg/kg)
MIR (0.5 mg/kg) +
REG (10 mg/kg)
E
Tumor Volume (mm3)
Vehicle
MIR
REG
MIR_REG
F
Survival probability
Treatment
Vehicle
MIR
REG
MIR+REG
Days after implant
Surviving mice
Vehicle 6 6 6 1 1 0 0 0 0 0 0
MIR 5 5 5 3 1 0 0 0 0 0 0
REG 6 6 6 3 1 1 1 1 0 0 0
MIR+REG 6 6 6 6 6 2 2 2 1 1 0

Figure 7

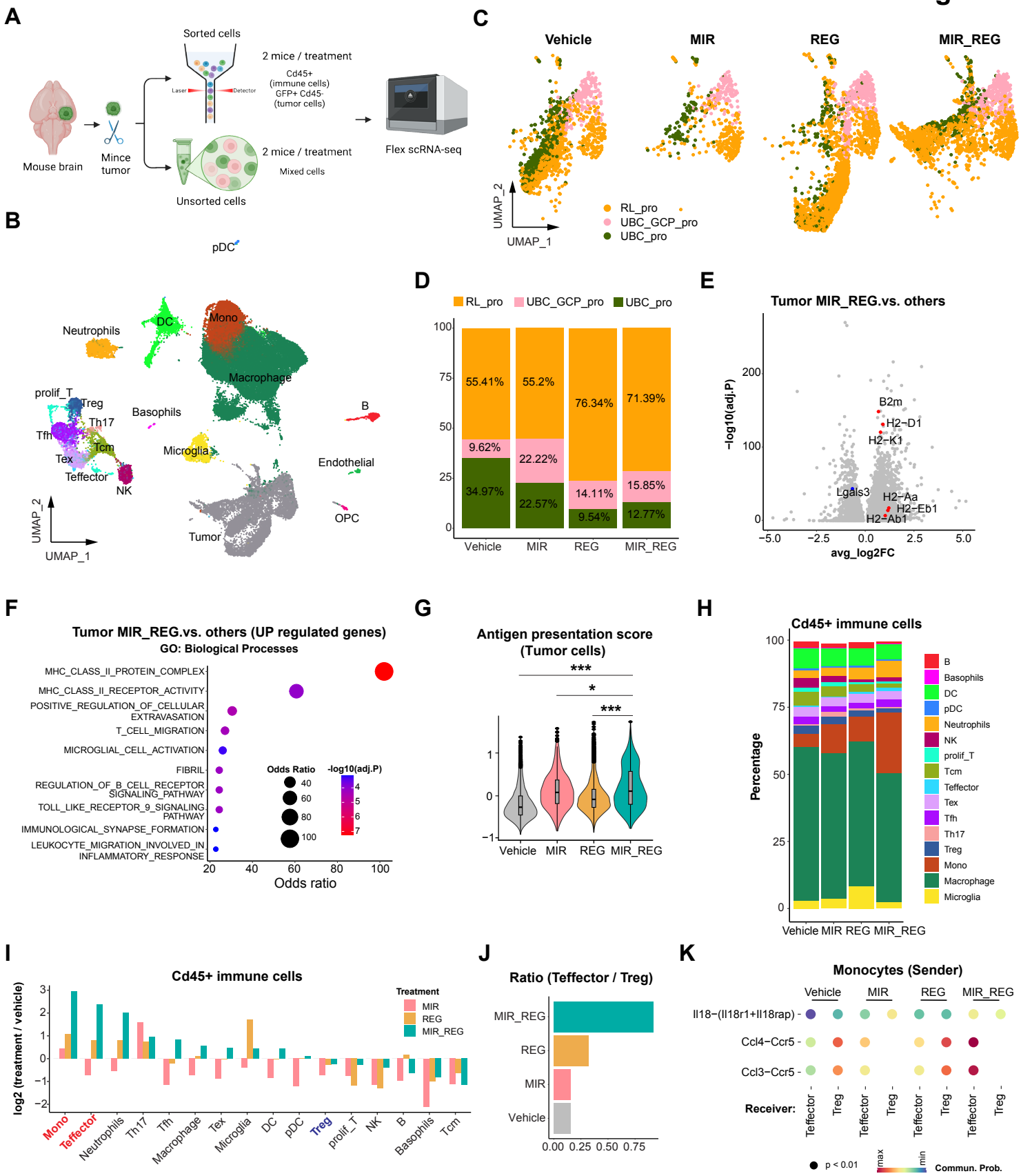
A
Sorted cells
2 mice / treatment
Cd45+ (immune cells) GFP+ Cd45- (tumor cells)
Laser
Detector
Mouse brain
Mince tumor
2 mice / treatment
Mixed cells
Unsorted cells
Flex scRNA-seq
B
pDC
Neutrophils
DC
Mono
Macrophage
prolif_T
Treg
Th17
Basophils
B
Tfh
Tcm
Microglia
Tex
Endothelial
Teffector
NK
OPC
Tumor
UMAP_2
UMAP_1
C
Vehicle
MIR
REG
MIR_REG
UMAP_2
UMAP_1
RL_pro
UBC_GCP_pro
UBC_pro
D
RL_pro
UBC_GCP_pro
UBC_pro
55.41%
9.62%
34.97%
55.2%
22.22%
22.57%
76.34%
14.11%
9.54%
71.39%
15.85%
12.77%
Vehicle
MIR
REG
MIR_REG
E
Tumor MIR_REG.vs. others
−log10(adj.P)
avg_log2FC
B2m
H2−D1
H2−K1
Lgals3
H2−Aa
H2−Eb1
H2−Ab1
F
Tumor MIR_REG.vs. others (UP regulated genes)
GO: Biological Processes
MHC_CLASS_II_PROTEIN_COMPLEX
MHC_CLASS_II_RECEPTOR_ACTIVITY
POSITIVE_REGULATION_OF_CELLULAR_EXTRAVASATION
T_CELL_MIGRATION
MICROGLIAL_CELL_ACTIVATION
FIBRIL
REGULATION_OF_B_CELL_RECEPTOR_SIGNALING_PATHWAY
TOLL_LIKE_RECEPTOR_9_SIGNALING_PATHWAY
IMMUNOLOGICAL_SYNAPSE_FORMATION
LEUKOCYTE_MIGRATION_INVOLVED_IN_INFLAMMATORY_RESPONSE
Odds Ratio
-log10(adj.P)
Odds ratio
G
Antigen presentation score (Tumor cells)
Vehicle
MIR
REG
MIR_REG
H
Cd45+ immune cells
Percentage
B
Basophils
DC
pDC
Neutrophils
NK
prolif_T
Tcm
Teffector
Tex
Tfh
Th17
Treg
Mono
Macrophage
Microglia
I
Cd45+ immune cells
log2 (treatment / vehicle)
Treatment
MIR
REG
MIR_REG
Mono
Teffector
Neutrophils
Th17
Tfh
Macrophage
Tex
Microglia
DC
pDC
Treg
prolif_T
NK
B
Basophils
Tcm
J
Ratio (Teffector / Treg)
MIR_REG
REG
MIR
Vehicle
K
Monocytes (Sender)
Vehicle
MIR
REG
MIR_REG
Il18−(Il18r1+Il18rap)
Ccl4−Ccr5
Ccl3−Ccr5
Receiver:
Teffector
Treg
p < 0.01
max
min
Commun. Prob.

Supplementary Figure S1

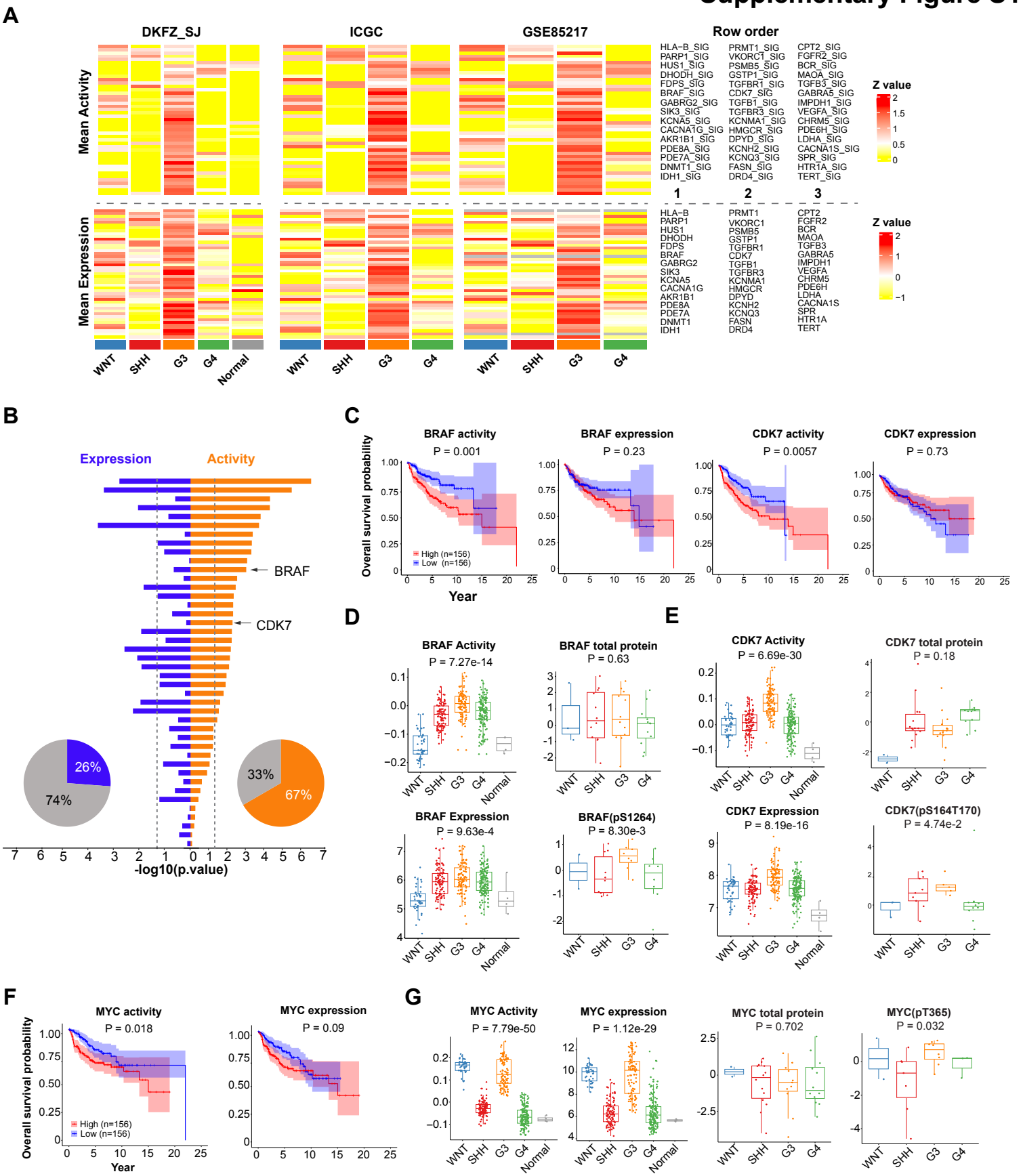

Supplementary Figure S2

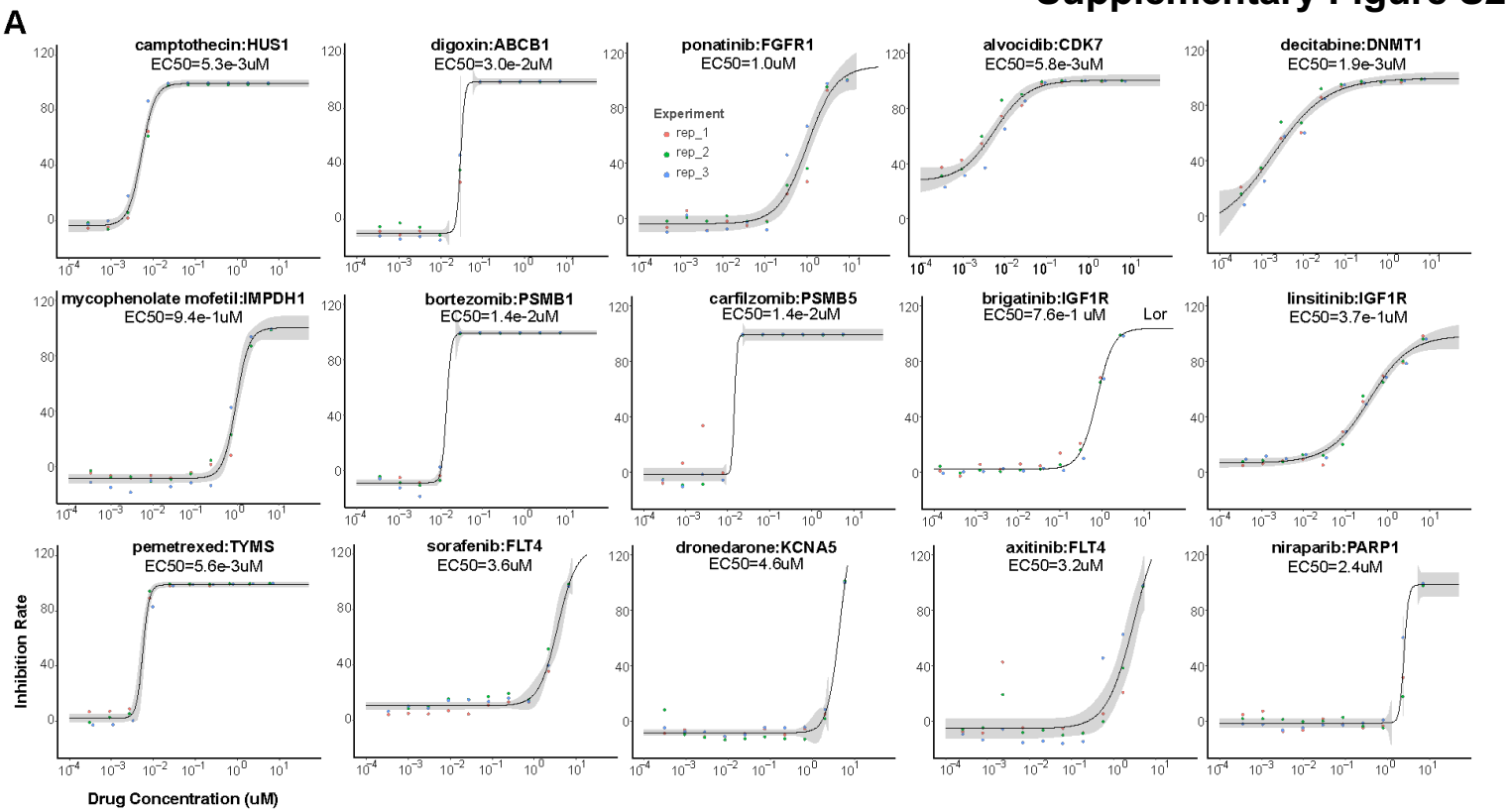

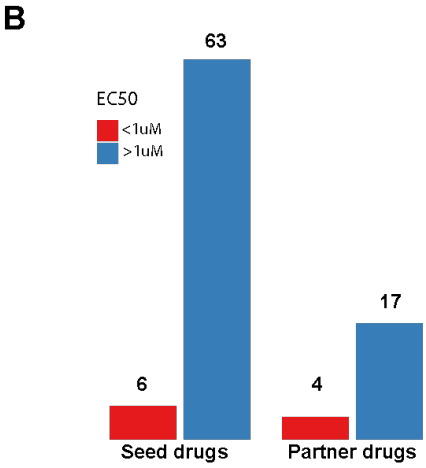

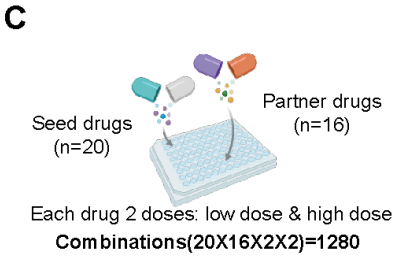

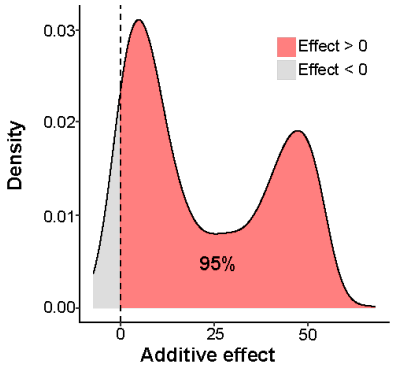

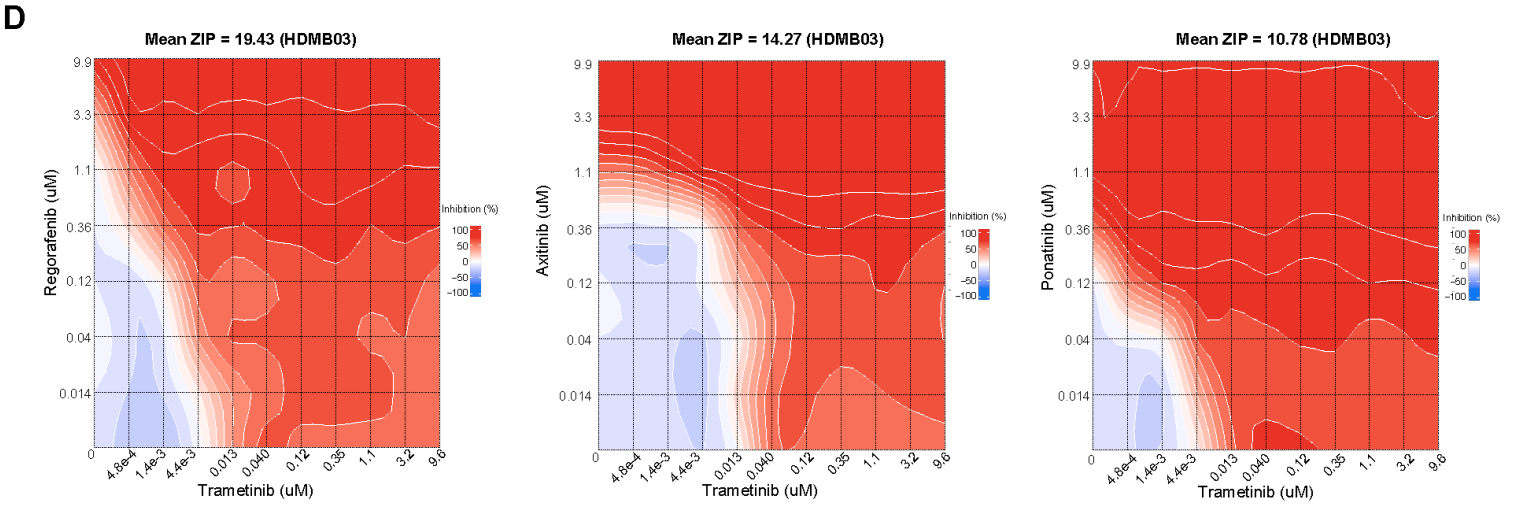

Supplementary Figure S3

A

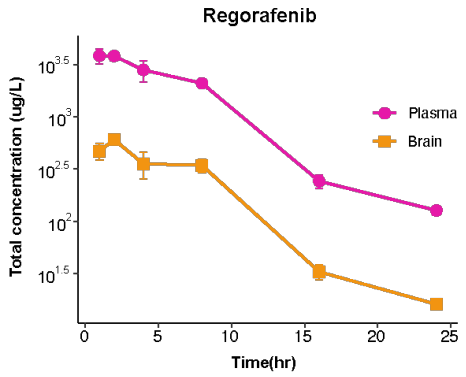

		Analyte	
		Regorafenib	
		Group	
		Brain	Plasma
Parameter	Unit	Value	
Cmax	ug/L	603	3830
Tmax	hr	2.00	1.00
AUClast	hr*ug/L	4350	30300
AUCinf	hr*ug/L	4410	30800
Kel	1/hr	0.191	0.175
T1/2	hr	3.63	3.96
CL/F	L/hr/kg	2.27	0.324
Vz/F	L/kg	11.9	1.85
Clast	ug/L	16.1	127
Tlast	hr	24.0	24.0
Kp_last		0.144	
Kp_inf		0.143	

B

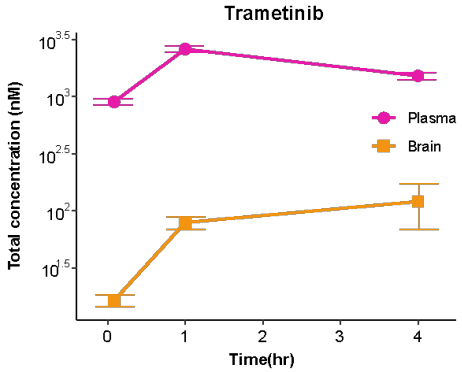

C

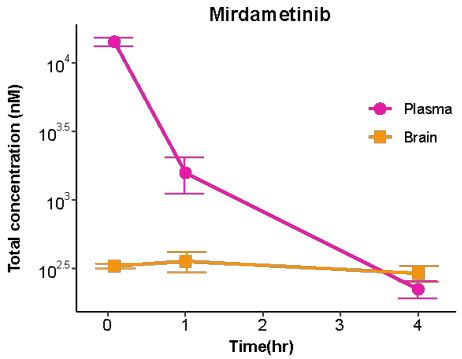

D

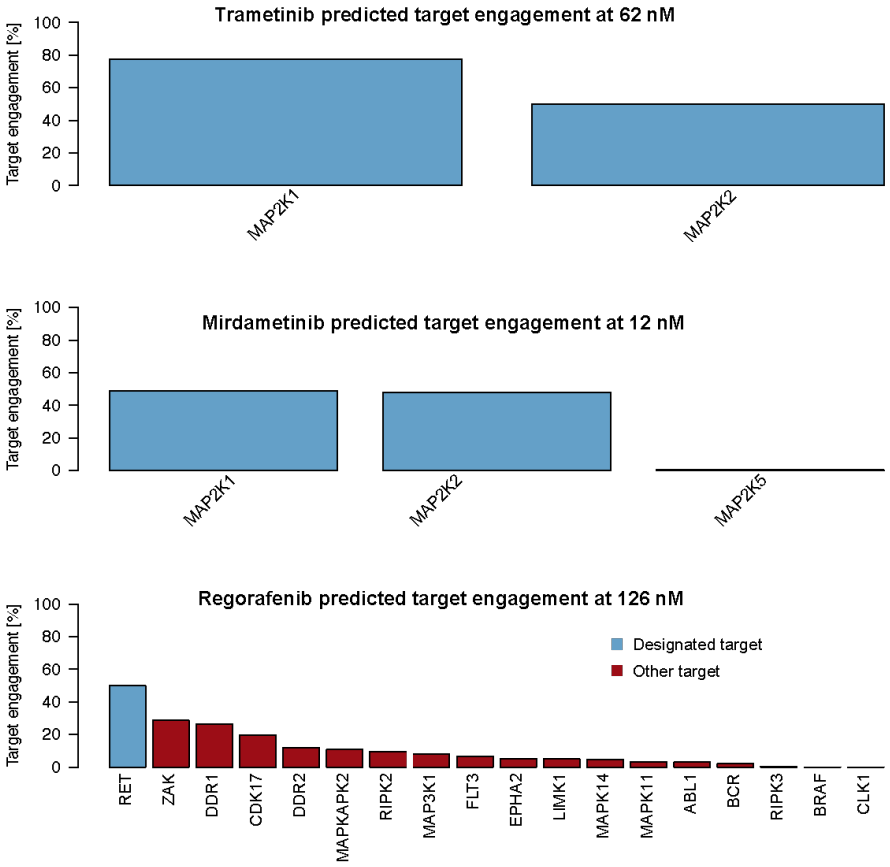

E

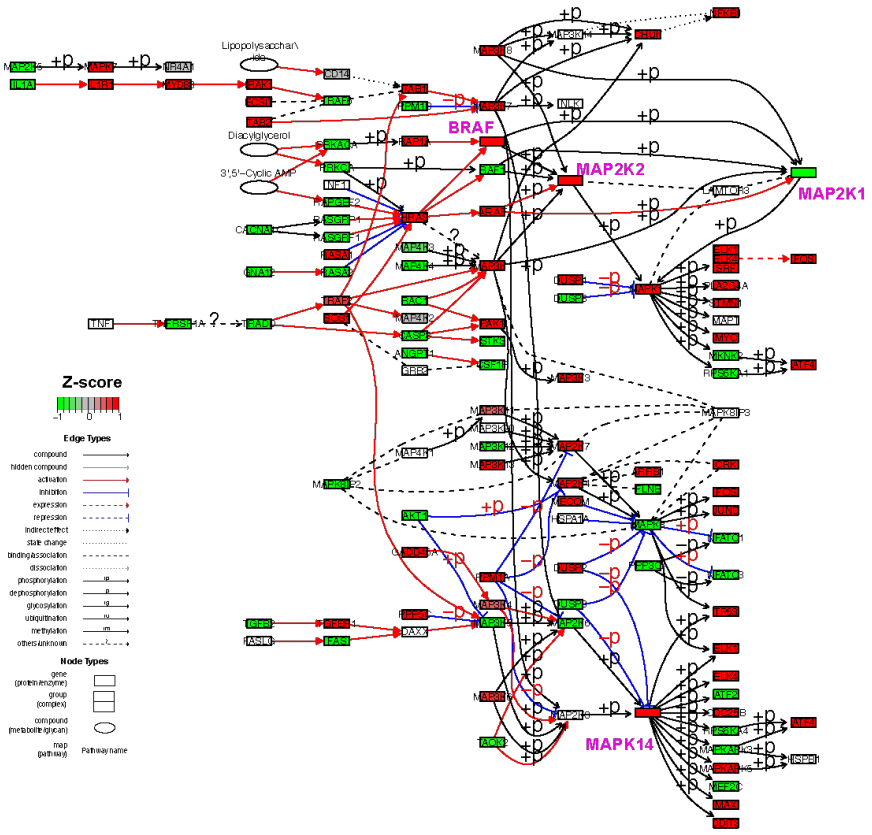

Supplementary Figure S4

A

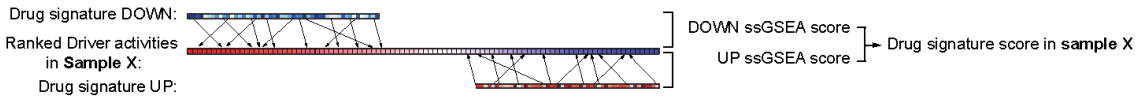

UP signature	UP gene	Down signature	Down gene number
CTRS_2230_regorafenib_up	103	CTRS_2230_regorafenib_down	42
CTRS_2295_trametinib_up	32	CTRS_2295_trametinib_down	28

B

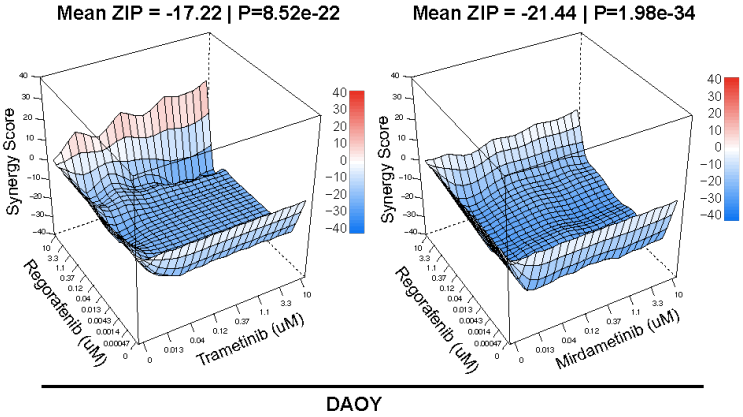

C

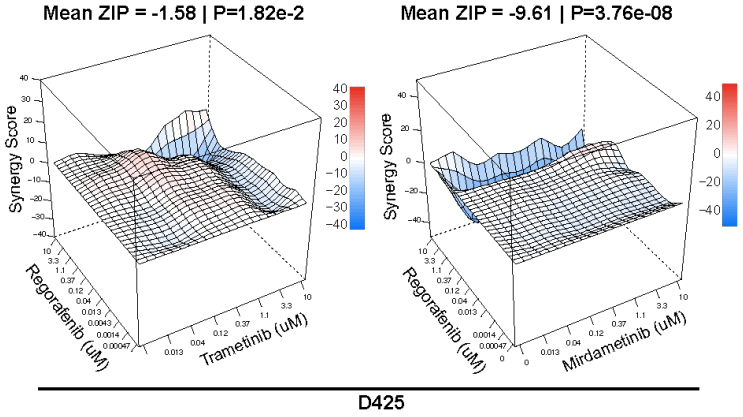

D

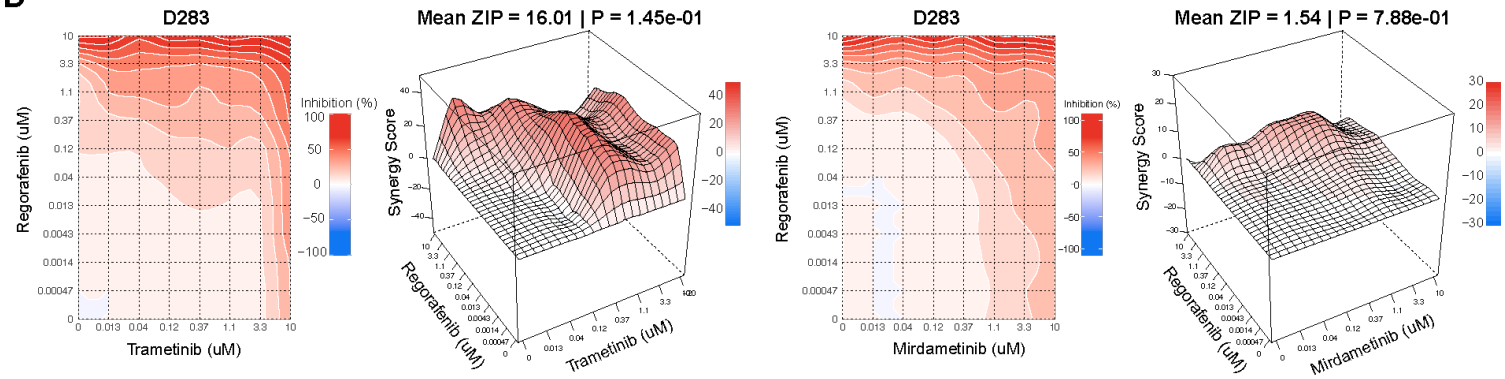

Supplementary Figure S5

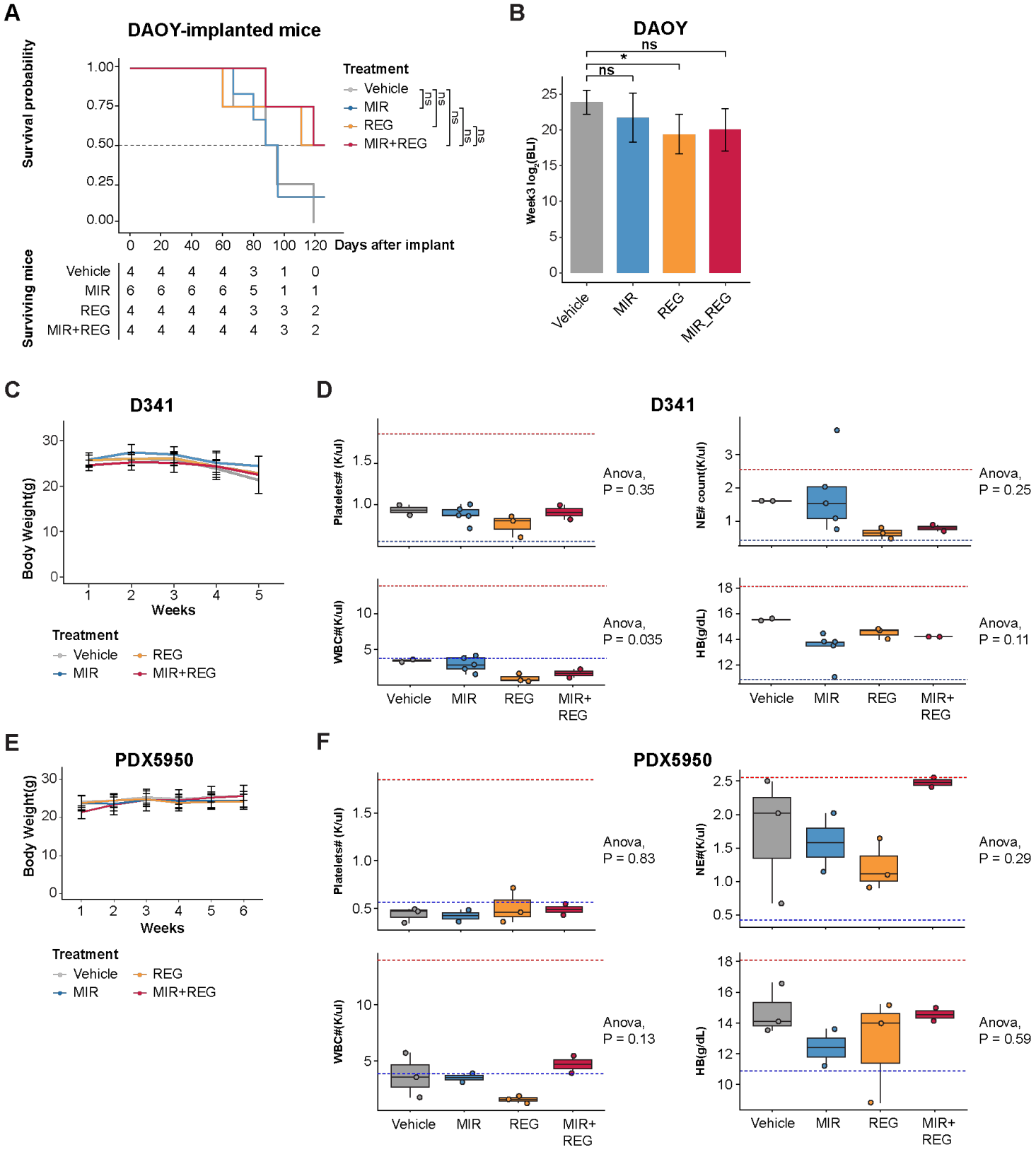

Supplementary Figure S6

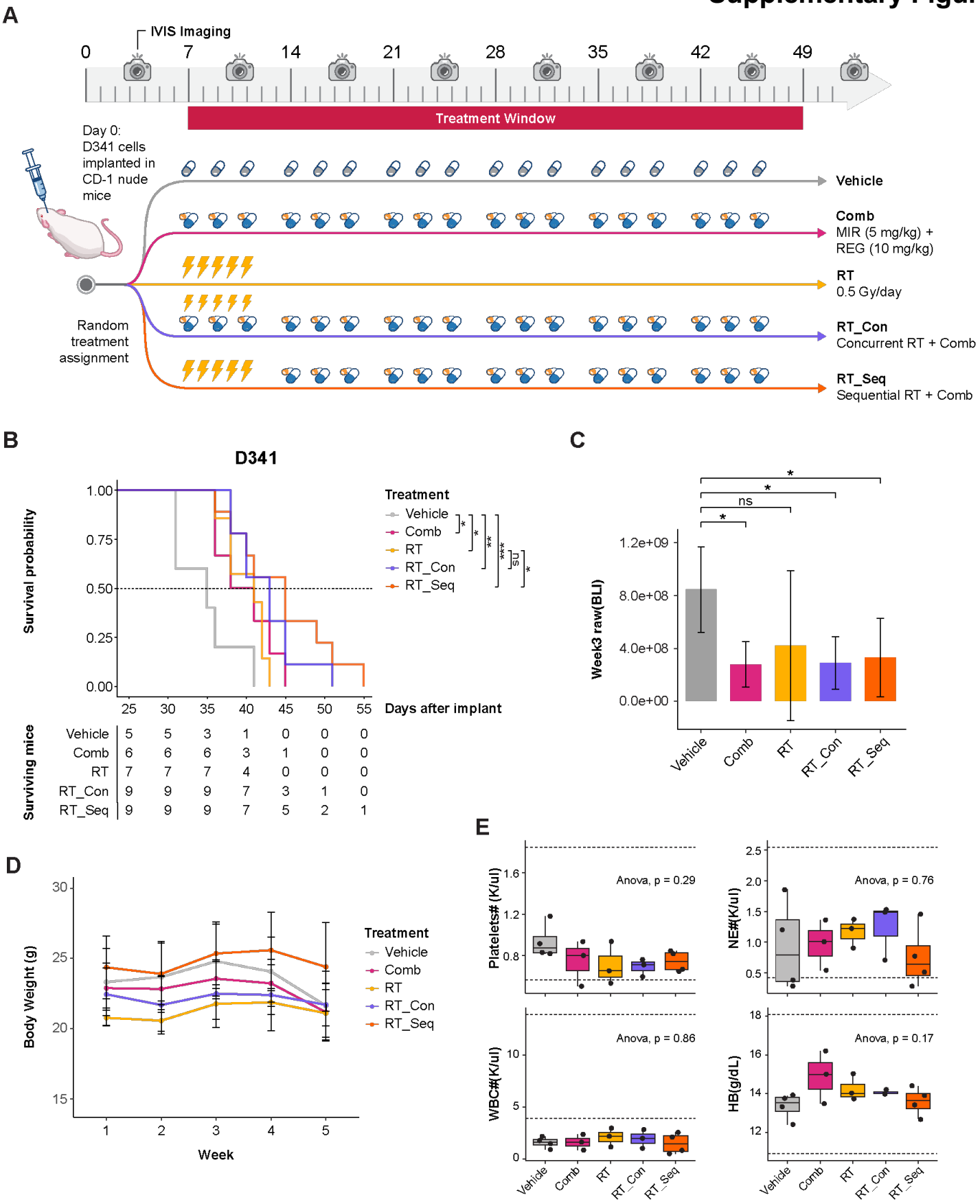

Supplementary Figure S7

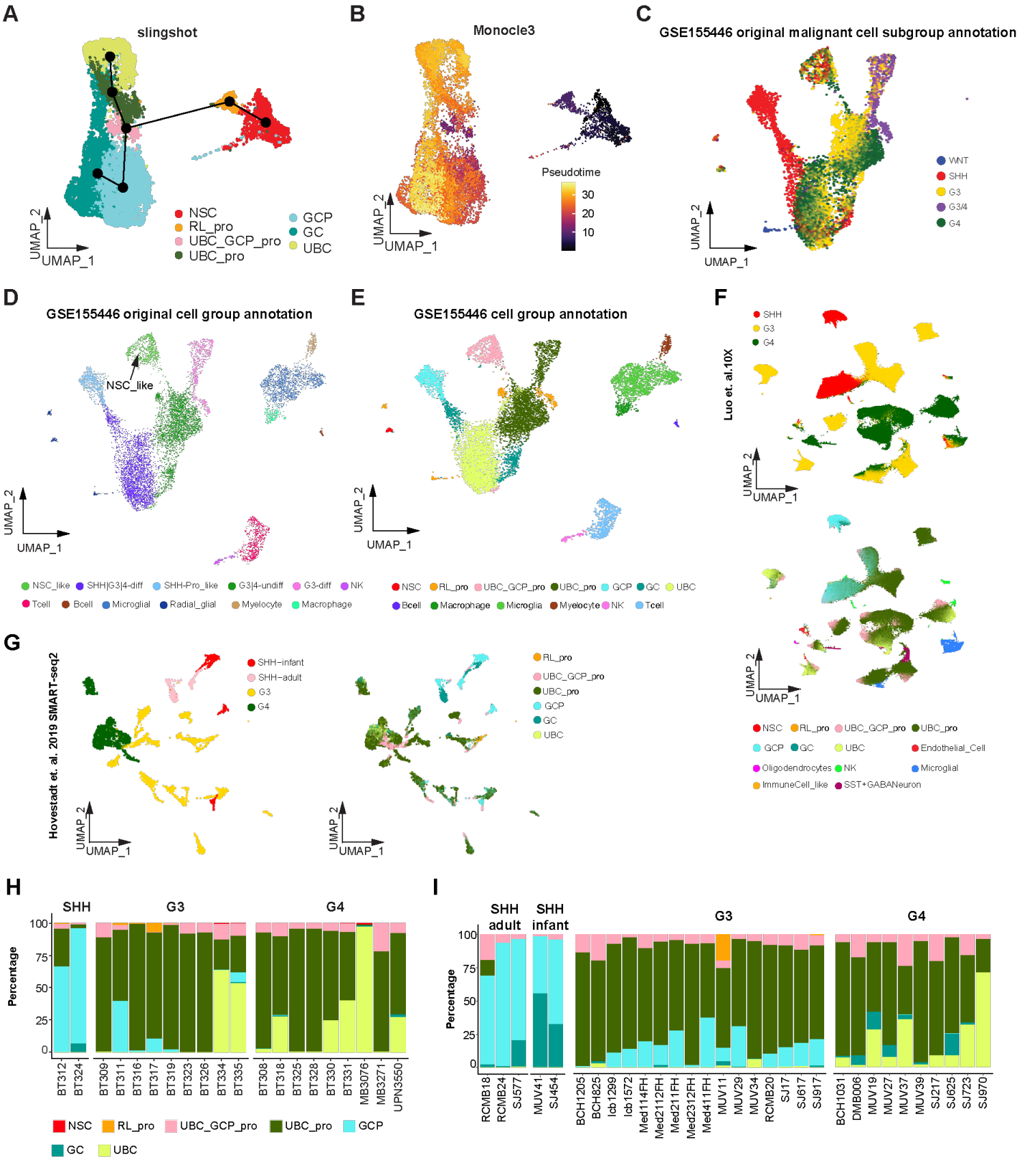

Supplementary Figure S8

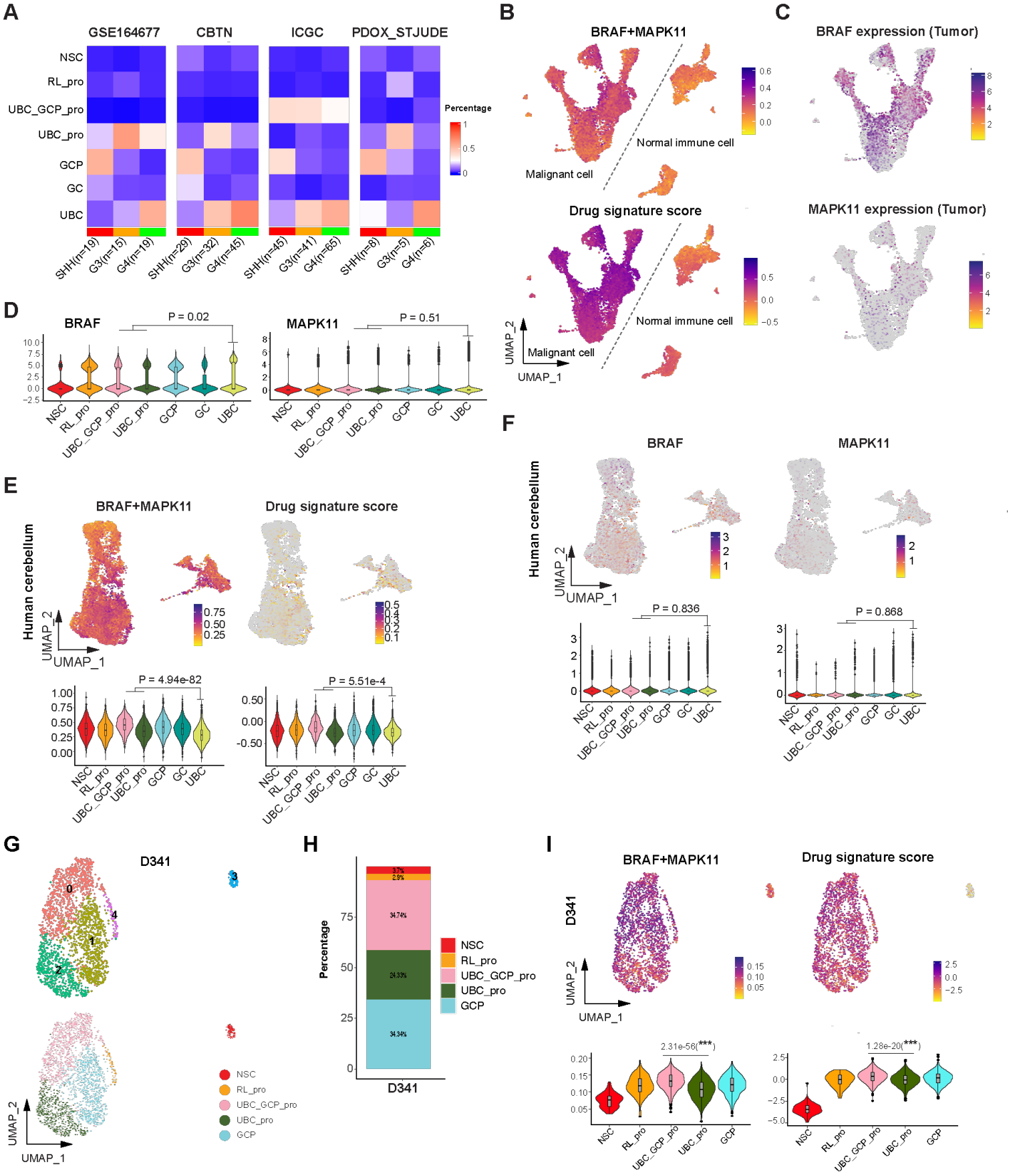

Supplementary Figure S9

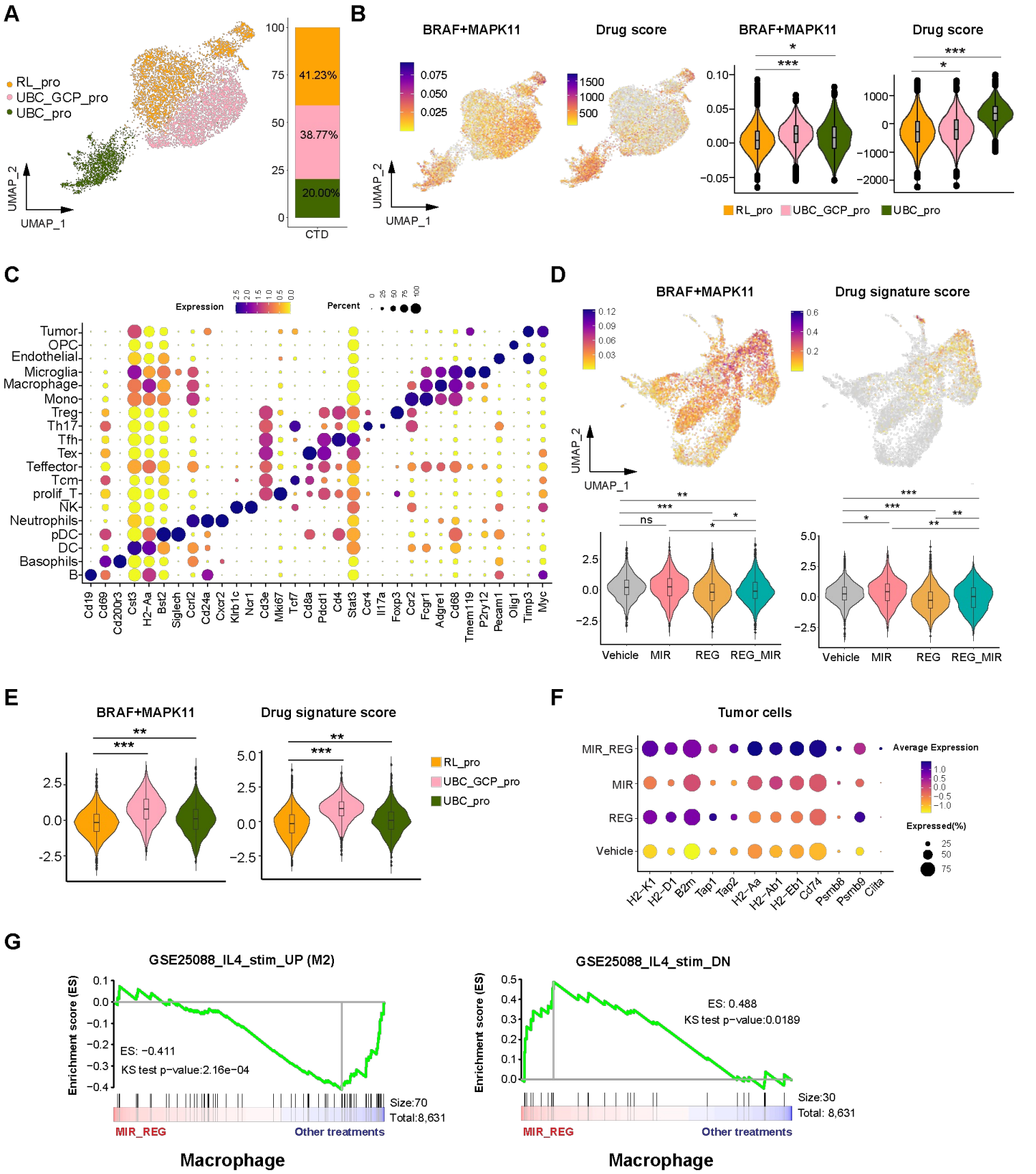
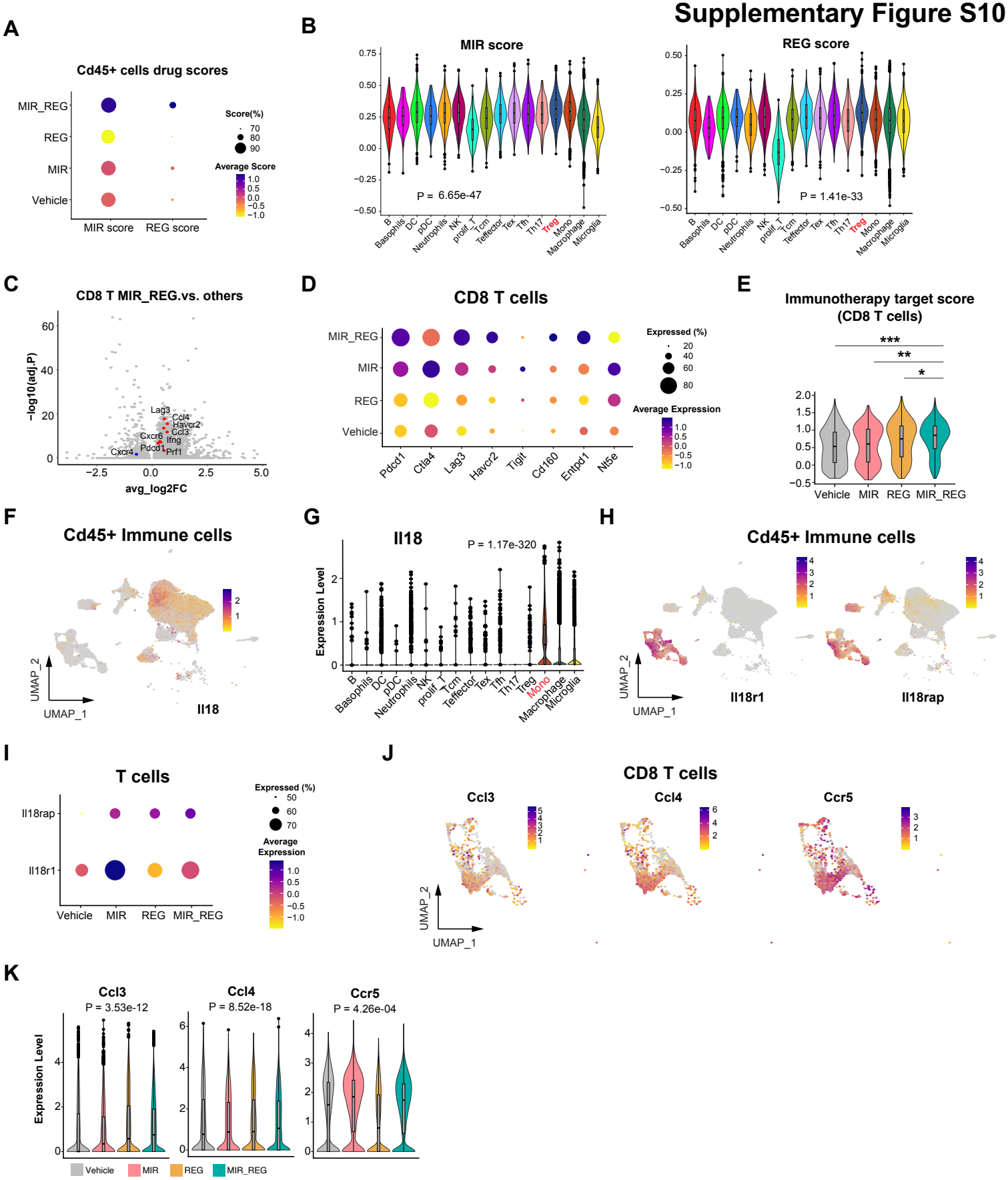
Supplementary Figure S10